Assumed Natural Strain and Stabilized Quadrilateral Lobatto Spectral Elements for C^0 Plate/Shell Analysis

K.Y.Sze*, Y.C.Hu
Department of Mechanical Engineering, The University of Hong Kong, Pokfulam, Hong Kong.
* Correspondence author (Email: kysze@hku.hk)

ABSTRACT

Lobatto elements are high-order or spectral elements featured by non-equispaced Lobatto nodes and the Lobatto nodal quadrature. The tensor product nature of the element interpolation allows the derivatives at the node be computed thru the derivatives along the nodal line which involve only 1D interpolations. In this paper, generic schemes for formulating assumed natural strain (ANS) and stabilized Lobatto Lagrange C^0 plate/shell elements of order ≥ 2 are presented. Two ANS schemes are devised. Both schemes sample the normal membrane and transverse shear natural strain components at the 1D reduced-order Gaussian quadrature points along the nodal lines. The difference is that the first and second schemes sample the membrane shear natural strain component at the Lobatto nodes and the 2D reduced-order Gaussian quadrature points, respectively. Meanwhile, all the other natural strain components in both schemes can be obtained by 1D interpolation along the nodal lines. In the stabilization scheme for reduced-integrated elements, only five stabilization vectors are required regardless of the element order. The new elements outperform the standard Lobatto element except when membrane-dominated curved thin shell problems with strong boundary layer effect are considered by coarse meshes.

Keywords: spectral finite element, high order, Lagrange element, stabilization, Lobatto, assumed natural strain

Published in *Int.J.Numer.Meth.Engng.* **111**: 403-446 (2017) DOI:: 10.1002/nme.5467

Submitted in July 2016, revised in September 2016, accepted in November 2016.

1. Introduction

For clarity, the abbreviations to be used repeatedly are first introduced: ANS for assumed natural strain [1-3], dofs for degrees of freedom, FGQ for full order Gaussian quadrature (namely, the (n_L+1)-point rule for n_L-th order element), FI for full integration by FGQ, LBQ for Lobatto quadrature [4], LB for the standard Lobatto element which is evaluated by LBQ, mixed interpolation of tensorial components (MITC) [5-9], RGQ for reduced order Gaussian quadrature (the n_L-point rule for n_L-th order element), RI for reduced-integration by RGQ, and ZEM for zero energy modes.

Low- and high-order elements have their own pros and cons. High-order elements are more promising in accuracy and convergence yet computationally more expensive than the low-order elements on the per node basis. If the domain geometry is not excessively complicated for mesh preparation, high-order elements can often offer a more appealing alternative than low-order elements. Lockings are pathological behaviours in which the element and thus the element assemblage are excessively stiff as if they were locked. When the element thickness drops, C^0 plate and flat shell elements may be plagued by shear locking whilst C^0 curved shell elements may also be plagued by membrane locking. To subdue lockings, advanced formulations including reduced and selectively reduced integration (SRI) [10-12], hybrid/mixed formulation [13-17], discrete Kirchhoff formulation [18, 19], stabilization method [14-17, 20, 21], ANS [1-3, 22], MITC [5-9] , method of substituted strain [23, 24], assumed natural deviatoric strain formulation (ANDES) [22, 25], discrete shear gap method (DSG) [26], enhanced assumed strain method (EAS) [22, 27-29], etc., have been proposed. In particular, ANS, MITC, method of substituted strain, ANDES and DSG are closely related. Besides DSG, the other four methods interpolate the natural strains at selected sampling points which are less in number than that of the FGQ. For simplicity, they would be collectively referred to as ANS. They manoeuvre the number of penalty-type constraints brought forward by the zero transverse shear and membrane strain conditions. Edge transverse shear and normal membrane natural strain samples are commonly used which are identical for the two elements sharing the same element edge. They are effective to reduce the number of independent constraints in the global level. While there are numerous first and second order advanced C^0 plate/shell elements, high-order advanced elements are relative rare. Some of the exceptions are third order stabilized elements [14, 15], third order MITC elements [6] and SRI elements [12], among others.

Lobatto elements are featured by their non-equispaced Lobatto nodes and Lobatto nodal integration rules LBQ [4]. The latter leads to a diagonal mass matrix which is important for explicit time integration and explains the widespread acceptance of the Lobatto elements in solving transient dynamics problems including those in acoustics, statics and dynamics, damage detection, structural health monitoring, seismology, medical imaging, computation fluid dynamics [4, 30-42]. Furthermore, the tensor product nature of the element interpolation allows the derivatives at the node

be computed thru the derivatives along the nodal line by using the differentiation matrix for the 1D interpolation.

In this paper, two ANS and a stabilized schemes for formulating Lobatto Lagrange C^0 plate/shell elements of order ≥ 2 are presented. In the first ANS scheme, all the natural strain samples employed are computed either along the nodal lines or at the nodes. Thus, they can be computed efficiently from 1D interpolations. To determine the strain sampling stations, 1D RGQ points are identified to be the superconvergent or Barlow points [43] for Lobatto but not equispaced nodes. For instance, the superconvergent points for the third order with equispaced nodes are $(0,\pm\sqrt{5/3})$ [44] whilst the RGQ points are $(0, \pm\sqrt{(3/5)})$. Our tests using third order C^0 beam elements also revealed that the predicted nodal deflections of the element with equispaced nodes are erroneous regardless whether the transverse shear strain is sampled at the superconvergent or RGQ points. Meanwhile, the predicted nodal deflections of the Lobatto element with the transverse shear strain sampled at RGQ points are much more accurate. In this light, the natural transverse shear and membrane normal strains would be sampled at the RGQ points along the nodal lines of the Lobatto element whilst all other strain components are sampled at the LBQ. The second ANS scheme only differs from the first one by sampling the natural membrane shear strain at the 2D RGQ points. The strain needs to go through a 2D interpolation for the value at the LBQ points. Thus, the second scheme is not as efficient as the first one. In the stabilization scheme for the reduced-integrated elements, only five stabilization vectors are required regardless of the element order. By generalizing the hybrid-stabilization method [16, 45] derived for the quadratic element, the vectors can be derived as explicit linear functions of the nodal dofs and geometric data. The stabilization can be formed more efficiently if sub-parametric geometry is employed. The new elements outperform the standard Lobatto element except when coarse meshes are employed in modelling membrane-dominated curved thin shell problems with strong boundary layer effect.

The rest of this paper is organized as follows. Section 2 introduces the Lobatto node and LBQ. Section 3 reviews how the conventional C^0 shell element can be formulated. Sections 4, 5 and 6 detail the two ANS schemes and the stabilization scheme. Section 7 presents the numerical examples and Section 8 is the concluding section. Throughout this paper, 1D and 2D arrays are underlined and double-underlined, respectively.

2. Lobatto Node and Lobatto Quadrature

Introduction to Lobatto nodes, LBQ and the nodal differentiation matrix can be found in [4]. A brief introduction is here presented for completeness. The set of n_L+1 Lobatto nodes bounded by -1 and +1

are the roots of the following equation:

$$(1-\xi^2)P'_{n_L}(\xi)=0 \tag{1}$$

in which P_{n_L} is the degree-n_L Legendre polynomial. Using Lagrange interpolation, the degree-n_L interpolation function for the node at $\xi = l_i$ is

$$L_i(\xi)=\frac{(\xi-l_1)\cdots(\xi-l_{i-1})(\xi-l_{i+1})\cdots(\xi-l_{n_L+1})}{(l_i-l_1)\cdots(l_i-l_{i-1})(l_i-l_{i+1})\cdots(l_i-l_{n_L+1})} \tag{2}$$

The Lobatto nodes are also the sampling points of LBQ which is exact for integrands up to degree-($2n_L$-1). The weighting factors for l_i are

$$w_i=\frac{2}{n_L(n_L+1)[P_{n_L}(l_i)]^2}\ . \tag{3}$$

If LBQ is employed to evaluate the mass matrix of the element, the coincidence of the nodes and quadrature points leads to a positive-definite diagonal matrix. The integrand leading to the mass matrix of a geometric regular element is of degree-$2n_L$. Thus, LBQ cannot exactly evaluate the matrix. Nevertheless, the minute inaccuracy does not affect the popularity of LB in explicit dynamic computations.

Nodal interpolation functions for 2D Lobatto or Lobatto Lagrange elements can be formed by the simple product rule. Using the two-index nodal notation as shown in Figure 1(a) and taking the plane element as an example, the interpolated coordinate vector $\underline{X}$ and displacement vector $\underline{U}$ are

$$\underline{X}=\sum_{i,j=1}^{n_L+1}L_i(\xi)L_j(\eta)\underline{X}_{ij} \quad \text{and} \quad \underline{U}=\sum_{i,j=1}^{n_L+1}L_i(\xi)L_j(\eta)\underline{U}_{ij} \tag{4}$$

Their derivatives with respect to the natural coordinates of the element $(\xi,\eta)\in$[-1,+1] at node-(p,q) can be expressed as

$$\left(\frac{\partial\underline{X}}{\partial\xi},\frac{\partial\underline{U}}{\partial\xi}\right)\Big|_{\xi=l_p,\eta=l_q}=\sum_{i=1}^{n_L+1}L'_i(l_p)\cdot(\underline{X}_{iq},\underline{U}_{iq})\ ,\ \left(\frac{\partial\underline{X}}{\partial\eta},\frac{\partial\underline{U}}{\partial\eta}\right)\Big|_{\xi=l_p,\eta=l_q}=\sum_{j=1}^{n_L+1}L'_j(l_q)\cdot(\underline{X}_{pj},\underline{U}_{pj}) \tag{5}$$

in which $L_i(l_j) = \delta_{ij}$ is invoked. They are the differential quadrature rules for the interpolated variables at the Lobatto nodes and $L'_i(l_j)$ defines the nodal differentiation matrix. It can be seen that all the 2D natural strain components at the LBQ point and, thus, the element stiffness matrix can be obtained by the 1D nodal differentiation matrix. That constitutes the other reason for the popularity of the LB element in addition to the diagonal mass matrix.

3. Conventional Formulation for C^0 Shell Elements

Although the conventional, standard or displacement-based formulation for C^0 shell elements can be easily found in the literature, it is presented here for completeness. Using the element in Figure 2 as an example, the global coordinates $\underline{X}$ along the nodal normal $\underline{X}_{ij}^{n}$ of node-(i,j) at $\underline{X}_{ij}^{o}$ can be expressed as:

$$\underline{X}_{ij} = \underline{X}_{ij}^{o} + \zeta \underline{X}_{ij}^{n} \tag{6}$$

where $\zeta \in [-1,+1]$ is the transverse natural coordinate and $|\underline{X}_{ij}^{n}|$ equals half of the nodal thickness at the node-(i,j), i.e. $t_{ij}/2$. The displacement along the same nodal normal is described as:

$$\underline{U}_{ij} = \underline{U}_{ij}^{o} + \zeta \underline{U}_{ij}^{n} = \underline{U}_{ij}^{o} + \zeta (\underline{f}_{ij}^{1}\phi_{ij}^{1} + \underline{f}_{ij}^{2}\phi_{ij}^{2}) \tag{7}$$

in which $\underline{U}_{ij}^{o}$ is the nodal displacement; $\underline{f}_{ij}$'s and $\underline{X}_{ij}^{n}$ are mutually perpendicular vectors; ϕ's are the rotations about $\underline{f}_{ij}$'s as shown in Figure 2; and $\underline{U}_{ij}^{n}$ is self-defined. The choices of $\underline{f}_{ij}$'s are not unique. Unless specified otherwise, they are taken to be

$$\underline{f}_{ij}^{1} = \frac{t_{ij}}{2}\begin{cases} \underline{e}_X & \text{for } \left\| \underline{X}_{ij}^{n} \times \underline{e}_Z \right\| = 0 \\ \dfrac{\underline{X}_{ij}^{n} \times \underline{e}_Z}{\left\| \underline{X}_{ij}^{n} \times \underline{e}_Z \right\|} & \text{otherwise} \end{cases} \qquad \text{and} \qquad \underline{f}_{ij}^{2} = \frac{2}{t_{ij}} \underline{X}_{ij}^{n} \times \underline{f}_{ij}^{1} \tag{8}$$

By interpolation, the coordinates and displacement at any point inside the element can be obtained as:

$$\underline{X} = \sum_{i,j=1}^{n_L+1} L_i(\xi) L_j(\eta)(\underline{X}_{ij}^{o} + \zeta \underline{X}_{ij}^{n}) = \underline{X}^{o} + \zeta \underline{X}^{n} \quad , \quad \underline{U} = \sum_{i,j=1}^{n_L+1} L_i(\xi) L_j(\eta)\left(\underline{U}_{ij}^{o} + \zeta \underline{U}_{ij}^{n}\right) = \underline{U}^{o} + \zeta \underline{U}^{n} \tag{9}$$

where $\underline{X}^o$, $\underline{X}^n$, $\underline{U}^o$ and $\underline{U}^n$ are self-defined and they are functions of the inplane natural coordinates (ξ,η). The natural strain which is the covariant strain defined with respect to the natural coordinates (ξ,η,ζ) is

$$\varepsilon_{pq} = \frac{1}{2}\left(\frac{\partial \underline{X}^{T}}{\partial p}\frac{\partial \underline{U}}{\partial q} + \frac{\partial \underline{X}^{T}}{\partial q}\frac{\partial \underline{U}}{\partial p}\right) \qquad \text{where } p,q = \xi,\eta,\zeta \tag{10}$$

With the second and first order ζ-terms in respectively the inplane and the transverse shear natural strain components discarded, they become

$$\varepsilon_{\xi\xi} = \varepsilon_{\xi\xi}^{0} + \zeta\varepsilon_{\xi\xi}^{1} \ , \ \varepsilon_{\eta\eta} = \varepsilon_{\eta\eta}^{0} + \zeta\varepsilon_{\eta\eta}^{1} \ , \ \gamma_{\xi\eta} = \gamma_{\xi\eta}^{0} + \zeta\gamma_{\xi\eta}^{1} \ ,$$

$$\gamma_{\zeta\xi} = 2\varepsilon_{\zeta\xi} = (\underline{X}^{n})^{T}\frac{\partial \underline{U}^{o}}{\partial \xi} + \left(\frac{\partial \underline{X}^{o}}{\partial \xi}\right)^{T}\underline{U}^{n} \ , \ \gamma_{\zeta\eta} = 2\varepsilon_{\zeta\eta} = (\underline{X}^{n})^{T}\frac{\partial \underline{U}^{o}}{\partial \eta} + \left(\frac{\partial \underline{X}^{o}}{\partial \eta}\right)^{T}\underline{U}^{n} \tag{11a-e}$$

where

$$\varepsilon^0_{\xi\xi} = (\frac{\partial \underline{X}^o}{\partial \xi})^T \frac{\partial \underline{U}^o}{\partial \xi} \ , \ \varepsilon^1_{\xi\xi} = (\frac{\partial \underline{X}^n}{\partial \xi})^T \frac{\partial \underline{U}^o}{\partial \xi} + (\frac{\partial \underline{X}^o}{\partial \xi})^T \frac{\partial \underline{U}^n}{\partial \xi} \ ,$$

$$\varepsilon^0_{\eta\eta} = (\frac{\partial \underline{X}^o}{\partial \eta})^T \frac{\partial \underline{U}^o}{\partial \eta} \ , \ \varepsilon^1_{\eta\eta} = (\frac{\partial \underline{X}^n}{\partial \eta})^T \frac{\partial \underline{U}^o}{\partial \eta} + (\frac{\partial \underline{X}^o}{\partial \eta})^T \frac{\partial \underline{U}^n}{\partial \eta} \ ,$$

$$\gamma^0_{\xi\eta} = 2\varepsilon^0_{\xi\eta} = (\frac{\partial \underline{X}^o}{\partial \xi})^T \frac{\partial \underline{U}^o}{\partial \eta} + (\frac{\partial \underline{X}^o}{\partial \eta})^T \frac{\partial \underline{U}^o}{\partial \xi} \ ,$$

$$\gamma^1_{\xi\eta} = 2\varepsilon^1_{\xi\eta} = (\frac{\partial \underline{X}^n}{\partial \xi})^T \frac{\partial \underline{U}^o}{\partial \eta} + (\frac{\partial \underline{X}^0}{\partial \xi})^T \frac{\partial \underline{U}^n}{\partial \eta} + (\frac{\partial \underline{X}^n}{\partial \eta})^T \frac{\partial \underline{U}^o}{\partial \xi} + (\frac{\partial \underline{X}^o}{\partial \eta})^T \frac{\partial \underline{U}^n}{\partial \xi} \ .$$

In the above expressions, superscripts "0" and "1" denote the zeroth and first order ζ-terms in the strain components, respectively. Let (x,y,z) be the local Cartesian coordinates for defining the material properties. With x and y tangential to the mid-surface defined by $\underline{X}^o$ and $\underline{X}^n$ assumed to be orthogonal to the mid-surface, the physical strain defined with respect to (x,y,z) can be obtained from the following transformations

$$\underline{\varepsilon} = \begin{Bmatrix} \varepsilon_{xx} \\ \varepsilon_{yy} \\ \gamma_{xy} \end{Bmatrix} = \begin{bmatrix} \xi_{,x}\,\xi_{,x} & \eta_{,x}\,\eta_{,x} & \xi_{,x}\,\eta_{,x} \\ \xi_{,y}\,\xi_{,y} & \eta_{,y}\,\eta_{,y} & \xi_{,y}\,\eta_{,y} \\ 2\xi_{,x}\,\xi_{,y} & 2\eta_{,x}\,\eta_{,y} & \xi_{,x}\,\eta_{,y} + \xi_{,y}\,\eta_{,x} \end{bmatrix} \begin{Bmatrix} \varepsilon_{\xi\xi} \\ \varepsilon_{\eta\eta} \\ \gamma_{\xi\eta} \end{Bmatrix} = \underline{\underline{T}}_{\varepsilon} \begin{Bmatrix} \varepsilon_{\xi\xi} \\ \varepsilon_{\eta\eta} \\ \gamma_{\xi\eta} \end{Bmatrix} = \underline{\underline{T}}_{\varepsilon} \left(\begin{Bmatrix} \varepsilon^0_{\xi\xi} \\ \varepsilon^0_{\eta\eta} \\ \gamma^0_{\xi\eta} \end{Bmatrix} + \zeta \begin{Bmatrix} \varepsilon^1_{\xi\xi} \\ \varepsilon^1_{\eta\eta} \\ \gamma^1_{\xi\eta} \end{Bmatrix} \right) \ ,$$

$$\underline{\varepsilon}^s = \begin{Bmatrix} \gamma_{zx} \\ \gamma_{zy} \end{Bmatrix} = \zeta_{,z} \begin{bmatrix} \xi_{,x} & \eta_{,x} \\ \xi_{,y} & \eta_{,y} \end{bmatrix} \begin{Bmatrix} \gamma^0_{\zeta\xi} \\ \gamma^0_{\zeta\eta} \end{Bmatrix} = \underline{\underline{T}}_{\gamma} \begin{Bmatrix} \gamma^0_{\zeta\xi} \\ \gamma^0_{\zeta\eta} \end{Bmatrix} \qquad (12a,b)$$

The entries in the two strain transformation matrices can be obtained as:

$$\begin{bmatrix} \xi_{,x} & \xi_{,y} & \xi_{,z} \\ \eta_{,x} & \eta_{,y} & \eta_{,z} \\ \zeta_{,x} & \zeta_{,y} & \zeta_{,z} \end{bmatrix} = \begin{bmatrix} x_{,\xi} & x_{,\eta} & x_{,\zeta} \\ y_{,\xi} & y_{,\eta} & y_{,\zeta} \\ z_{,\xi} & z_{,\eta} & z_{,\zeta} \end{bmatrix}^{-1} = \left(\begin{bmatrix} \underline{e}^T_x \\ \underline{e}^T_y \\ \underline{e}^T_z \end{bmatrix} \left[\underline{X}_{,\xi} \ \vdots \ \underline{X}_{,\eta} \ \vdots \ \underline{X}_{,\zeta} \right] \right)^{-1} \qquad (13)$$

It can be seen that $\underline{\underline{T}}_{\varepsilon}$ and $\underline{\underline{T}}_{\gamma}$ are functions of ζ. By expanding $\underline{\underline{T}}_{\varepsilon}$ about $\zeta = 0$, i.e. $\underline{\underline{T}}_{\varepsilon} = \underline{\underline{T}}^0_{\varepsilon} + \zeta \underline{\underline{T}}^1_{\varepsilon} + 0(\zeta^2)$, and retaining only the constant and linear ζ-terms in physical inplane strain, (12a) becomes

$$\underline{\varepsilon} = \underline{\varepsilon}^m + \zeta\, \underline{\varepsilon}^b = (\underline{\underline{T}}^0_{\varepsilon} + \zeta \underline{\underline{T}}^1_{\varepsilon} + 0(\zeta^2))(\begin{Bmatrix} \varepsilon^0_{\xi\xi} \\ \varepsilon^0_{\eta\eta} \\ \gamma^0_{\xi\eta} \end{Bmatrix} + \zeta \begin{Bmatrix} \varepsilon^1_{\xi\xi} \\ \varepsilon^1_{\eta\eta} \\ \gamma^1_{\xi\eta} \end{Bmatrix}) \simeq \underline{\underline{T}}^0_{\varepsilon} \begin{Bmatrix} \varepsilon^0_{\xi\xi} \\ \varepsilon^0_{\eta\eta} \\ \gamma^0_{\xi\eta} \end{Bmatrix} + \zeta (\underline{\underline{T}}^0_{\varepsilon} \begin{Bmatrix} \varepsilon^1_{\xi\xi} \\ \varepsilon^1_{\eta\eta} \\ \gamma^1_{\xi\eta} \end{Bmatrix} + \underline{\underline{T}}^1_{\varepsilon} \begin{Bmatrix} \varepsilon^0_{\xi\xi} \\ \varepsilon^0_{\eta\eta} \\ \gamma^0_{\xi\eta} \end{Bmatrix}) \qquad (14)$$

in which the self-defined $\underline{\varepsilon}^m$ and $\underline{\varepsilon}^b$ are the vectors of membrane and bending strain components, respectively. On the other hand, the physical transverse shear strain in (12b) is kept independent of ζ by using $\underline{\underline{T}}_{\gamma} \simeq \underline{\underline{T}}_{\gamma}\Big|_{\zeta=0} = \underline{\underline{T}}^0_{\gamma}$. Symbolically, the inplane strain $\underline{\varepsilon}$ and the transverse shear strain $\underline{\varepsilon}^s$ can be expressed as:

$$\underline{\varepsilon} = \underline{\varepsilon}^m + \zeta\,\underline{\varepsilon}^b = (\underline{\underline{B}}^m + \zeta\,\underline{\underline{B}}^b)\underline{d} \;\;,\;\; \underline{\varepsilon}^s = \underline{\underline{B}}^s\underline{d} \tag{15}$$

in which $\underline{\underline{B}}$s are independent of ζ and $\underline{d}$ is the element displacement vector embracing all the nodal translations and rotations of the element. With the Jacobian determinant $J = |[\underline{X},_\xi \;\; \underline{X},_\eta \;\; \underline{X},_\zeta]|$ approximated by $J_o = J|_{\zeta=0} = |[\underline{X}_o,_\xi \;\; \underline{X}_o,_\eta \;\; \underline{X}^n]|$, the potential energy functional of the element can be manipulated as

$$\Pi_P^e = \frac{1}{2}\int_{-1}^{+1}\int_{-1}^{+1}\int_{-1}^{+1}[(\underline{\varepsilon}^m + \zeta\,\underline{\varepsilon}^b)^T\,\underline{\underline{C}}_\varepsilon(\underline{\varepsilon}^m + \zeta\,\underline{\varepsilon}^b) + (\underline{\varepsilon}^s)^T\,\underline{\underline{C}}_s\,\underline{\varepsilon}^s)]J_o\,d\xi d\eta d\zeta - P^e \tag{16}$$

where P^e is the load potential for the element. For isotropic materials, the material elasticity matrices are

$$\underline{\underline{C}}_\varepsilon = \begin{bmatrix} E/(1-\nu^2) & \nu E/(1-\nu^2) & 0 \\ \nu E/(1-\nu^2) & E/(1-\nu^2) & 0 \\ 0 & 0 & G \end{bmatrix},\; \underline{\underline{C}}_s = kG\begin{bmatrix} 1 & 0 \\ 0 & 1 \end{bmatrix} \tag{17}$$

in which E is the elastic modulus, ν is the Poisson's ratio, $G = E/2/(1+\nu)$ is the shear modulus and k is the shear correction factor commonly taken to be 5/6. After integrating over ζ, Eq.(16) becomes

$$\Pi_P^e = \frac{1}{2}\sum_{\varphi=m,b,s}\langle(\underline{\varepsilon}^\varphi)^T\,\underline{\underline{D}}^\varphi\,\underline{\varepsilon}^\varphi\rangle^e - P^e \tag{18}$$

in which

$$\langle\circ\rangle^e = \int_{-1}^{+1}\int_{-1}^{+1}\circ J_o\,d\xi d\eta \;,\; \underline{\underline{D}}^m = \int_{-1}^{+1}\underline{\underline{C}}_\varepsilon d\zeta \;,\; \underline{\underline{D}}^b = \int_{-1}^{+1}\zeta^2\,\underline{\underline{C}}_\varepsilon d\zeta \;,\; \underline{\underline{D}}^s = \int_{-1}^{+1}\underline{\underline{C}}_\gamma d\zeta \;.$$

By invoking Eq.(15), the potential energy functional of the element can be written as

$$\Pi_P^e = \frac{1}{2}\underline{d}^T\sum_{\varphi=m,b,s}\langle(\underline{\underline{B}}^\varphi)^T\,\underline{\underline{D}}^\varphi\,\underline{\underline{B}}^\varphi\rangle^e\,\underline{d} - P^e \tag{19}$$

where the term between the two $\underline{d}$s is the element stiffness matrix.

When the stiffness matrix of Lobatto element is evaluated by LBQ, the resulting element model will be termed as LB element. It is trivial to show that the integrands at node ij depend only on the coordinates and dofs of nodes im and mj where $m = 1,\ldots,n_L+1$. This tensor product feature has been well-explored by computational mathematicians and is effective to reduce the computational cost of the LB element, see [12, 46, 47], among others.

4. First Assumed Natural Strain Scheme

When the element stiffness matrix is evaluated by numerical integration, each of the sampled

transverse shear and membrane strain components becomes a constraint penalized by the length-to-thickness ratio of the element. If the number of independent constraints in the global level is excessive, the element assembly would behave as if it was locked. The lower order assumed strain and ANS elements alleviate shear locking by sampling the natural transverse shear strains along the element edge [5, 24, 44]. Since there are fewer sampling points compared with FGQ and the "edge" strain samples are also identical for the two elements sharing the common element edge, the number of independent constraints is reduced in the global level yet the element is not rank deficient. Edge transverse shear and edge inplane normal strain samples are used in nearly all 9-node ANS elements [2, 23]. An exception is an early version of MITC9 9-node element [6, 48]. However, improved versions of MITC9 turned to edge transverse shear strain samples which better alleviate shear locking [7]. One of them also employs edge inplane normal strain and becomes rather similar to other ANS 9-node elements [2, 23], see Figure 3(a). On the other hand, the 16-node MITC16 element samples all its strain components away from the element boundary as portrayed in Figure 4(a) with the number of strain samples less than that used in the FGQ.

ANS often uses super-convergent points as the strain sampling points. Obviously, the function in (2) can interpolate exactly up to ξ^{n_L}. Following how super-convergent or Barlow points are identified [3, 43], ξ^{n_L+1} is interpolated at the Lobatto node thru (2). Thus, the interpolation error is

$$E(\xi) = \sum_{i=1}^{n_L+1} L_i(\xi) \cdot l_i^{n_L+1} - \xi^{n_L+1}$$

It is trivial that the n_L+1 Lobatto nodes are the roots of $E(\xi)$. By virtue of (1), $E(\xi)$ can be expressed as:

$$E(\xi) = a(1-\xi^2)P'_{n_L}(x) \tag{20}$$

where a is a constant. From the Legendre differential equation, i.e.

$$\frac{d}{d\xi}\left[(1-\xi^2)P'_{n_L}(\xi)\right] + n_L(n_L+1)P_{n_L}(\xi) = 0\,,$$

the derivative of $E(\xi)$ in (20) can be expressed as

$$E'(\xi) = \frac{d}{d\xi}\left[a(1-\xi^2)P'_{n_L}(\xi)\right] = -a \cdot n_L(n_L+1)P_{n_L}(\xi)\,.$$

E' and P_{n_L} share the same set of roots which are the RGQ points $\{g_i, i=1,..,n_L\}$. It should be remarked that if the interpolation function is based on equispaced nodes, the minimization of the interpolation error will result in another set of super-convergent points. For instance, the sampling points for third order equispaced nodes are $\{\pm\sqrt{5}/3,\ 0\}$ [44] which are different from the RGQ points $\{\pm\sqrt{(3/5)},\ 0\}$. Figure 5 shows the relative positions of the Lobatto nodes, equispaced nodes and RGQ points for the

6th and 7th order interpolations. The former is the highest order interpolation in which there is only one RGQ point between each pair of adjacent equispaced nodes. When the order goes up, there can be zero and more than one RGQ points between each pair of adjacent equispaced nodes. On the other hand, there is always one and only one RGQ point at roughly the midpoint of each pair of adjacent Lobatto nodes. Lobatto nodes appear to be the more natural choice of nodes than the equispaced if strains are sampled at RGQ points.

Next, a thin beam problem with the left end clamped and the right end pinned is considered. The cantilever has a rectangular cross section with unit width. Its length to thickness L/t ratio is 100. The ratio of the elastic modulus to shear modulus is 2.5. It is loaded by the uniform transverse load q_o per unit length. The thin beam solution for the deflection is fourth order in x, i.e.

$$w_{thin} = \frac{q_o L^4}{48EI}\left(\frac{x}{L}\right)^2\left[3-5\frac{x}{L}+2\left(\frac{x}{L}\right)^2\right] \quad \text{for} \quad 0 \le x \le L \tag{21}$$

One 4-node or cubic C^0 beam element, which cannot reproduce the thin beam solution, is employed to model the problem. The combinations of nodes and ANS sampling stations for the transverse shear strain γ include Lobatto nodes with γ sampled at RGQ points (LB_R), equispaced nodes with γ sampled at RGQ points (EQ_R) and equispaced nodes with γ sampled at superconvergent points (EQ_C). Figures 6(a), (b), (c) and (d) plot the normalized (w_{thin},θ_{thin}), w^h - w_{thin}, θ^h - θ_{thin} and γ^h, respectively, where h stands for finite element prediction, θ is the rotation and $\theta_{thin} = d(w_{thin})/dx$. The predictions of LB_R and EQ_R are identical. Recalling that the interior Lobatto and equispaced nodes are at $\xi \approx \pm 0.447$ and ± 0.333, respectively, it can be seen that w^h from LB_R and EQ_R is exceptionally close to w_{thin} at the interior Lobatto nodes but is erroneous at the interior equispaced nodes. The deflection of EQ_C are not accurate at neither the interior equispaced nor Lobatto nodes. While the rotations of LB_R and EQ_R is high accurate, that of EQ_C is erroneous. The predicted transverse shear strain are practically zero at the respective ANS sampling points at which the transverse shear constraints are enforced.

In view of the higher accuracy for the nodal deflection as well as the coincidence of the RGQ and super-convergent points, the ANS scheme to be presented is devised with respect to the LB element. In the scheme, the natural transverse shear and membrane normal strain components are sampled and interpolated at the 1D RGQ points $\{g_k, k = 1,\ldots, n_L\}$ of the nodal lines whilst all other natural strain components are directly evaluated at LB nodes or, equivalently, LBQ points. The scheme is considerably different from that of the MITC16 [6, 48] in terms of the nodal and ANS sampling positions. With reference to Figures 3(b) and 4(b), $\varepsilon^0_{\xi\xi}$ in Eq. (11a) along $\eta = l_j$ and at (g_k, l_j) are

$$\varepsilon^0_{\xi\xi}\Big|_{\eta=l_j} = [(\frac{\partial \underline{X}^o}{\partial \xi})^T \frac{\partial \underline{U}^o}{\partial \xi}]\Big|_{\eta=l_j} = \sum_{p,q=1}^{n_L+1} L'_p(\xi)L'_q(\xi)(\underline{X}^o_{pj})^T \underline{U}^o_{qj} \ , \ \varepsilon^0_{\xi\xi}\Big|_{\xi=g_k,\eta=l_j} = \sum_{p,q=1}^{n_L+1} L'_p(g_k)L'_q(g_k)(\underline{X}^o_{pj})^T \underline{U}^o_{qj} \tag{22}$$

The assumed $\varepsilon^0_{\xi\xi}$ is obtained by 1D interpolation at the 1D RGQ points and can be expressed as

$$\tilde{\varepsilon}^0_{\xi\xi}\Big|_{\eta=l_j} = \sum_{k=1}^{n_L} G_k(\xi)\cdot \varepsilon^0_{\xi\xi}\Big|_{(\xi=g_k,\eta=l_j)} = \sum_{p,q=1}^{n_L+1} \mathcal{R}_{pq}(\xi)(\underline{X}^o_{pj})^T \underline{U}^o_{qj} \tag{23}$$

where

$$G_k(\xi) = \frac{(\xi-g_1)\cdots(\xi-g_{k-1})(\xi-g_{k+1})\cdots(\xi-g_{n_L})}{(g_i-g_1)\cdots(g_i-g_{i-1})(g_i-g_{i+1})\cdots(g_i-g_{n_L})} \quad \text{and} \quad \mathcal{R}_{pq}(\xi) = \sum_{k=1}^{n_L} G_k(\xi)L'_p(g_k)L'_q(g_k)\,.$$

At node-(i, j),

$$\tilde{\varepsilon}^0_{\xi\xi}\Big|_{(\xi=l_i,\eta=l_j)} = \sum_{p,q=1}^{n_L+1} \mathcal{R}_{pq}(l_i)\cdot(\underline{X}^o_{pj})^T \underline{U}^o_{qj} = \sum_{p,q=1}^{n_L+1} \mathcal{R}_{pqi}\cdot(\underline{X}^o_{pj})^T \underline{U}^o_{qj} \tag{24}$$

in which $\mathcal{R}_{pqi}$ is self-defined. Similarly, the assumed $\gamma_{\zeta\xi}$ at node-(i, j) can be derived to be

$$\tilde{\gamma}_{\zeta\xi}\Big|_{(\xi=l_i,\eta=l_j)} = \sum_{p,q=1}^{n_L+1} [\ \mathcal{S}_{qpi}\cdot(\underline{X}^n_{pj})^T \underline{U}^o_{qj} + \mathcal{S}_{pqi}\cdot(\underline{X}^0_{pj})^T \underline{U}^n_{qj}\ ] \tag{25}$$

where

$$\mathcal{S}_{pqi} = \sum_{k=1}^{n_L} G_k(l_i)L'_p(g_k)L_q(g_k)\,.$$

The values of $\mathcal{R}_{pqi}$ and $\mathcal{S}_{pqi}$ can be precomputed and stored for efficient computation of the element stiffness matrix. Similarly, $\tilde{\varepsilon}^0_{\eta\eta}$ and $\tilde{\gamma}_{\zeta\eta}$ at node-(i, j) can be obtained.

The remaining natural strain components are directly evaluated at LB nodes by using the differential quadrature rule introduced in (5). In particular,

$$\gamma^0_{\xi\eta}\Big|_{\xi=l_i,\eta=l_j} = \sum_{p,q=1}^{n_L+1} L'_p(l_i)L'_q(l_j)[(\underline{X}^o_{pj})^T \underline{U}^o_{iq} + (\underline{X}^o_{iq})^T \underline{U}^o_{pj}]\,. \tag{26}$$

5. Second Assumed Natural Strain Scheme

The second ANS scheme only differs from the first one by sampling the natural membrane shear strain at the 2D RGQ points. This practice is also used in the MITC9 and MITC16 elements [6, 48] but not the other ANS elements. Similar to (24) and (25), the assumed natural membrane shear strain

at the LB points in this scheme can be derived to be

$$\tilde{\gamma}^0_{\xi\eta}\Big|_{\xi=l_i,\eta=l_j} = \sum_{a=1}^{n_L}\sum_{b=1}^{n_L} G_a(l_i)G_b(l_j)\cdot\gamma^0_{\xi\eta}\Big|_{(\xi=g_a,\eta=g_b)} = \sum_{p,q,r,s=1}^{n_L+1} (S_{pri}S_{sqj}+S_{rpi}S_{qsj})(\underline{X}^o_{pq})^T\underline{U}^o_{rs} \qquad (27)$$

Comparing (26) with (27), the former involves only two summation indices and thus are more efficient.

6. Stabilization for Reduced-Integrated Element

The computational efficiency and accuracy of the RI element had been known since 1970's. The drawback of the RI element is the existence of compatible ZEM which leads to the well-known hourglass instability. While stabilized first and second order RI C^0 shell elements based on the derivation of stabilization vectors can be found in the literature [16, 49, 50], their extensions to higher order elements are seldom, if not never, seen. Recently, the authors have generalized the hybrid-stabilization method previously derived for 9-node Lagrange C^0 shell elements [16, 45] to higher order plane and axisymmetric elements [41]. Here, the method would further be generalized to high-order C^0 shell elements.

For a square 2×2 flat n_L-th order RI element where $n_L \geq 2$, the compatible ZEM can be identified to be

$$\begin{Bmatrix} u_\xi \\ u_\eta \\ u_\zeta \end{Bmatrix} = \begin{bmatrix} \Psi & 0 & \zeta\Psi & 0 & 0 \\ 0 & \Psi & 0 & \zeta\Psi & 0 \\ 0 & 0 & 0 & 0 & \Psi \end{bmatrix} \begin{Bmatrix} c_1 \\ \vdots \\ c_5 \end{Bmatrix} \qquad (28)$$

where $\Psi = P_{n_L}(\xi)P_{n_L}(\eta)$ and c's are coefficients. They lead to the following strain modes

$$\begin{Bmatrix} \varepsilon_{\xi\xi} \\ \varepsilon_{\eta\eta} \\ 2\varepsilon_{\xi\eta} \end{Bmatrix} = \begin{bmatrix} \Psi_{,\xi} & 0 \\ 0 & \Psi_{,\eta} \\ \Psi_{,\eta} & \Psi_{,\xi} \end{bmatrix} \begin{Bmatrix} c_1 \\ c_2 \end{Bmatrix} + \zeta \begin{bmatrix} \Psi_{,\xi} & 0 \\ 0 & \Psi_{,\eta} \\ \Psi_{,\eta} & \Psi_{,\xi} \end{bmatrix} \begin{Bmatrix} c_3 \\ c_4 \end{Bmatrix}, \quad \begin{Bmatrix} 2\varepsilon_{\xi\zeta} \\ 2\varepsilon_{\eta\zeta} \end{Bmatrix} = \begin{bmatrix} \Psi & 0 & \Psi_{,\xi} \\ 0 & \Psi & \Psi_{,\eta} \end{bmatrix} \begin{Bmatrix} c_3 \\ c_4 \\ c_5 \end{Bmatrix} \qquad (29)$$

The hybrid-stabilization method starts with Hellinger-Reissner hybrid functional. With reference to Eq.(18), the functional can be written as:

$$\Pi^e_{HR} = \sum_{\varphi=m,b,s} \langle -\frac{1}{2}(\underline{\sigma}^\varphi)^T(\underline{\underline{D}}^\varphi)^{-1}\underline{\sigma}^\varphi + (\underline{\sigma}^\varphi)^T\underline{\varepsilon}^\varphi\rangle^e - P^e \qquad (30)$$

in which the vectors of stress components $\underline{\sigma}^\varphi$ is the energy conjugates of $\underline{\varepsilon}^\varphi$. By partitioning the stress into orthogonal lower order "L" and higher order "H" modes, i.e.

$$\underline{\sigma}^\varphi = \underline{\sigma}^\varphi_L + \underline{\sigma}^\varphi_H \quad \text{and} \quad \langle(\underline{\sigma}^\varphi_L)^T(\underline{\underline{D}}^\varphi)^{-1}\underline{\sigma}^\varphi_H\rangle^e = 0\ , \qquad (31)$$

the functional becomes:

$$\Pi_{HR}^{e} = \sum_{\varphi=m,b,s} \langle -\frac{1}{2}(\underline{\sigma}_L^{\varphi})^T (\underline{\underline{D}}^{\varphi})^{-1} \underline{\sigma}_L^{\varphi} + (\underline{\sigma}_L^{\varphi})^T \underline{\varepsilon}^{\varphi} - \frac{1}{2}(\underline{\sigma}_H^{\varphi})^T (\underline{\underline{D}}^{\varphi})^{-1} \underline{\sigma}_H^{\varphi} + (\underline{\sigma}_H^{\varphi})^T \underline{\varepsilon}^{\varphi} \rangle^e - P^e \quad (32)$$

We shall take

$$\underline{\sigma}_L^m = \sum_{i,j=1}^{n_L} G_i(\xi) G_j(\eta) \underline{\alpha}_{ij}^m \ , \ \underline{\sigma}_L^b = \sum_{i,j=1}^{n_L} G_i(\xi) G_j(\eta) \underline{\alpha}_{ij}^b \ , \ \underline{\sigma}_L^s = \sum_{i,j=1}^{n_L} G_i(\xi) G_j(\eta) \underline{\alpha}_{ij}^s \quad (33)$$

where G_i has been defined in (23) and $G_{ij} = \delta_{ij}$; $\underline{\alpha}_{ij}^m$, $\underline{\alpha}_{ij}^b$ and $\underline{\alpha}_{ij}^s$ are the vector with coefficients for the lower order membrane, bending and shear stress components, respectively. As G_i is a degree n_L-1 polynomial, the first two integrands in (32) are up to degrees $2n_L$-1 in ξ and η for regular elements. They can be evaluated by RI using which the first two integrals become

$$\langle -\frac{1}{2}(\underline{\sigma}_L^{\varphi})^T (\underline{\underline{D}}^{\varphi})^{-1} \underline{\sigma}_L^{\varphi} + (\underline{\sigma}_L^{\varphi})^T \underline{\varepsilon}^{\varphi} \rangle_{RGQ} = \sum_{p=1}^{n_L} \sum_{q=1}^{n_L} w_p w_q J_{pq} [-\frac{1}{2}(\underline{\alpha}_{pq}^{\varphi})^T (\underline{\underline{D}}^{\varphi})^{-1} \underline{\alpha}_{pq}^{\varphi} + (\underline{\alpha}_{pq}^{\varphi})^T \underline{\underline{B}}_{pq}^{\varphi} \underline{d} \ ] \quad (34)$$

in which w_p is the weight factor for g_p; J_{pq} and $\underline{\underline{B}}_{pq}^{\varphi}$ denote J_o and $\underline{\underline{B}}^{\varphi}$ at (g_p, g_q), respectively. Variations of (32) with respect to $\underline{\alpha}_{pq}^{\varphi}$ s yield $\underline{\alpha}_{pq}^{\varphi} = \underline{\underline{D}}^{\varphi} \underline{\underline{B}}_{pq}^{\varphi} \underline{d}$ and

$$\langle -\frac{1}{2}(\underline{\sigma}_L^{\varphi})^T (\underline{\underline{D}}^{\varphi})^{-1} \underline{\sigma}_L^{\varphi} + (\underline{\sigma}_L^{\varphi})^T \underline{\varepsilon}^{\varphi} \rangle_{RGQ} = \frac{1}{2} \underline{d}^T \sum_{p=1}^{n_L} \sum_{q=1}^{n_L} w_p w_q J_{pq} (\underline{\underline{B}}_{pq}^{\varphi})^T (\underline{\underline{D}}_{pq}^{\varphi}) \underline{\underline{B}}_{pq}^{\varphi} \underline{d} = \frac{1}{2} \underline{d}^T \underline{\underline{K}}_{RI} \underline{d} \quad (35)$$

where $\underline{\underline{K}}_{RI} = \sum_{\varphi=m,b,s} \langle (\underline{\underline{B}}^{\varphi})^T \underline{\underline{D}}^{\varphi} \underline{\underline{B}}^{\varphi} \rangle_{RGQ}$ is the RI stiffness matrix of the element. Thus, (32) becomes

$$\Pi_{HR}^{e} = \frac{1}{2} \underline{d}^T \underline{\underline{K}}_{RI} \underline{d} + \sum_{\varphi=m,b,s} \langle -\frac{1}{2}(\underline{\sigma}_H^{\varphi})^T (\underline{\underline{D}}^{\varphi})^{-1} \underline{\sigma}_H^{\varphi} + (\underline{\sigma}_H^{\varphi})^T \underline{\varepsilon}^{\varphi} \rangle^e - P^e \quad (36)$$

To fulfill the orthogonality requirement in (31) and be able to stabilize the compatible spurious ZEMs of the RI element, the following $\underline{\sigma}_H^{\varphi}$ s are chosen:

$$\underline{\sigma}_H^m = (\underline{\underline{T}}_{\varepsilon}^0)^{-T} \frac{1}{J_o} \begin{bmatrix} \Psi_{,\xi} & 0 \\ 0 & \Psi_{,\eta} \\ 0 & 0 \end{bmatrix} \underline{\beta}^m \ , \ \underline{\sigma}_H^b = (\underline{\underline{T}}_{\varepsilon}^0)^{-T} \frac{1}{J_o} \begin{bmatrix} \Psi_{,\xi} & 0 \\ 0 & \Psi_{,\eta} \\ 0 & 0 \end{bmatrix} \underline{\beta}^b \ , \ \underline{\sigma}_H^s = (\underline{\underline{T}}_{\gamma}^0)^{-T} \frac{1}{J_o} \begin{bmatrix} \Psi_{,\xi} \\ \Psi_{,\eta} \end{bmatrix} \underline{\beta}^s \quad (37)$$

in which $\underline{\beta}$s are the coefficient vectors for the higher order stress modes. By incorporating (14) and (37) into (36),

$$\Pi_{HR}^{e} = \frac{1}{2} \underline{d}^T \underline{\underline{K}}_{RI} \underline{d} + \sum_{\varphi=m,b,s} [-\frac{1}{2} (\underline{\beta}^{\varphi})^T \underline{\underline{H}}^{\varphi} \underline{\beta}^{\varphi} + (\underline{\beta}^{\varphi})^T \underline{\underline{G}}^{\varphi} \underline{d}] - P^e \quad (38)$$

where $\underline{\underline{H}}$'s and $\underline{\underline{G}}$'s are the flexibility and leverage matrices, respectively. Moreover,

$$\underline{\underline{H}}^{\varphi} = \langle \frac{1}{J_o^2} \begin{bmatrix} \Psi_{,\xi} & 0 \\ 0 & \Psi_{,\eta} \\ 0 & 0 \end{bmatrix}^T (\underline{\underline{T}}_{\varepsilon}^{0})^{-1} (\underline{\underline{D}}^{\varphi})^{-1} (\underline{\underline{T}}_{\varepsilon}^{0})^{-T} \begin{bmatrix} \Psi_{,\xi} & 0 \\ 0 & \Psi_{,\eta} \\ 0 & 0 \end{bmatrix} \rangle^e \quad \text{for } \varphi = m, b;$$

$$\underline{\underline{H}}^{s} = \langle \frac{1}{J_o^2} \begin{bmatrix} \Psi_{,\xi} \\ \Psi_{,\eta} \end{bmatrix}^T (\underline{\underline{T}}_{\gamma}^{0})^{-1} (\underline{\underline{D}}^{s})^{-1} (\underline{\underline{T}}_{\gamma}^{0})^{-T} \begin{bmatrix} \Psi_{,\xi} \\ \Psi_{,\eta} \end{bmatrix} \rangle^e \tag{39}$$

and

$$\underline{\underline{G}}^{m}\underline{d} = \int_{-1}^{+1}\int_{-1}^{+1} \begin{bmatrix} \Psi_{,\xi} (\frac{\partial \underline{X}^{o}}{\partial \xi})^T \frac{\partial \underline{U}^{o}}{\partial \xi} \\ \Psi_{,\eta} (\frac{\partial \underline{X}^{o}}{\partial \eta})^T \frac{\partial \underline{U}^{o}}{\partial \eta} \end{bmatrix} d\xi d\eta \ , \quad \underline{\underline{G}}^{b}\underline{d} = \int_{-1}^{+1}\int_{-1}^{+1} \begin{bmatrix} \Psi_{,\xi} [(\frac{\partial \underline{X}^{n}}{\partial \xi})^T \frac{\partial \underline{U}^{o}}{\partial \xi} + (\frac{\partial \underline{X}^{o}}{\partial \xi})^T \frac{\partial \underline{U}^{n}}{\partial \xi}] \\ \Psi_{,\eta} [(\frac{\partial \underline{X}^{n}}{\partial \eta})^T \frac{\partial \underline{U}^{o}}{\partial \eta} + (\frac{\partial \underline{X}^{o}}{\partial \eta})^T \frac{\partial \underline{U}^{n}}{\partial \eta}] \end{bmatrix} d\xi d\eta \ ,$$

$$\underline{\underline{G}}^{s}\underline{d} = \int_{-1}^{+1}\int_{-1}^{+1} [\ \Psi_{,\xi} (\underline{X}^{n})^T \frac{\partial \underline{U}^{o}}{\partial \xi} + \Psi_{,\eta} (\underline{X}^{n})^T \frac{\partial \underline{U}^{o}}{\partial \eta} + \Psi_{,\xi} (\frac{\partial \underline{X}^{o}}{\partial \xi})^T \underline{U}^{n} + \Psi_{,\eta} (\frac{\partial \underline{X}^{o}}{\partial \eta})^T \underline{U}^{n} \ ] d\xi d\eta \ . \tag{40}$$

It should be remarked that the contribution of $\underline{\varepsilon}^0$ to $\underline{\varepsilon}^b$ has been disregarded in calculating $\underline{\underline{G}}^b$ for simplicity. Using (9) and (28), the above expressions can be written as:

$$\underline{\underline{G}}^{m}\underline{d} = \sum_{i,j,k,l=1}^{n_L+1} \begin{bmatrix} \mathcal{G}_{ik}^{111}\mathcal{G}_{jl}^{000} \\ \mathcal{G}_{ik}^{000}\mathcal{G}_{jl}^{111} \end{bmatrix} (\underline{X}_{ij}^{o})^T \underline{U}_{kl}^{o} \ , \quad \underline{\underline{G}}^{b}\underline{d} = \sum_{i,j,k,l=1}^{n_L+1} \begin{bmatrix} \mathcal{G}_{ik}^{111}\mathcal{G}_{jl}^{000} \\ \mathcal{G}_{ik}^{000}\mathcal{G}_{jl}^{111} \end{bmatrix} [\ (\underline{X}_{ij}^{n})^T \underline{U}_{kl}^{o} + (\underline{X}_{ij}^{o})^T \underline{U}_{kl}^{n} \ ] \ ,$$

$$\underline{\underline{G}}^{s}\underline{d} = \sum_{i,j,k,l=1}^{n_L+1} [\ (\mathcal{G}_{ik}^{101}\mathcal{G}_{jl}^{000} + \mathcal{G}_{ik}^{000}\mathcal{G}_{jl}^{101})(\underline{X}_{ij}^{n})^T \underline{U}_{kl}^{o} + (\mathcal{G}_{ik}^{110}\mathcal{G}_{jl}^{000} + \mathcal{G}_{ik}^{000}\mathcal{G}_{jl}^{110})(\underline{X}_{ij}^{o})^T \underline{U}_{kl}^{n} \ ] \tag{41}$$

in which

$$[\mathcal{G}_{ij}^{111}, \mathcal{G}_{ij}^{000}, \mathcal{G}_{ij}^{101}] = \int_{-1}^{+1} [P'_{n_L}(\xi) L_i'(\xi) L_j'(\xi) \ , \ P_{n_L}(\xi) L_i(\xi) L_j(\xi) \ , \ P'_{n_L}(\xi) L_i(\xi) L_j'(\xi)] d\xi \ \text{ and } \ \mathcal{G}_{ij}^{110} = \mathcal{G}_{ji}^{101}$$

It can be seen that $\mathcal{G}_{ij}$'s are independent of the element geometry and can be precomputed whilst the leverage matrices can be formed by multiplying $\mathcal{G}_{ij}$'s with the nodal vectors $\underline{X}_{ij}^{n}$'s and $\underline{X}_{ij}^{n}$'s. If the sub-parametric formulation which is popular in high order elements is employed for better computational efficiency, the range of the first index in $\mathcal{G}_{ij}$'s can be reduced.

On the other hand, the flexibility matrix can be approximately computed without compromising the patch test fulfillment [16, 45]. Besides the derivatives of Ψ, all terms in the integrands leading to the flexibility matrix are approximated by their counterparts at the element origin. Thus,

$$\underline{\underline{H}}^{\varphi} = \int_{-1}^{+1}\int_{-1}^{+1} \begin{bmatrix} S_{11}^{\varphi}\Psi_{,\xi}\Psi_{,\xi} & S_{12}^{\varphi}\Psi_{,\xi}\Psi_{,\eta} \\ S_{12}^{\varphi}\Psi_{,\xi}\Psi_{,\eta} & S_{22}^{\varphi}\Psi_{,\eta}\Psi_{,\eta} \end{bmatrix} d\xi d\eta = \begin{bmatrix} S_{11}^{\varphi}\mathcal{H} & 0 \\ 0 & S_{22}^{\varphi}\mathcal{H} \end{bmatrix} \quad \text{for } \varphi = m, b,$$

$$\underline{\underline{H}}^s = \int_{-1}^{+1}\int_{-1}^{+1} (S_{11}^s \Psi_{,\xi}\,\Psi_{,\xi} + 2S_{12}^s \Psi_{,\xi}\,\Psi_{,\eta} + S_{22}^s \Psi_{,\eta}\,\Psi_{,\eta})\, d\xi d\eta = (S_{11}^s + S_{22}^s)\mathcal{H} \tag{42}$$

where

$$\underline{\underline{S}}^{\varphi} = [S_{ij}^{\varphi}] = [\frac{1}{J_o}(\underline{\underline{T}}_{\varepsilon}^0)^{-1}(\underline{\underline{D}}^{\varphi})^{-1}\underline{\underline{T}}_{\varepsilon}^0)^{-T}]\Big|_{\xi=\eta=0} \quad \text{for} \quad \varphi = m,\, b;$$

$$\underline{\underline{S}}^{s} = [S_{ij}^{s}] = [\frac{1}{J_o}(\underline{\underline{T}}_{\gamma}^0)^{-1}(\underline{\underline{D}}^{s})^{-1}\underline{\underline{T}}_{\gamma}^0)^{-T}]\Big|_{\xi=\eta=0}\ ,\ \mathcal{H} = \int_{-1}^{+1} P'_{n_L}(\xi)P'_{n_L}(\xi)d\xi \cdot \int_{-1}^{+1} P_{n_L}(\xi)P_{n_L}(\xi)d\xi = \frac{2n_L(n_L+1)}{2n_L+1}\ .$$

It can be seen that the chosen approximations exempt the use of high order numerical integration. By condensing $\underline{\beta}$'s thru $\underline{\underline{H}}^{\varphi}\underline{\beta}^{\varphi} = \underline{\underline{G}}^{\varphi}\underline{d}$, the functional in (36) becomes

$$\Pi_{HR}^e = \frac{1}{2}\underline{d}^T[\underline{\underline{K}}_{RI} + \sum_{i=m,b,s}(\underline{\underline{G}}^{\varphi})^T(\underline{\underline{H}}^{\varphi})^{-1}\underline{\underline{G}}^{\varphi}]\,\underline{d} - P^e \tag{43}$$

The element stiffness matrix is within the square brackets. For better computational efficiency, $\underline{\underline{K}}_{RI}$ can be computed by 1D operations with respect to the set of auxiliary nodes (l_i,g_j) and (g_i,l_j), see Figure 1(b) for the case of cubic element. The coordinates and displacements of the auxiliary nodes are obtained from those of the 2D Lobatto nodes by 1D interpolations. The required $\underline{\underline{K}}_{RI}$, defined with respect to the 2D Lobatto nodes, can then be obtained by transformation. The same technique has also been used in the previous stabilized Lobatto plane and axisymmetric elements [41].

7. Numerical Examples

In this section, most of the numerical examples are conducted to compare the following Lobatto element models:

- LB: the Lobatto element evaluated by LBQ, see Section 3 for details;
- ANS: the ANS Lobatto element, see Section 4 for details;
- ANS*: it is essentially the same as ANS except that the natural membrane shear strain are sampled at the 2D RGQ, see Section 5 for details;
- Stab: the stabilized RI Lobatto element, see Section 6 for details.

Section 7.8 will compare LB with the Lagrange elements using equi-spaced and Chebyshev nodes. The following relative errors would be employed to quantify the element accuracy:

- relative displacement error = $\left[\dfrac{\sum_e \left\langle (\underline{U}^o - (\underline{U}^o)^{ref})^T (\underline{U}^o - (\underline{U}^o)^{ref}) \right\rangle_{LBQ}^e}{\sum_e \left\langle ((\underline{U}^o)^{ref})^T (\underline{U}^o)^{ref} \right\rangle_{LBQ}^e}\right]^{\frac{1}{2}}$

- relative rotation error = $\left[\dfrac{\sum_e \left\langle (\underline{\phi} - \underline{\phi}^{ref})^T (\underline{\phi} - \underline{\phi}^{ref}) \right\rangle_{LBQ}^e}{\sum_e \left\langle (\underline{\phi}^{ref})^T (\underline{\phi}^{ref}) \right\rangle_{LBQ}^e}\right]^{\frac{1}{2}}$

- relative energy error = $\left[\dfrac{\sum_e \sum_{\varphi=m,b,s} \left\langle (\underline{\varepsilon}^{\varphi} - (\underline{\varepsilon}^{\varphi})^{ref})^T \underline{\underline{D}}^{\varphi} (\underline{\varepsilon}^{\varphi} - (\underline{\varepsilon}^{\varphi})^{ref}) \right\rangle_{RGQ}^e}{\sum_e \sum_{\varphi=m,b,s} \left\langle ((\underline{\varepsilon}^{\varphi})^{ref})^T \underline{\underline{D}}^{\varphi} ((\underline{\varepsilon}^{\varphi})^{ref}) \right\rangle_{RGQ}^e}\right]^{\frac{1}{2}}$

where $\underline{\phi} = \{\phi^1, \phi^2\}^T$ and the superscript "*ref*" denotes the reference solutions used to quantify the errors. As nodes and RGQ are often regarded as the super-convergent points for the nodal variables and stress/strain, they are employed to integrate the displacement/rotation and energy errors, respectively. Alternate integration rules are also adopted to evaluate the errors which are supportive to the aforementioned super-convergent features. Furthermore, ANS and ANS* are identical in plate problems. Their predictions are graphically indistinguishable in some shell examples wherein their predictions would not be separately presented.

Analytical solutions would be employed as the reference solutions for square plate and cylindrical shell problems in Sections 6.1 to 6.5. For the hyperbolic shell problem in Section 6.6, highly-converged solution obtained by 1D finite element discretization would be used. The procedures for deriving the reference solutions can be seen in Appendices A to C.

7.1 Hard-simply supported square plate

A $2L \times 2L$ square plate with all its edges hard-simply supported (i.e. $w = \theta_n = 0$ where θ_n is the rotation about the outward normal of the pertinent edge) is considered. The transverse loading is $q = \cos(\alpha x)\sin(\alpha x)$ wherein $\alpha = \pi/(2L)$. Owing to symmetry, only a quarter of the plate is analyzed as shown in Figure 7. The domain is meshed into $m \times m$ elements where m = 2, 4, 8 and 16. The parameters are $E = 10^6$, $\nu = 0.3$ and $t = 0.1$ or 0.001. The analytical solution for this problem is [51]:

$$w^{exact} = \left(\frac{1}{4D\alpha^4} + \frac{1}{2C\alpha^2}\right)\cos(\alpha x)\cos(\alpha y)\ ,\ \begin{Bmatrix}\phi_x \\ \phi_y\end{Bmatrix}^{exact} = \frac{1}{4D\alpha^3}\begin{Bmatrix}\sin(\alpha x)\cos(\alpha y) \\ \cos(\alpha x)\sin(\alpha y)\end{Bmatrix} \qquad (44)$$

where

$$D = \frac{Et^3}{12(1-\nu^2)} \quad \text{and} \quad C = kGt\,. \tag{45}$$

Figure 8(a), (b) and (c) plot result for elements of order n_L = 2, 3 and 4, respectively. It can be seen that ANS and Stab are 10 to 5000 times more accurate than LB. Moreoever, when t/L changes from 0.1 to 0.001, both the accuracy and convergence rate of LB deteriorate. On the other hand, the accuracy and convergent rate of ANS and Stab are virtually unaffected by the value of t/L.

7.2 Hard-simply supported square plate with distorted mesh

In this section, the previous example is re-analyzed with distorted mesh as shown in Figure 9. The ratio of the element edges is L_1: L_2: L_3: … L_m = 1: 2: 3: …m [9]. Figure 10(a), (b) and (c) plot the result for elements of n_L = 2, 3 and 4, respectively. From Figure 10(a) and (b) for n_L = 2 and 3, it can be seen that the displacement errors of ANS and Stab are close when t/L = 0.1. In all other cases, the ANS is more accurate than Stab and LB in turn. ANS is virtually unaffected by the value of t/L but the predictions of Stab and LB deteriorate when t/L changes from 0.1 to 0.001. Owing to the mesh distortion, the relative errors in Figure 10 are typically one order lager than those in Figure 8. Though the accuracy of Stab deterioates with the mesh distortion, it is still more accurate than LB in all cases.

7.3 Square plate with boundary layer effect

The square plate to be considered is shown in Figure 11 [51]. The edges at x = 0 and L are hard-simply supported. The edges at $y = \pm L/2$ are either clamped or free. The applied transverse loading is $q = q_0 \sin(\pi x/L)$. Other parameters are $E = 10^6$, $\nu = 0.3$, L = 1 and t = 0.1 or 0.01. Along $y = \pm L/2$, the plate will exhibit boundary layer effect and the layer width is in the order of the thickness [52]. Owing to symmetry, only a quarter of the plate is analyzed and meshed into $m \times 2m$ elements, see Figure 11(b). To better capture the boundary layer effect, b is taken to be 0.2 and 0.04 for t = 0.1 and 0.01, respectively. The analytical shear force Q_x and twisting moment M_{xy} along x = 0 in Appendix A are plotted in Figure 12 and 13 when the edges at $y = \pm L/2$ are clamped and free, respectively. The sharp changes in Q_x and/or M_{xy} at the points close to $y = \pm L/2$ illustrate the boundary layer effect.

The plate with clamped edges is first considered. Figure 14(a), (b) and (c) show the results for element orders n_L = 2, 3 and 4, respectively. The predictions of ANS and Stab are close. They are markedly more accurate than those of LB for lower n_L and smaller thickness. Also, they are less sensitive to the thickness change. The plate with free edges is then considered. Figure 15(a), (b) and (c) show the results for element orders n_L = 2, 3 and 4, respectively. The observations are similar to those of the plate with clamped edges. However, the error of LB is less affected by the thickness change. This is well expected as the plate with free edges is less constrained than the plate with

clamped edges. Shear locking is less serious.

7.4 Cylindrical shell under pressure

In this example, the cylindrical shell of radius R, length $2L$ and thickness t as shown in Figure 16 is subjected to pressure loading $p = p_0 \cos(2\theta)$ wherein $p_0 = 1$ [9, 53, 54]. Other parameters include $E = 2\times10^5$, $v = 1/3$, $R = L = 1$ and $t = 0.01$ and 0.0001. The cases in which the two ends of the shell are both clamped and both free are considered. Based on the loading and boundary conditions, the displacements and rotations assume the following parametric forms:

$$\begin{Bmatrix} u_X \\ u_\theta \\ u_r \end{Bmatrix} = \begin{Bmatrix} u(X)\cos(a\theta) \\ v(X)\sin(a\theta) \\ w(X)\cos(a\theta) \end{Bmatrix}, \quad \begin{Bmatrix} \phi_X \\ \phi_\theta \end{Bmatrix} = \begin{Bmatrix} \alpha(X)\cos(a\theta) \\ \beta(X)\sin(a\theta) \end{Bmatrix} \tag{46}$$

After integrating with respect to θ, the total potential depends only on X and the analytical solution can be derived, see Appendix B. The analytical membrane and bending strains along $\theta = 0$ at $t = 0.01$ and 0.0001 for clamped ends are shown in Figure 17 whilst those for free ends are shown in Figure 18. The ratios of the membrane to bending energy are given below:

For $t = 0.01$, the ratios are 50.6 and 2.18×10^{-3} for clamped and free ends, respectively;

For $t = 0.0001$, the ratios are 1.23×10^3 and 0.218×10^{-3} for clamped and free ends, respectively.

Thus, the clamped-ends and free-ends cases are dominated by membrane and bending energies, respectively. The boundary zone of width in the order of $\sqrt{t}$ is strongly affected by the boundary layer effect [53, 54]. This fact is well-echoed in Figures 17 and 18 in which the two strains go up abruptly at around 0.1 and 0.01 from the cylinder end. Owing to symmetry, only one eighth of the cylinder is modelled by $m\times m$ elements where $m = 4$, 8, 16 and 32. To capture the boundary layer effect, half of the elements are employed to model the region of width b next to the cylinder end, see Figure 16(b), whilst b is taken to be 0.2 and 0.05 for $t = 0.01$ and $t = 0.0001$, respectively.

For the shell with clamped ends, the error plots for elements of order $n_L = 2$, 3 and 4 are given in Figure 19. When $t = 0.01$, it can be seen that the ANS, ANS* and Stab yield close results which are much more accurate than those of LB. When $t = 0.0001$, the displacement and rotation errors of Stab and ANS* are larger than those of LB under coarse meshes. For $n_L = 2$, the accuracy of ANS is slightly better and worse than ANS* and LB, respectively, under coarse meshes. For $n_L = 3$ and 4, ANS is most accurate in nearly all error measures. The deterioration in ANS, ANS* and Stab is caused by the oscillation in the predicted displacement/rotations. Figure 20 illustrates the oscillation for the 3rd order ANS* for $m = 4$ and $t = 0.0001$. However, the oscillation diminishes at higher mesh density whereat the displacement and rotation predictions of ANS, ANS* and Stab catch up with those of

LB. On the other hand, the energy predictions of Stab and ANS improve much faster than the displacement and rotation predictions.

For the shell with free ends, the errors plots for elements of order n_L = 2, 3 and 4 are given in Figure 21. Figure 21(a) shows that the quadratic LB element locks severely. As the element order goes up, the result of LB improves. On the other hand, the predictions of Stab and ANS are much better than that of LB and they are less sensitive to the change in thickness. From Figures 21(b) and (c) for element order n_L = 3 and 4, Stab produces more accurate displacement result than ANS while ANS is slightly more accurate than Stab in rotation and energy for t = 0.01. When t = 0.0001, the results of ANS and Stab are close. The accuracy of ANS and Stab at t = 0.0001 are better than those at t = 0.01. However, one should also recall that the meshes at the two thicknesses are different (i.e. b = 0.2 and 0.05 for t = 0.01 and 0.0001, respectively) and the boundary layer effect is also thickness dependent. Predictions of ANS* are graphically indistinguishable from those of ANS and, thus, are not shown separately.

7.5 Cylindrical shell with distorted mesh

In this section, the cylindrical shell problem subjected to the same pressure loading is employed to study the element performance under distorted mesh. To avoid the interplay of the thickness-dependent boundary layer effect with the element distortion, the two ends of the cylindrical shell are prescribed with symmetric boundary conditions, i.e. U_X^0 and ϕ^1 shown in Figure 16 are restrained. The analytical solutions for the non-zero displacement and rotation components are

$$\begin{Bmatrix} U_Y^0 \\ U_Z^0 \end{Bmatrix} = \frac{2p_0R^2}{9}\left(\frac{1}{C}+\frac{R^2}{4D}\right)\begin{Bmatrix} 2\cos(2\theta)\sin(\theta)-\sin(2\theta)\cos(\theta) \\ 2\cos(2\theta)\cos(\theta)+\sin(2\theta)\sin(\theta) \end{Bmatrix},\ \phi^2 = \frac{p_0R^3}{6D}\sin(2\theta) \qquad (47)$$

which are independent of X. Both regular and distorted elements are set up. Following the practice of Reference [9], the distorted $m\times m$ mesh shown in Figure 22 with L_1: L_2: L_3: … L_m = 1: 2: 3: …m is employed. In this problem, the analytical membrane energy is zero regardless of the thickness.

The result based on the regular mesh is first presented. The result for n_L = 2 is shown in Figure 23(a). Predications of ANS and Stab are several order more accurate than LB in all the error measures. The accuracy of LB deteriorates severely when the thickness changes from 0.01 to 0.0001 while those of ANS and Stab remain virtually intact. Besides, the predictions of ANS and Stab are close. Similar trend is observed in Figures 23(b) and (c) for n_L = 3 and 4, respectively.

Next, the result based on the distorted mesh is considered. Figures 24(a), (b) and (c) plot the errors for n_L = 2, 3 and 4, respectively. Overall speaking, ANS* is close to but marginally more accurate than Stab. ANS is considerable and marginally more accurate than LB for t = 0.01 and t = 0.0001,

respectively. The predications of all elements deteriorate when thickness changes from t = 0.01 to t = 0.0001.

7.6 Hyperbolic shell under pressure

The hyperbolic shell in Figure 25 with mid-surface given by $X^2 + Z^2 = 1 + Y^2$ is loaded by the harmonic pressure $p(\theta) = p_0 \cos(2\theta)$ [7, 9, 55]. Owing to symmetry, one-eighth of the shell ($-1 \le Y \le 0$; $0 \le \theta \le \pi/2$) is meshed into $m \times m$ elements where m = 4, 8, 16 and 32. Symmetric boundary conditions are applied along the edges AB, BC and CD, see Figure 25(b). To better capture the boundary effect, half of the elements are used to model the regions within $6\sqrt{t}$ and $0.5\sqrt{t}$ from the clamped and free AD, respectively [7, 9]. Regarding the reference solution, the following parametric forms can be assumed as a result of the loading and the boundary conditions:

$$\begin{Bmatrix} u_Y \\ u_\theta \\ u_r \end{Bmatrix} = \begin{Bmatrix} u(Y)\cos(a\theta) \\ v(Y)\sin(a\theta) \\ w(Y)\cos(a\theta) \end{Bmatrix}, \quad \begin{Bmatrix} \phi_x \\ \phi_\theta \end{Bmatrix} = \begin{Bmatrix} \alpha(Y)\cos(a\theta) \\ \beta(Y)\sin(a\theta) \end{Bmatrix} \tag{48}$$

After integrating with respect to θ, the potential energy functional is Y-dependent. Though analytical solution cannot be derived, highly converged reference solutions can be obtained very efficiently by 1D finite element discretization, see Appendix C. The solutions are here obtained by 64 sixth order 1D elements with, again, half of the elements employed in the regions within $6\sqrt{t}$ and $0.5\sqrt{t}$ from the clamped and free AD, respectively. The membrane and bending shear strains in the reference solutions are plotted in Figures 26 and 27 for clamped and free ends, respectively. The ratios of the membrane to bending energy are given below:

For t = 0.01, the ratios are 23.1 and 8.39×10^{-3} for clamped and free ends, respectively;

For t = 0.0001, the ratios are 285 and 1.50×10^{-6} for clamped and free ends, respectively.

Same as the cylindrical shell in Section 6.4, the problem is dominated by membrane and bending energies when the two ends are clamped and free, respectively. For the case with clamped ends, the error plots for n_L = 2, 3 and 4 are given in Figures 28(a), (b) and (c), respectively. The predictions of ANS and ANS* almost overlap except for the displacement and rotation errors under t = 0.0001 and n_L = 2 and 3. The predictions of quartic ANS and ANS* are graphically indistinguishable. For thickness t = 0.01, ANS/ANS* and Stab yield similar result in displacement and energy while the rotation error of ANS/ANS* gradually becomes lower than that of Stab after mesh refinement. Oscillations similar to but less severe than those of the cylindrical shell with clamped ends are observed for Stab and ANS/ANS* under coarse mesh when t = 0.0001. Among the advanced models, Stab is least accurate in this example. Overall speaking, ANS is marginally more accurate than ANS*.

For the case with free ends, the error plots for n_L = 2, 3 and 4 are presented in Figures 29(a), (b)

and (c), respectively. At t = 0.0001, the problem is highly dominated by bending energy which is nearly 1 million times larger than the membrane energy. The relative accuracy of the elements are similar to that of the cylinder shell problem under symmetric end conditions, wherein the membrane energy is zero, and modelled by distorted mesh in Section 7.5. Stab and ANS* are markedly more accurate than ANS. The quadratic LB suffers from locking which is relieved to some extent by increasing element order to 3 and 4.

7.7 Eigen Frequencies of a Free Cylindrical Shell Panel

Eigen frequencies for the cylinder shell panel which is geometrically the same as ABCD in Figure 16(a) are computed. The panel is free, i.e., none of the nodal dofs is restrained. The material parameters are $E = 200\times10^3$, $\nu = 1/3$ and $\rho = 1$. The problem domain is meshed uniformly into 4×4 quadratic elements or 2×2 quartic elements. Thus, the number of nodes is kept at 9 nodes along each side of the domain. The element mass matrix is

$$\underline{\underline{M}} = \langle (\underline{\underline{N}})^T \, \underline{\underline{m}} \underline{\underline{N}} \rangle^e_{LBQ} \quad \text{with} \quad \underline{\underline{m}} = diag.\{\rho t, \rho t, \rho t, \rho t^3/12, \rho t^3/12\}.$$

Recalling that LBQ is a nodal integration, the assembled mass matrix is diagonal. The eigen frequencies predicted by 4×4 sixth order LB elements are also computed for reference. Figure 30 plots the lowest 20 non-zero eigen frequencies in increasing order. The predictions of Stab and ANS* are close to the reference solution. Those of LB and ANS are respectively much and slightly higher than the reference solution, indicating that they are too stiff. On the other hand, the maximum eigen frequencies of all elements are very close. In other words, the advanced formulation can soften the element stiffness but do not enable a large stable time increment in explicit time integration.

7.8 Comparisons with other Lagrange Elements

This subsection will compare LB with Lagrange elements EQ and CB which use equi-spaced and Chebyshev nodes, respectively, and integrated by FGQ. Figure 31 shows the errors of the third order elements in the hard-simply supported square plate problems considered in Sections 7.1 and 7.2. Figure 32 shows the errors of the third order elements in the cylindrical shell problem with symmetry end conditions considered in Section 7.5. At t = 0.1, EQ and CB are slightly more accurate than LB regardless whether regular or distorted meshes are used. At t = 0.001, the accuracy of EQ and CB are still close to but not necessarily slightly higher than that of LB. By contrasting Figures 31(a), 31(b), 32(a) and 32(b) with respectively Figures 8(b), 10(b), 23(b) and 24(b), one can see that EQ and CB are far less accurate than some of the proposed elements. As a matter of fact, when the third order LB element is also evaluated by FGQ, its predictions are identical to that of EQ and CB. This point is not surprising as all LB (evaluated by FGQ), EQ and CB employ the same solution basis and integration

rule. They should yield the same prediction before the Runge phenomenon [4] occurs. However, LB enjoys higher popularity because it is considerably more efficient than EQ and CB by virtue of the tensor product feature of the nodal interpolation at the LBQ points. The aforementioned observations on the relative accuracy of LB, EQ and CB on cubic elements also applicable to the fourth order elements.

8. Closure

In this paper, assumed natural strain (ANS) and stabilization schemes are developed for quadrilateral Lobatto C^0 plate/shell problems. It is noted that the reduced order Gaussian quadrature (RGQ) points are the super-convergent points of the Lobatto (LB) nodes. Two ANS schemes are devised. Both the schemes sample and interpolate the natural membrane normal and transverse shear strain components at the 1D RGQ points along the nodal lines whilst all the bending strain components are directly sampled at the nodes. In the first ANS scheme, the natural membrane shear strain is also sampled at the LB nodes. In the second ANS scheme, the natural membrane shear strain is sampled at the 2D RGQ. Hence, the first scheme only requires 1D operations. The stabilization scheme is generalized from the hybrid-stabilization method for reduced-integrated elements. It is based on the Hellinger-Reissner functional with orthogonal lower and higher order stress-resultant modes. Regardless of the element order, five higher order stress-resultant modes are sufficient to suppress all the compatible spurious zero energy modes. The stabilization vectors can be pre-derived in terms of the element nodal information for better computational efficiency. Though all the three schemes are developed with respect to LB elements, they are equally applicable to other quadrilateral Lagrange elements.

For plate and moderately thick-shell problems, the three schemes yield similar results which are considerably more accurate than those yielded by the conventional LB elements. For thin-shell problems dominated by bending energy and modelled, or needed to be modelled, by geometrically complicated meshes, the second ANS and the stabilization schemes are close in accuracy and significantly more accurate than the first ANS scheme and the conventional Lobatto elements. For the thin-shell problems dominated by membrane energy and exhibiting boundary effect, oscillations occur in the predictions of the advanced elements when coarse meshes are employed. At finer meshes, the oscillations disappear and the advanced elements often become more accurate than the conventional LB. Similar oscillations also occur in other advanced models [8, 54]. While the first ANS scheme is least accurate in bending-dominated thin-shell problems among the three scheme, it is essentially the most accurate one in problems dominated by membrane energy and exhibiting boundary effect.

The three schemes can readily be used in solid-shell elements. Their predictions are essentially identical to those of the present C^0 shell elements and are not repeated here.

Acknowledgment – This work was supported by the Hong Kong Research Grant Council in the form of a GRF Grant (HKU 7168 13E). Some of the presented results are extracted from the thesis of the second author [42].

References

[1] Park K, Stanley G, A curved C0 shell element based on assumed natural-coordinate strains, Journal of Applied Mechanics, 53 1986 278-290.

[2] Jang J, Pinsky PM, An assumed covariant strain based 9-node shell element, International Journal for Numerical Methods in Engineering, 24 1987 2389-2411.

[3] Sze KY, Zhu D, Quadratic assumed natural strain curved triangular shell element, Computer Methods in Applied Mechanics and Engineering, 174 1999 57-71.

[4] Pozrikidis C, Introduction to finite and spectral element methods using MATLAB: CRC Press, 2005.

[5] Bathe K-J, Dvorkin EN, A four-node plate bending element based on Mindlin/Reissner plate theory and a mixed interpolation, International Journal for Numerical Methods in Engineering, 21 1985 367-383.

[6] Bucalem ML, Bathe K-J, Higher-order MITC general shell elements, International Journal for Numerical Methods in Engineering, 36 1993 3729-3754.

[7] Bathe K-J, Lee P-S, Hiller J-F, Towards improving the MITC9 shell element, Computers & Structures, 81 2003 477-489.

[8] da Veiga LB, Chapelle D, Suarez IP, Towards improving the MITC6 triangular shell element, Computers & Structures, 85 2007 1589-1610.

[9] Lee Y, Lee P-S, Bathe K-J, The MITC3+ shell element and its performance, Computers and Structures, 138 2014 12-23.

[10] Zienkiewicz O, Taylor R, Too J, Reduced integration technique in general analysis of plates and shells, International Journal for Numerical Methods in Engineering, 3 1971 275-290.

[11] Malkus DS, Hughes TJR, Mixed finite element methods—reduced and selective integration techniques: a unification of concepts, Computer Methods in Applied Mechanics and Engineering, 15 1978 63-81.

[12] Brito KD, Sprague MA, Reissner–Mindlin Legendre spectral finite elements with mixed reduced quadrature, Finite Elements in Analysis and Design, 58 2012 74-83.

[13] Lee SW, Pian THH, Improvement of plate and shell finite elements by mixed formulations, AIAA journal, 16 1978 29-34.

[14] Rhiu JJ, Lee SW, A sixteen node shell element with a matrix stabilization scheme, Computational mechanics, 3 1988 99-113.

[15] Rhiu JJ, Lee SW, Russell M, Two higher-order shell finite elements with stabilization matrix, AIAA journal, 28 1990 1517-1524.

[16] Sze KY, An explicit hybrid-stabilized 9-node Lagrangian shell element, Computer methods in applied mechanics and engineering, 117 1994 361-379.

[17] Kim K, Cho C, Lee SW, An assumed strain nin-node solid shell element with improved performance, Computer Modelling in Engineering and Science, 2 2002 339-349.

[18] Batoz JL, Bathe KJ, Ho LW, Study of three-node triangular plate bending elements, International Journal for Numerical Methods in Engineering, 15 1980 1771-1812.

[19] Batoz J, Zheng C, Hammadi F, Formulation and evaluation of new triangular, quadrilateral, pentagonal and hexagonal discrete Kirchhoff plate/shell elements, International journal for numerical methods in engineering, 52 2001 615-630.

[20] Belytschko T, Wong BL, Stolarski H, Assumed strain stabilization procedure for the 9-node Lagrange shell element, International Journal for Numerical Methods in Engineering, 28 1989 385-414.

[21] Belytschko T, Tsay CS, A stabilization procedure for the quadrilateral plate element with one-point quadrature, International Journal for Numerical Methods in Engineering, 19 1983 405-419.

[22] Mostafa M, Sivaselvan M, Felippa C, A solid-shell corotational element based on ANDES, ANS and EAS for geometrically nonlinear structural analysis, International Journal for Numerical Methods in Engineering, 95 2013 145-180.

[23] Huang HC, Hinton E, A new nine node degenerated shell element with enhanced membrane and shear interpolation, International Journal for Numerical Methods in Engineering, 22 1986 73-92.

[24] Hinton E, Huang HC, A family of quadrilateral Mindlin plate elements with substitute shear strain fields, Computers & structures, 23 1986 409-431.

[25] Militello C, Felippa CA, First ANDES elements: 9-Dof plate bending triangles, Computer Methods in Applied Mechanics and Engineering, 93 1991 217-246.

[26] Bletzinger K-U, Bischoff M, Ramm E, A unified approach for shear-locking-free triangular and rectangular shell finite elements, Computers & Structures, 75 2000 321-334.

[27] Simo JC, Rifai MS, A class of mixed assumed strain methods and the method of incompatible modes, International Journal for Numerical Methods in Engineering, 29 1990 1595-1638.

[28] Simo JC, Armero F, Geometrically non-linear enhanced strain mixed methods and the method of incompatible modes, International Journal for Numerical Methods in Engineering, 33 1992 1413-1449.

[29] Caseiro J, De Sousa RA, Valente R, A systematic development of EAS three-dimensional finite elements for the alleviation of locking phenomena, Finite Elements in Analysis and Design, 73 2013 30-41.

[30] Patera AT, A spectral element method for fluid dynamics: Laminar flow in a channel expansion, Journal of Computational Physics, 54 1984 468-488.

[31] Dauksher W, Emery AF, Accuracy in modeling the acoustic wave equation with Chebyshev spectral finite elements, Finite Elements in Analysis and Design, 26 1997 115-128.

[32] Komatitsch D, Vilotte JP, The spectral element method: An efficient tool to simulate the seismic response of 2D and 3D geological structures, Bulletin of the Seismological Society of America, 88 1998 368-392.

[33] Dauksher W, Emery AF, The solution of elastostatic and elastodynamic problems with Chebyshev spectral finite elements, Computer methods in applied mechanics and engineering, 188 2000 217-233.

[34] Komatitsch D, Tsuboi S, Tromp J, The spectral-element method in seismology, Geophysical Monograph Series, 157 2005 205-227.

[35] Kudela P, Żak A, Krawczuk M, Ostachowicz W, Modelling of wave propagation in composite plates using the time domain spectral element method, Journal of Sound and Vibration, 302 2007 728-745.

[36] Sprague M, Geers T, Legendre spectral finite elements for structural dynamics analysis, Communications in Numerical Methods in Engineering, 24 2008 1953-1965.

[37] Kim Y, Ha S, Chang F-K, Time-domain spectral element method for built-in piezoelectric-actuator-induced lamb wave propagation analysis, AIAA journal, 46 2008 591-600.

[38] Xing Y, Liu B, High-accuracy differential quadrature finite element method and its application to free vibrations of thin plate with curvilinear domain, International journal for numerical methods in engineering, 80 2009 1718-1742.

[39] Żak A, A novel formulation of a spectral plate element for wave propagation in isotropic structures, Finite Elements in Analysis and Design, 45 2009 650-658.

[40] Brigham JC, Aquino W, Aguilo MA, Diamessis PJ, A spectral finite element approach to modeling soft solids excited with high-frequency harmonic loads, Computer methods in applied mechanics and engineering, 200 2011 692-698.

[41] Hu YC, Sze KY, Zhou YX, Stabilized plane and axisymmetric Lobatto finite element models, Computational Mechanics, 56 2015 879-903.

[42] Hu YC, Formulation of Advanced Lobatto Finite Elements for Structural Analyses, Ph.D. thesis, in: The University of Hong Kong, 2016.

[43] Barlow J, More on optimal stress points - reduced integration, element distortions and error estimation, International Journal for Numerical Methods in Engineering, 28 1989 1487-1504.

[44] MacNeal RH, Finite elements: their design and performance, New York: Marcel Dekker Inc., 1994.

[45] Sze KY, Admissible matrix formulation - from orthogonal approach to explicit hybrid stabilization, Finite elements in analysis and design, 24 1996 1-30.

[46] Orszag SA, Spectral methods for problems in complex geometries, Journal of Computational Physics, 37 1980 70-92.

[47] Melenk JM, Gerdes K, Schwab C, Fully discrete hp-finite elements: Fast quadrature, Computer Methods in Applied Mechanics and Engineering, 190 2001 4339-4364.

[48] Bathe K-J, Finite element procedures: New York: Prentice Hall, 1996.

[49] Belytschko T, Leviathan I, Physical stabilization of the 4-node shell element with one point quadrature, Computer Methods in Applied Mechanics and Engineering, 113 1994 321-350.

[50] Gruttmann F, Wagner W, A linear quadrilateral shell element with fast stiffness computation, Computer Methods in Applied Mechanics and Engineering, 194 2005 4279-4300.

[51] Wang CM, Lim GT, Reddy JN, Lee KH, Relationships between bending solutions of Reissner and Mindlin plate theories, Engineering Structures, 23 2001 838-849.

[52] Häggblad B, Bathe KJ, Specifications of boundary conditions for Reissner/Mindlin plate bending finite elements, International Journal for Numerical Methods in Engineering, 30 1990 981-1011.

[53] Pitkaranta J, Leino Y, Ovaskainen O, Piila J, Shell deformation states and the finite element method: a benchmark study of cylindrical shells, Computer Methods in Applied Mechanics and Engineering, 128 1995 81-121.

[54] Bathe K-J, Iosilevich A, Chapelle D, An evaluation of the MITC shell elements, Computers and Structures, 75 2000 1-30.

[55] Hakula H, hp-boundary layer mesh sequences with applications to shell problems, Computers & Mathematics with Applications, 67 2014 899-917.

[56] Hu HC, Variational principles of theory of elasticity with applications: Science press, Gordon and Breach, Science publisher: Beijing, 1984.

[57] Chapelle D, Bathe K-J, The mathematical shell model underlying general shell elements, International Journal for Numerical Methods in Engineering, 48 2000 289-313.

[58] Malinen M, On the classical shell model underlying bilinear degenerated shell finite elements, International Journal for Numerical Methods in Engineering, 52 2001 389-416.

Appendix A: Analytical solutions for C^0 square plate problems

In this appendix, the analytical solution for the square plate with one pair of opposite edges hard-simply supported is presented. The boundary conditions on other pair of edges are given arbitrarily. The displacement components for the C^0 plate can be expressed as

$$u = z\phi_x(x,y)\,,\quad v = z\phi_y(x,y)\,,\quad w = w(x,y)\,. \tag{A1}$$

For isotropic C^0 plate under transverse loading, the deflection and rotations satisfying the equilibrium equations can be expressed as [56]:

$$w = F - \frac{D}{C}\nabla^2 F,\quad \phi_x = -\frac{\partial F}{\partial x} - \frac{\partial f}{\partial y},\quad \phi_y = -\frac{\partial F}{\partial y} + \frac{\partial f}{\partial x} \tag{A2}$$

In the relations, D and C have been defined in (45) whilst F and f satisfy

$$D\nabla^4 F = q\ ,\ \frac{t^2}{12k}\nabla^2 f - f = 0 \tag{A3}$$

where q is the transverse loading and k is the shear corrector factor, see (17). With $q = q_o \sin(\alpha x)$ and $\alpha = \pi/L$, F and f can be expressed as:

$$F = Y(y)\sin(\alpha x)\ ,\ f = Q(y)\cos(\alpha x)\,. \tag{A4}$$

using which the boundary conditions $w = \phi_y = M_x = 0$ at $x = 0, L$ are satisfied. Substitution of (A4) into (A3) gives

$$\alpha^4 Y - 2\alpha^2\frac{d^2Y}{dy^2} + \frac{d^4Y}{dy^4} = \frac{q_0}{D}\ ,\ \frac{d^2Q}{dy^2} - \alpha_t^2 Q = 0\,. \tag{A5}$$

where $\alpha_t = \sqrt{\alpha^2 + 12k/t^2}$. The solutions of Y and Q are

$$Y = \frac{q_0}{D\alpha^4} + A_1\exp(\alpha y) + A_2\exp(-\alpha y) + y\left[A_3\exp(\alpha y) + A_4\exp(-\alpha y)\right]\ ,$$

$$Q = A_5\exp(\alpha_t y) + A_6\exp(-\alpha_t y) \tag{A6}$$

in which A_i's are unknown coefficients. Using the six boundary conditions ($w = \phi_x = \phi_y = 0$ for clamped edges; $M_y = M_{xy} = Q_y = 0$ for free edges) at $y = \pm L/2$, the coefficients A_is and, thus, the analytical solution can be solved.

The expansion of $\exp(\alpha_t y)$ about $y = +L/2$ up to the linear term of y is $\exp(\alpha_t L/2)\cdot[1\text{-}\alpha_t(L/2\text{-}y)]$. The expression equals zero as $L/2\text{-}y = 1/\alpha_t$. For small thickness, $1/\alpha_t \approx t/\sqrt{(12k)}$ which indicates that the characteristic length of the boundary layer is in the order of thickness.

Interested readers may contact the senior author for the Matlab code leading to the reference solution.

Appendix B: Analytical Solutions for Cylindrical Shell Problems

In this appendix, the analytical solution for the cylinder shell in Figure 16 under the harmonic pressure

$$p(\theta) = p_0 \cos(a\theta) \tag{B1}$$

where a = 2 will be derived for the C^0 shell formulation introduced in Section 3. The solution was constructed based on the classical 2D shell models using the exact geometry [53]. More recently, the 2D shell models underlying the degenerate shell formulations has been investigated [57, 58]. In the following, the physical strains for the cylindrical shell will be derived in line with the formulations in Section 3 and the analytical solutions arise from the variation of the total potential. Using X and θ to describe the geometry of the shell, we have

$$\underline{X}^o = \begin{Bmatrix} X \\ R\sin(\theta) \\ R\cos(\theta) \end{Bmatrix}, \quad \underline{X}^n = \frac{t}{2}\begin{Bmatrix} 0 \\ \sin(\theta) \\ \cos(\theta) \end{Bmatrix}. \tag{B2}$$

From the applied loading and the supporting conditions, the mid-surface displacement and rotation components with respect to the cylindrical coordinates can be expressed as [53]:

$$\begin{Bmatrix} u_X \\ u_\theta \\ u_r \end{Bmatrix} = \begin{Bmatrix} u(X)\cos(a\theta) \\ v(X)\sin(a\theta) \\ w(X)\cos(a\theta) \end{Bmatrix}, \quad \begin{Bmatrix} \phi_X \\ \phi_\theta \end{Bmatrix} = \begin{Bmatrix} \alpha(X)\cos(a\theta) \\ \beta(X)\sin(a\theta) \end{Bmatrix}. \tag{B3}$$

Thus,

$$\underline{U}^o = u_X \underline{e}_X + u_\theta \underline{e}_\theta + u_r \underline{e}_r \ , \quad \underline{U}^n = \phi_X \frac{t}{2}\underline{e}_X + \phi_\theta \frac{t}{2}\underline{e}_\theta \tag{B4}$$

in which

$$\underline{e}_X = \{1,0,0\}^T, \ \underline{e}_\theta = \{0,\cos\theta,-\sin\theta\}^T \ , \ \underline{e}_r = \{0,\sin\theta,\cos\theta\}^T \tag{B5}$$

are the unit base vectors of the cylindrical coordinates. By taking $\xi = X$ and $\eta = \theta$ in (11a-e), covariant strain components with respect to (X,θ,ζ) can be derived as:

$$\varepsilon^0_{XX} = u'\cos(a\theta), \ \varepsilon^0_{\theta\theta} = R(w+av)\cos(a\theta), \ \gamma^0_{X\theta} = (-au+Rv')\sin(a\theta),$$

$$\varepsilon^1_{XX} = \frac{t}{2}\alpha'\cos(a\theta), \ \varepsilon^1_{\theta\theta} = \frac{t}{2}(av+w+aR\beta)\cos(a\theta), \ \gamma^1_{X\theta} = \frac{t}{2}(v'-a\alpha+R\beta')\sin(a\theta),$$

$$\gamma_{X\zeta} = \frac{t}{2}(w'+\alpha)\cos(a\theta), \ \gamma_{\theta\zeta} = \frac{t}{2}(-v-aw+R\beta)\sin(a\theta) \ . \tag{B6}$$

Let (x, y, z) be the local Cartesian coordinates with its base vectors ($\underline{e}_X$, $\underline{e}_\theta$, $\underline{e}_r$) thus

$$x_{,X} = 1; \ y_{,\theta} = \underline{e}_\theta^T \frac{\partial \underline{X}}{\partial \theta} = R + \frac{t}{2}\zeta; \ z_{,\zeta} = \frac{t}{2} \quad \text{and} \quad J_0 = (x_{,Y}\, y_{,\theta}\, z_{,\zeta})\big|_{\zeta=0} = R\frac{t}{2} \tag{B7}$$

Since the coordinates are orthogonal,

$$\theta_{,y} = (y_{,\theta})^{-1} = (R + \frac{t}{2}\zeta)^{-1} = \frac{1}{R} - \frac{t}{2R^2}\zeta + 0(\zeta^2),\ X_{,x} = (x_{,X})^{-1} = 1,\ \zeta_{,z} = (z_{,\zeta})^{-1} = \frac{2}{t} \quad \text{(B8)}$$

and the strain transformation matrixes are

$$\underline{\underline{T}}_{\varepsilon}^{0} = diag.\{1, \frac{1}{R^2}, \frac{1}{R}\},\ \underline{\underline{T}}_{\varepsilon}^{1} = diag.\{0, -\frac{t}{R^3}, -\frac{t}{2R^2}\},\ \underline{\underline{T}}_{\gamma}^{0} = diag.\{\frac{2}{t}, \frac{2}{Rt}\} \quad \text{(B9)}$$

Though (12a,b), the physical strains can be derived to be

$$\varepsilon_{xx}^{m} = u'\cos(a\theta),\ \varepsilon_{yy}^{m} = \frac{1}{R}(av + w)\cos(a\theta),\ \gamma_{xy}^{m} = \frac{1}{R}(-au + Rv')\sin(a\theta),$$

$$\varepsilon_{xx}^{b} = \frac{t}{2}\alpha'\cos(a\theta),\ \varepsilon_{yy}^{b} = \frac{t}{2R^2}(-av - w + aR\beta)\cos(a\theta),\ \gamma_{xy}^{b} = \frac{t}{2R^2}(au + R^2\beta' - aR\alpha)\sin(a\theta),$$

$$\gamma_{xz} = (w' + \alpha)\cos(a\theta),\ \gamma_{yz} = \frac{1}{R}(-aw - v + R\beta)\sin(a\theta). \quad \text{(B10)}$$

Comparing with the physical strains in the R-model [53], it can be shown that the strains are almost the same despite the difference in the bending strains ε_{yy}^{b} and γ_{xy}^{b}. The total potential for the cylinder is

$$\Pi_{cylinder} = \frac{1}{2}\sum_{\varphi=m,b,s}\int_{-L}^{L}\int_{0}^{2\pi}(\underline{\varepsilon}^{\varphi})^{T}\underline{\underline{D}}^{\varphi}\underline{\varepsilon}^{\varphi}J_0 d\theta dX - \int_{-L}^{L}\int_{0}^{2\pi} pu_r R d\theta dX \quad \text{(B11)}$$

After integrating with respect to θ, the total potential only depends on X and can be expressed as

$$\Pi_{cylinder} = \int_{-L}^{L}\mathcal{L}(\underline{q}, \underline{q}')dX = \int_{-L}^{L}[\frac{1}{2}(\underline{q}')^{T}\underline{\underline{K}}_{11}\underline{q}' + (\underline{q}')^{T}\underline{\underline{K}}_{10}\underline{q} + \frac{1}{2}\underline{q}^{T}\underline{\underline{K}}_{00}\underline{q} - \underline{F}^{T}\underline{q}]dX \quad \text{(B12)}$$

in which $\underline{q} = \{u, v, w, \alpha, \beta\}^T$, $\underline{q}' = d\underline{q}/dX$ and $\mathcal{L}(\underline{q}, \underline{q}')$ is self-defined and the $\underline{\underline{K}}$s and $\underline{F}$ are

$$\underline{\underline{K}}_{11} = \frac{\pi REt}{1-\upsilon^2}\cdot diag\{1, \frac{1-\upsilon}{2}, \frac{k(1-\upsilon)}{2}, \frac{t^2}{12}, \frac{(1-\upsilon)t^2}{24}\},$$

$$\underline{\underline{K}}_{10} = \frac{\pi Et}{12R(1-\upsilon^2)}\begin{bmatrix} 0 & 24R\upsilon & 12R\upsilon & 0 & 0 \\ 12R(\upsilon-1) & 0 & 0 & 0 & 0 \\ 0 & 0 & 0 & 6k(1-\upsilon)R^2 & 0 \\ 0 & -2\upsilon t^2 & -\upsilon t^2 & 0 & 2R\upsilon t^2 \\ (1-\upsilon)t^2 & 0 & 0 & R(1-\upsilon)t^2 & 0 \end{bmatrix},$$

$$\underline{\underline{K}}_{00} = \frac{\pi Et}{6R^3(1-\upsilon^2)}\begin{bmatrix} (12R^2+t^2)(1-\upsilon) & 0 \\ 0 & 3kR^2(1-\upsilon)+24R^2+2t^2 \\ 0 & 6kR^2(1-\upsilon)+12R^2+t^2 \\ Rt^2(\upsilon-1) & 0 \\ 0 & 3kR^3(\upsilon-1)-2Rt^2 \end{bmatrix}$$

$$\begin{bmatrix} 0 & Rt^2(\upsilon-1) & 0 \\ 6kR^2(1-\upsilon)+12R^2+t^2 & 0 & 3kR^3(\upsilon-1)-2Rt^2 \\ 12kR^2(1-\upsilon)+6R^2+t^2/2 & 0 & 6kR^3(\upsilon-1)-Rt^2 \\ 0 & R^2(1-\upsilon)(t^2+3kR^2) & 0 \\ 6kR^3(\upsilon-1)-Rt^2 & 0 & 3kR^4(1-\upsilon)+2R^2t^2 \end{bmatrix},$$

$$\underline{F} = \{0, 0, \pi p_0 R, 0, 0\}^T \ .$$

The Euler equation for (B12) is

$$\frac{\partial \mathcal{L}}{\partial \underline{q}} - \frac{d}{dX}\left(\frac{\partial \mathcal{L}}{\partial \underline{q}'}\right) = \underline{0} \tag{B13}$$

or

$$\underline{\underline{K}}_{11}\underline{q}'' + (\underline{\underline{K}}_{10} - \underline{\underline{K}}_{10}^T)\underline{q}' - \underline{\underline{K}}_{00}\underline{q} + \underline{F} = \underline{0} \tag{B14}$$

The second order equation can be cast into the following first order equation:

$$\begin{bmatrix} \underline{\underline{K}}_{11} & \underline{\underline{0}} \\ \underline{\underline{0}} & \underline{\underline{I}}_{5\times5} \end{bmatrix}\underline{V}' + \begin{bmatrix} \underline{\underline{K}}_{10} - \underline{\underline{K}}_{10}^T & -\underline{\underline{K}}_{00}^T \\ -\underline{\underline{I}}_{5\times5} & \underline{\underline{0}} \end{bmatrix}\underline{V} = \begin{Bmatrix} -\underline{F} \\ \underline{0} \end{Bmatrix} \tag{B15}$$

where $\underline{V}^T = \{(\underline{q}')^T, \underline{q}^T\}$. The general solution for $\underline{V}$ is

$$\underline{V} = \sum_{i=1}^{10} c_i \underline{\varphi_i} \exp(-\lambda_i X) + \underline{V_p} \tag{B16}$$

in which c_is are constants determined by the boundary conditions at $X = \pm L$, λ_is and $\underline{\varphi_i}$s are eigenvalues and eigenvectors of the system:

$$\begin{bmatrix} \underline{\underline{K}}_{10} - \underline{\underline{K}}_{10}^T & -\underline{\underline{K}}_{00}^T \\ -\underline{\underline{I}}_{5\times5} & \underline{\underline{0}} \end{bmatrix}\underline{\varphi_i} = \lambda_i \begin{bmatrix} \underline{\underline{K}}_{11} & \underline{\underline{0}} \\ \underline{\underline{0}} & \underline{\underline{I}}_{5\times5} \end{bmatrix}\underline{\varphi_i} \tag{B17}$$

Moreover, V_p is the particular solution which can be derived to be

$$\underline{V_p}^T = \{(\underline{q_o}')^T, \underline{q_o}^T\}$$

where

$$\underline{q_0} = \underline{\underline{K}}_{00}^{-1}\underline{F} = \frac{p_0 R^2(1-\upsilon^2)}{Et^3} \cdot \{0, -\frac{2}{9}[3R^2 + \frac{2t^2}{k(1-\upsilon)}], \frac{4}{9}[3R^2 + \frac{2t^2}{k(1-\upsilon)}], 0, 2R\}^T .$$

The particular solution is independent of the axial coordinate X. It represents the deformation of an infinitely long cylinder or cylinder with symmetric boundary conditions at its two ends. It should be noted that c_is, λ_is and $\underline{\varphi_i}$s are complex in general. The characteristic equation for (B17) is obtained from the following determinant:

$$\det\left(\begin{bmatrix} \underline{\underline{K_{10}}} - \underline{\underline{K_{10}^T}} & -\underline{\underline{K_{00}^T}} \\ -\underline{\underline{I}}_{5\times5} & \underline{\underline{0}} \end{bmatrix} - \lambda \begin{bmatrix} \underline{\underline{K_{11}}} & \underline{\underline{0}} \\ \underline{\underline{0}} & \underline{\underline{I}}_{5\times5} \end{bmatrix}\right) = 0 \tag{B18}$$

The eigenvalues are roots of the characteristic equation. Taking the parameters (k = 5/6, υ = 1/3), the characteristic equation is

$$\begin{aligned} &90t^4\lambda^{10} + (-2103t^4 - 104t^6 - 900t^2)\lambda^8 + (884t^6 + 17640t^2 + 15624t^4)\lambda^6 \\ &+(-9600 - 49563t^4 - 3104t^6 - 81860t^2)\lambda^4 \\ &+(2880t^6 + 75480t^4 + 136800t^2)\lambda^2 - 129600t^2 - 62640t^4 = 0 \end{aligned}$$

Through the Puiseux expansion, the roots are

$$\begin{aligned} &\lambda_1 = 1.35540301(1+i)\sqrt{t} + 1.31418478(1-i)t^{3/2} + 0(t^{5/2}), \\ &\lambda_2 = -\lambda_1, \quad \lambda_3 = \overline{\lambda}_1, \quad \lambda_4 = -\lambda_3, \\ &\lambda_5 = 1.27788621(1+i)t^{-1/2} + 1.81288964(1-i)t^{1/2} + 0(t^{3/2}), \\ &\lambda_6 = -\lambda_5, \quad \lambda_7 = \overline{\lambda}_5, \quad \lambda_8 = -\lambda_7, \\ &\lambda_9 = 3.16227766t^{-1} + 0.76421710t + 0(t^3), \\ &\lambda_{10} = -\lambda_9 \end{aligned} \tag{B19}$$

where $i = \sqrt{-1}$ and the overbar refers to the complex conjugate of the quantity below. Recalling that the general solutions are linear combinations of $\exp(-\lambda_i X)$, the eigenvalues $\lambda_1 \sim \lambda_4$ are associated with the smooth part of the solution. In addition, the leading terms in $\lambda_5 \sim \lambda_8$ and $\lambda_9 \sim \lambda_{10}$ indicate that they are associated with the boundary layers of $\sqrt{t}$-scale and t-scale, respectively [53]. Comparing the eigenvalues in (B19) with that of the R-model in [53], it can be noted that the leading terms of λ_1 through λ_8 are the same. This echoes the fact that the present formulation and the R-model deviates only slightly from each other in considering the bending strains.

Interested readers may contact the senior author for the Matlab code leading to the reference solution.

Appendix C: Reference Solutions for the Hyperbolic Shell Problems

In this appendix, procedures for obtaining the reference solutions for the hyperbolic shell problems is presented for the C^0 shell formulation introduced in Section 3. The mid-surface of the hyperbolic shell is given by the following equation [7, 55]:

$$X^2 + Z^2 = 1 + Y^2 \tag{C1}$$

The two ends are either both clamped or free. The coordinate parameters Y and θ are chosen to describe the shell geometry, see Figure 25. The shell mid-surface is

$$\underline{X}^o = \{A\cos(\theta), Y, A\sin(\theta)\}^T \tag{C2}$$

where $A = \sqrt{1+Y^2}$. Thus, the tangential vectors along the increasing directions of Y and θ are

$$\frac{\partial \underline{X}^o}{\partial Y} = \left\{\frac{Y}{A}\cos(\theta), 1, \frac{Y}{A}\sin(\theta)\right\}^T, \quad \frac{\partial \underline{X}^o}{\partial \theta} = \{-A\sin(\theta), 0, A\cos(\theta)\}^T. \tag{C3}$$

which are parallel to the following unit vectors

$$\underline{e}_x = \left\{\frac{Y}{B}\cos(\theta), \frac{A}{B}, \frac{Y}{B}\sin(\theta)\right\}^T, \quad \underline{e}_\theta = \{-\sin(\theta), 0, \cos(\theta)\}^T \tag{C4}$$

where $B = \sqrt{1+2Y^2}$. The surface unit normal and $\underline{X}^n$ are

$$\underline{e}_n = \underline{e}_x \times \underline{e}_\theta = \left\{\frac{A}{B}\cos(\theta), -\frac{Y}{B}, \frac{A}{B}\sin(\theta)\right\}^T, \quad \underline{X}^n = \frac{t}{2}\underline{e}_n. \tag{C5}$$

The cylindrical coordinate is defined by introducing another two unit vectors to $\underline{e}_\theta$

$$\underline{e}_Y = \{0,1,0\}^T \quad \text{and} \quad \underline{e}_r = \{\cos(\theta), 0, \sin(\theta)\}^T \tag{C6}$$

From the applied loading $p(\theta) = p_0\cos(a\theta)$ and the supporting conditions, the mid-surface displacements and rotations can be expressed as [55]:

$$\begin{Bmatrix} u_Y \\ u_\theta \\ u_r \end{Bmatrix} = \begin{Bmatrix} u(Y)\cos(a\theta) \\ v(Y)\sin(a\theta) \\ w(Y)\cos(a\theta) \end{Bmatrix}, \quad \begin{Bmatrix} \phi_x \\ \phi_\theta \end{Bmatrix} = \begin{Bmatrix} \alpha(Y)\cos(a\theta) \\ \beta(Y)\sin(a\theta) \end{Bmatrix} \tag{C7}$$

where (u_Y, u_θ, u_r) are mid-surface displacement components in the cylindrical coordinate; ϕ_x and ϕ_θ are rotations defined with respect to the tangential base vectors $\underline{e}_x$ and $\underline{e}_\theta$. Thus

$$\underline{U}^o = u_Y\underline{e}_Y + u_\theta\underline{e}_\theta + u_r\underline{e}_r \quad \text{and} \quad \underline{U}^n = \phi_x\frac{t}{2}\underline{e}_x + \phi_\theta\frac{t}{2}\underline{e}_\theta \tag{C8}$$

By taking $\xi = Y$ and $\eta = \theta$ in (11a-e), the covariant strain components with respect to (Y,θ,ζ) are

$$\varepsilon^0_{YY} = (u' + \frac{Y}{A}w')\cos(a\theta), \quad \varepsilon^0_{\theta\theta} = A(av + w)\cos(a\theta), \quad \gamma^0_{Y\theta} = \frac{1}{A}(-aAu - Yv - aYw + A^2v')\sin(a\theta),$$

$$\varepsilon^1_{YY}=\frac{t}{2AB^3}\left[-Yw'-Au'+B^4\alpha'\right]\cos(a\theta)\,,\ \ \varepsilon^1_{\theta\theta}=\frac{tA}{2B}(av+w+Y\alpha+aB\beta)\cos(a\theta)\,,$$

$$\gamma^1_{Y\theta}=\frac{t}{2AB^3}(aAu+Yv+aYw-aB^4\alpha-B^3Y\beta+A^2B^2v'+A^2B^3\beta')\sin(a\theta)\,,$$

$$\gamma_{Y\zeta}=\frac{t}{2AB}(B^2\alpha-AYu'+A^2w')\cos(a\theta)\,,\ \ \gamma_{\theta\zeta}=\frac{t}{2B}(aYu-Av-aAw+AB\beta)\sin(a\theta) \qquad \text{(C9)}$$

Let (x, y, z) be the local Cartesian coordinates and their unit base vectors are $(\underline{e}_x, \underline{e}_\theta, \underline{e}_n)$, then

$$x_{,Y}=\underline{e}_x^T\frac{\partial \underline{X}}{\partial Y}=\frac{B}{A}-\frac{t}{2AB^2}\zeta\quad,\quad y_{,\theta}=\underline{e}_\theta^T\frac{\partial \underline{X}}{\partial \theta}=A+\frac{tA}{2B}\zeta$$

$$z_{,\zeta}=\frac{t}{2}\quad\text{and}\quad J_0=(x_{,Y}\,y_{,\theta}\,z_{,\zeta})\Big|_{\zeta=0}=B\frac{t}{2} \qquad \text{(C10)}$$

Since the coordinates are orthogonal,

$$\begin{aligned}&Y_{,x}=(x_{,Y})^{-1}=(\frac{B}{A}-\frac{t}{2AB^2}\zeta)^{-1}=\frac{A}{B}+\frac{tA}{2B^4}\zeta+0(\zeta^2)\,,\\&\theta_{,y}=(y_{,\theta})^{-1}=(A+\frac{tA}{2B}\zeta)^{-1}=\frac{1}{A}-\frac{t}{2AB}\zeta+0(\zeta^2)\,,\ \ \zeta_{,z}=(z_{,\zeta})^{-1}=\frac{2}{t}\end{aligned} \qquad \text{(C11)}$$

The transformation matrixes are

$$\underline{\underline{T}}^0_\varepsilon=diag.\{\frac{A^2}{B^2},\frac{1}{A^2},\frac{1}{B}\},\ \ \underline{\underline{T}}^1_\varepsilon=\frac{t}{B}diag.\{\frac{A^2}{B^4},\frac{-1}{A^2},-\frac{Y^2}{B^3}\},\ \ \underline{\underline{T}}^0_\gamma=\frac{2}{t}diag.\{\frac{A}{B},\frac{1}{A}\}. \qquad \text{(C12)}$$

Through (12a,b), the physical strains are

$$\varepsilon^m_{xx}=\frac{A}{B^2}(Au'+Yw')\cos(a\theta)\,,\ \ \varepsilon^m_{yy}=\frac{1}{A}(av+w)\cos(a\theta)\,,\quad \gamma^m_{xy}=\frac{1}{AB}(-aAu-Yv-aYw+A^2v')\sin(a\theta)\,,$$

$$\varepsilon^b_{xx}=\frac{tA}{2B^5}(Au'+Yw'+B^4\alpha')\cos(a\theta)\,,\ \ \varepsilon^b_{yy}=\frac{t}{2AB}(-av-w+Y\alpha+aB\beta)\cos(a\theta)\,,$$

$$\gamma^b_{xy}=\frac{t}{2AB^4}(aAB^2u+B^2Yv+aB^2Yw-aB^4\alpha-B^3Y\beta+A^2v'+A^2B^3\beta')\sin(a\theta)\ \,,$$

$$\gamma_{xz}=\frac{1}{B^2}(B^2\alpha-AYu'+A^2w')\cos(a\theta)\,,\ \ \gamma_{yz}=\frac{1}{AB}(aYu-Av-aAw+AB\beta)\sin(a\theta)\,. \qquad \text{(C13)}$$

The total potential for the half hyperboloid ($-1 \le Y \le 0$) is

$$\Pi_{hyperboloid}=\frac{1}{2}\sum_{\varphi=m,b,s}\int_{-1}^{0}\int_{0}^{2\pi}(\underline{\varepsilon}^\varphi)^T\underline{\underline{D}}^\varphi\underline{\varepsilon}^\varphi J_0 d\theta dY-\int_{-1}^{0}\int_{0}^{2\pi}p\underline{e}_n^T\underline{U}^o B d\theta dY\ . \qquad \text{(C14)}$$

After integrating with respect to θ, the total potential only depends on Y. The stationary conditions of the potential lead to a system of ODE's which do not appear to be solvable analytically. However, highly-converged reference solution can be obtained efficiently by 1D finite element discretization. Interested readers may contact the senior author for the Matlab code leading to the reference solution.

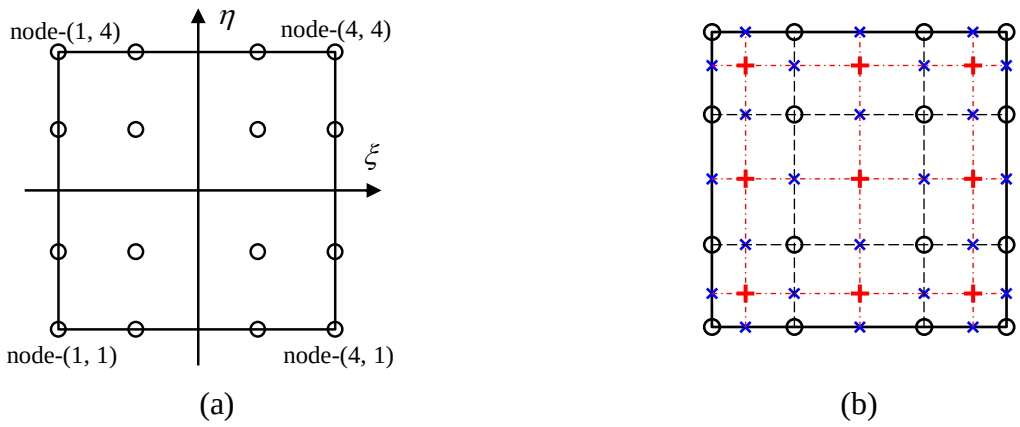

Figure 1. The third order Labotto element: (a) Designations for Lobatto nodes ○. (b) Reduced order Gaussian quadrature points + and auxiliary nodes ×.

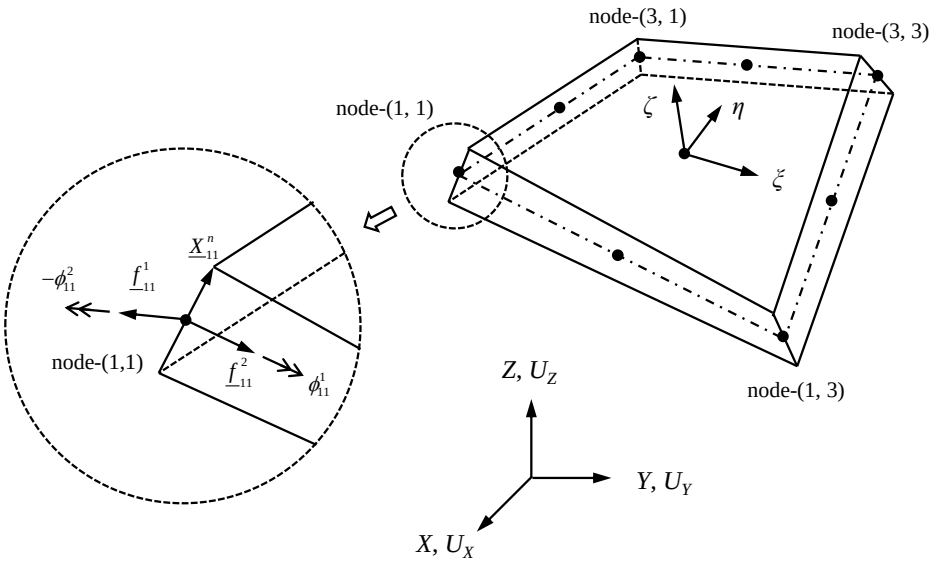

Figure 2. The quadratic C^0 shell element.

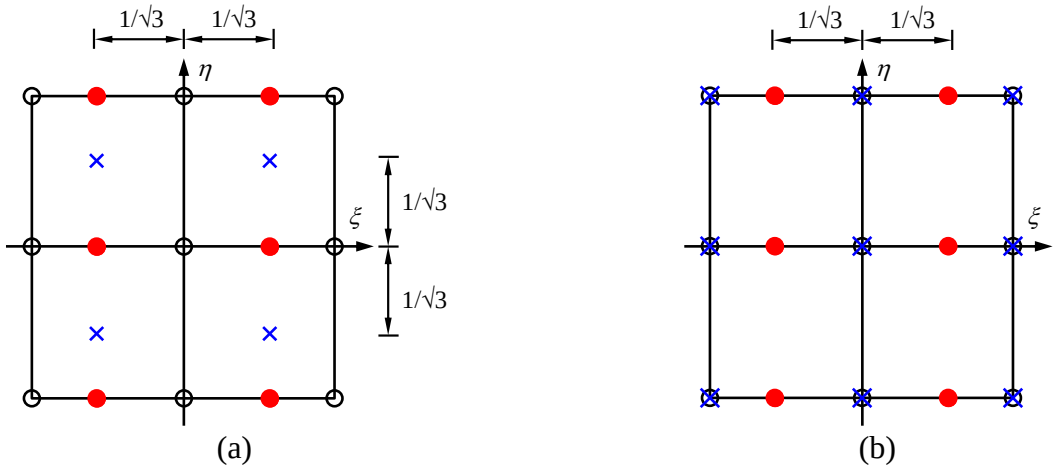

Figure 3. The sampling points of (a) an improved version of MITC9 and (b) the first ANS scheme. ○ denotes node, ● denotes the sampling point for $\varepsilon^0_{\xi\xi}$ and $\gamma_{\zeta\xi}$, × denotes the sampling point for $\gamma^0_{\xi\eta}$. ±1/√3 are the second order Gaussian quadrature points.

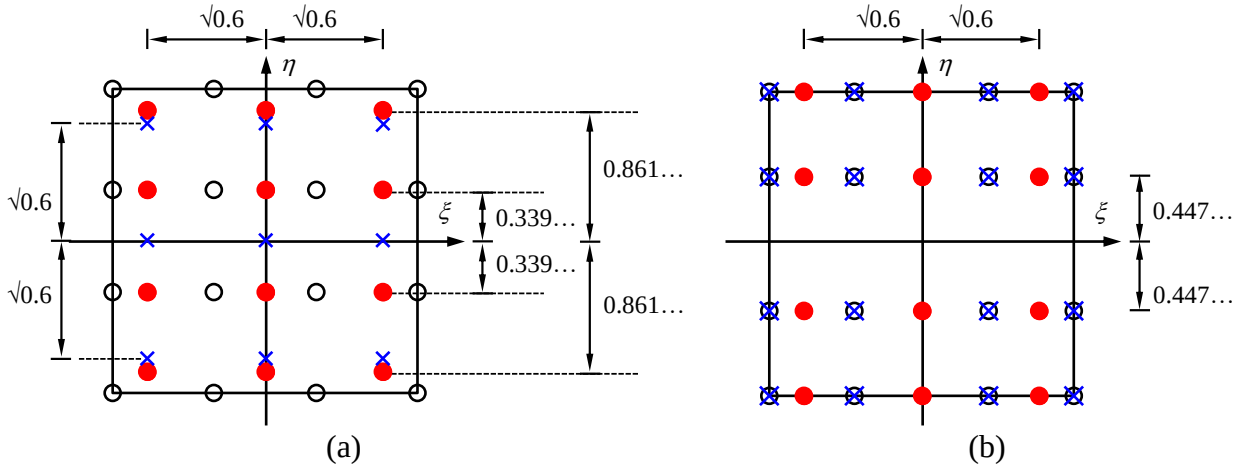

Figure 4. The sampling points of (a) MITC16 and (b) the first ANS scheme. ○ denotes node, ● denotes the sampling point for $\varepsilon^0_{\xi\xi}$ and $\gamma_{\zeta\xi}$, × denotes the sampling point for $\varepsilon^0_{\xi\eta}$. (0, ±√0.6) and (±0.339…, ±0.861…) are the third and fourth order Gaussian quadrature points, respectively.

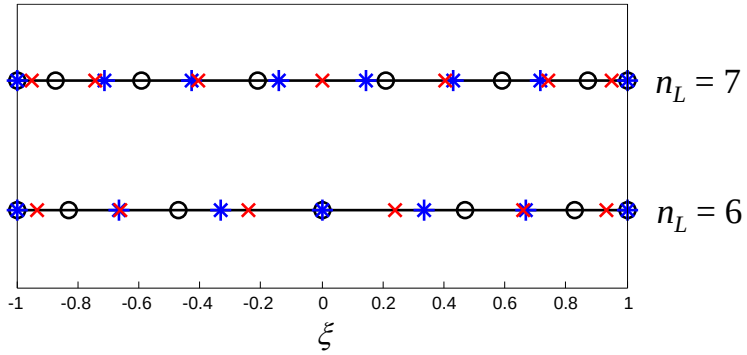

Figure 5. The Lobatto nodes ○, equispaced nodes * and reduced Gaussian points × for n_L = 6 and 7.

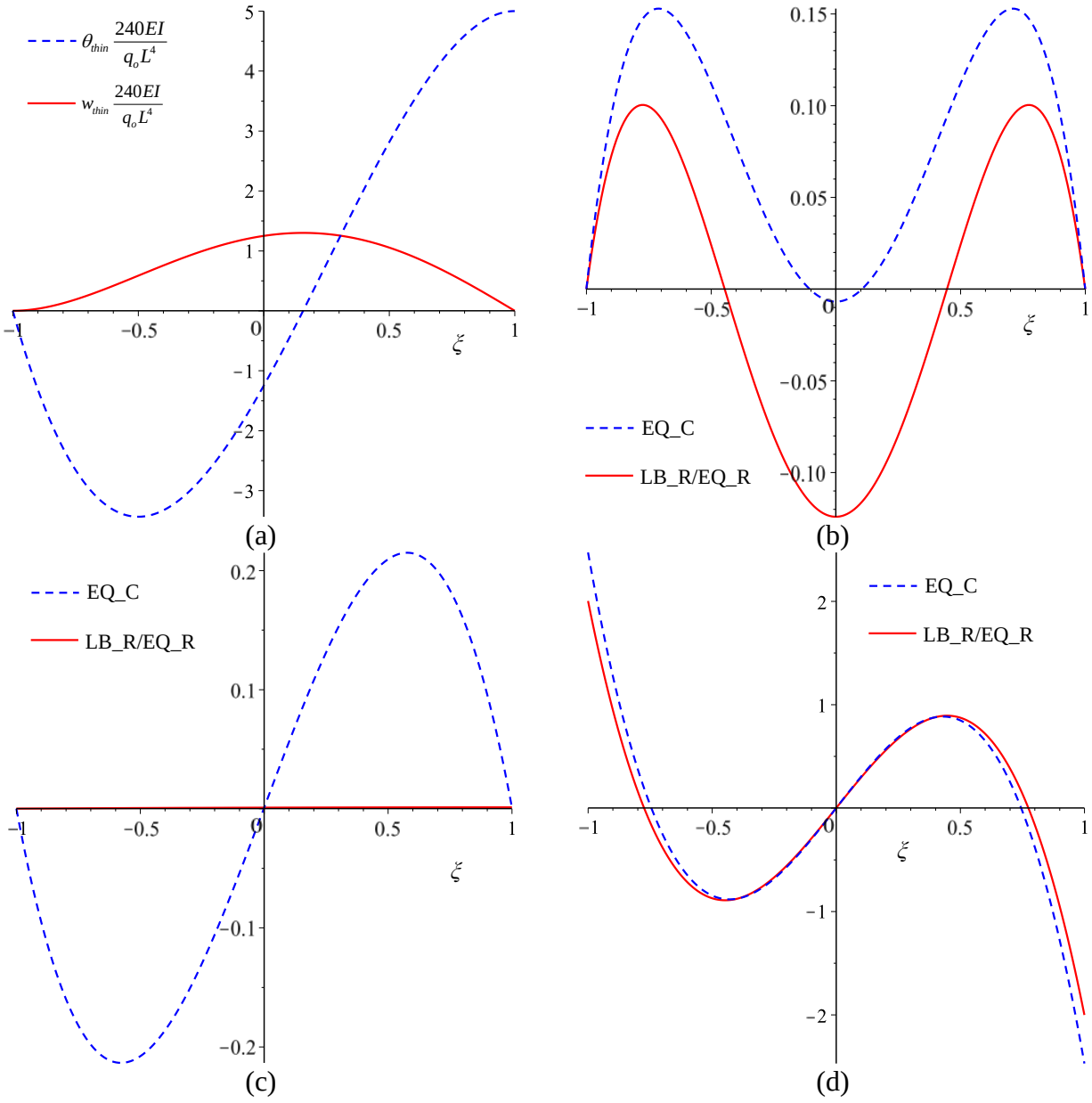

Figure 6. (a) Thin beam solution $w_{thin}c$ and $\theta_{thin}c$, (b) the deflection error $(w^h - w_{thin})c$, (c) the rotation error $(\theta^h - \theta_{thin})c$ and (d) the transverse shear $\gamma^h c$. The scaling factor c equals $240EI/(q_oL^4)$.

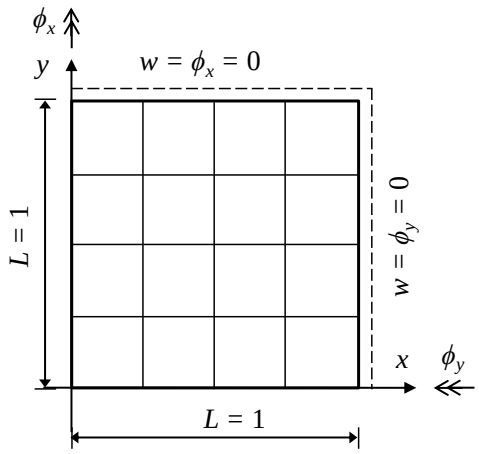

Figure 7. A quarter of the hard-simply supported square plate meshed into 4×4 regular elements.

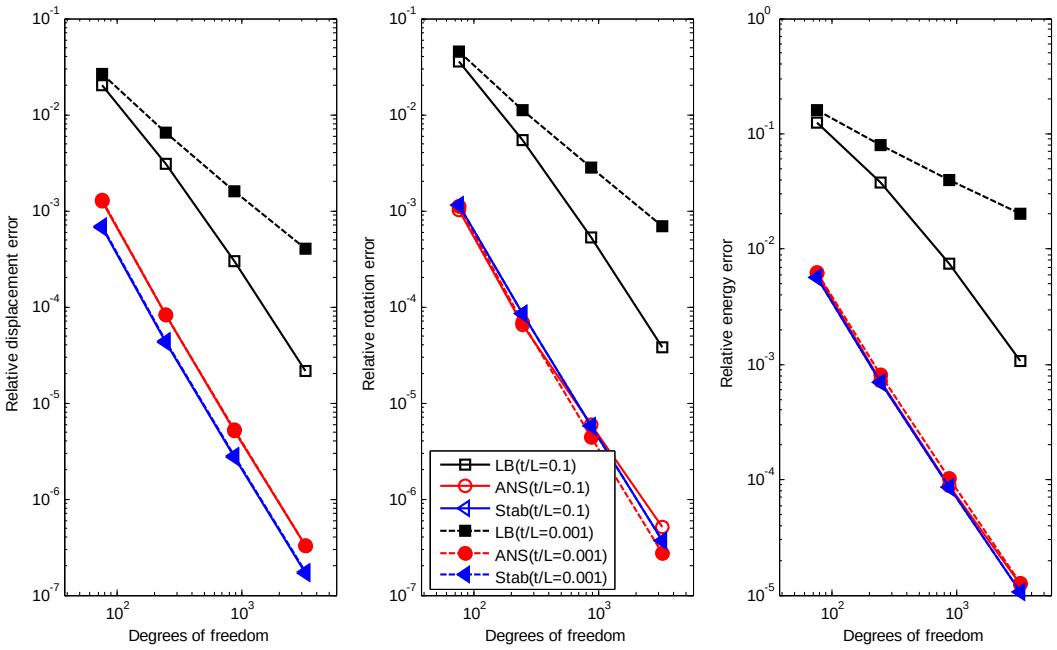

(a) $n_L = 2$

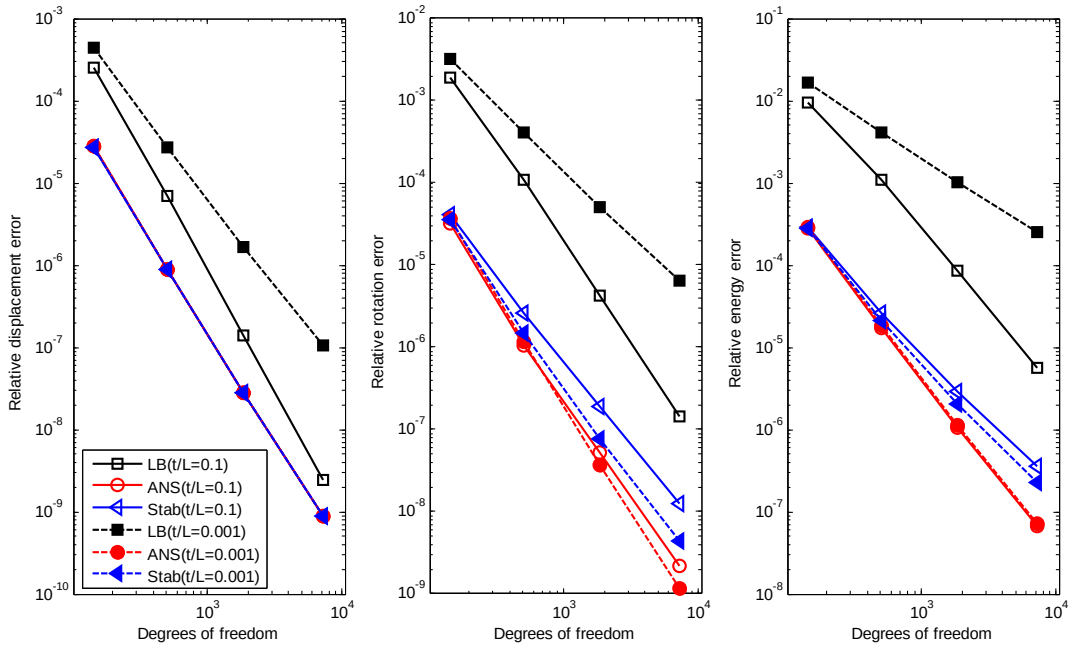

(b) $n_L = 3$

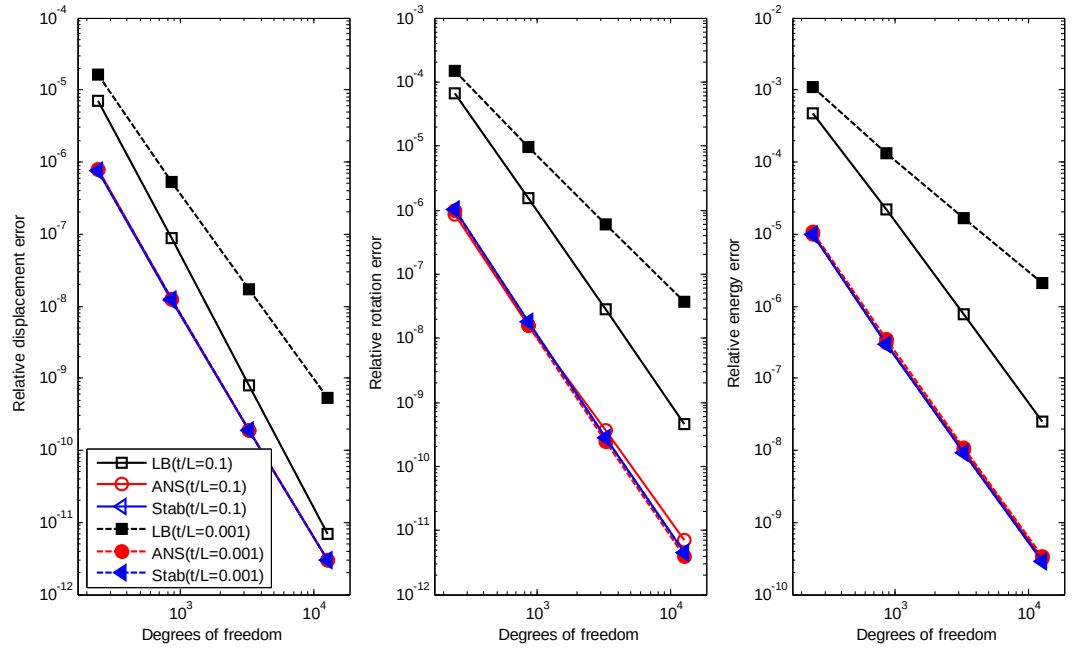

(c) $n_L = 4$

Figure 8. Errors for the square plate problem in Figure 7.

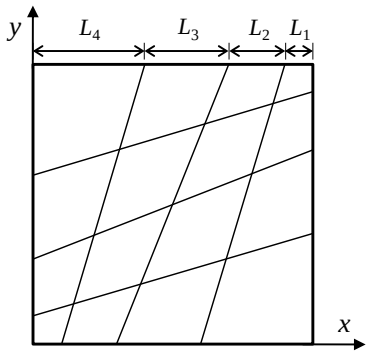

Figure 9. The 4×4 distorted mesh for the hard-simply supported square plate problem.

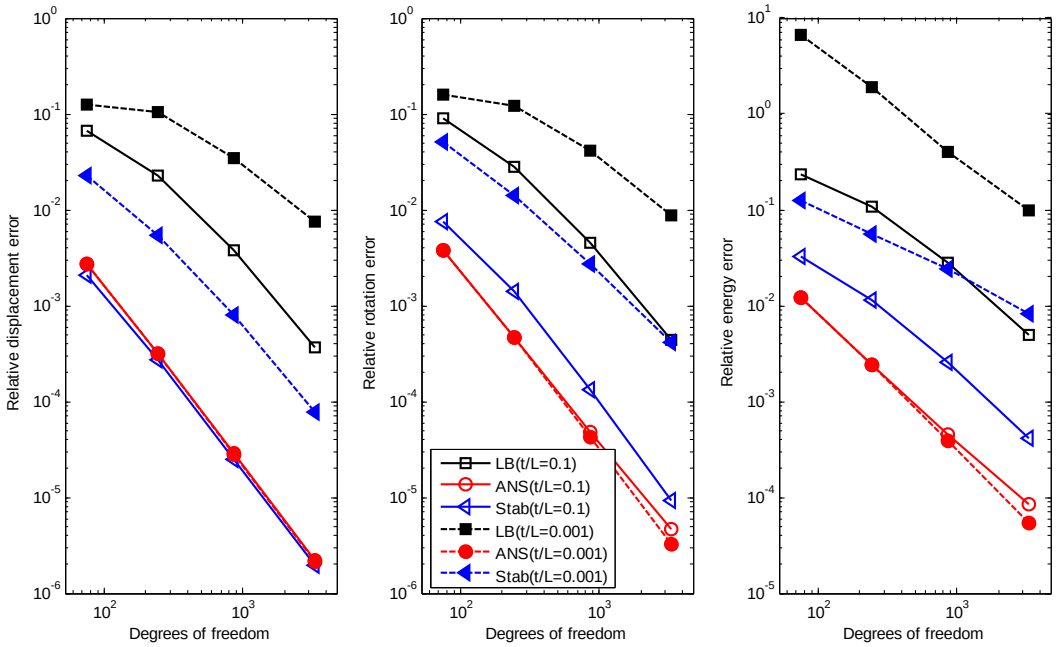

(a) $n_L = 2$

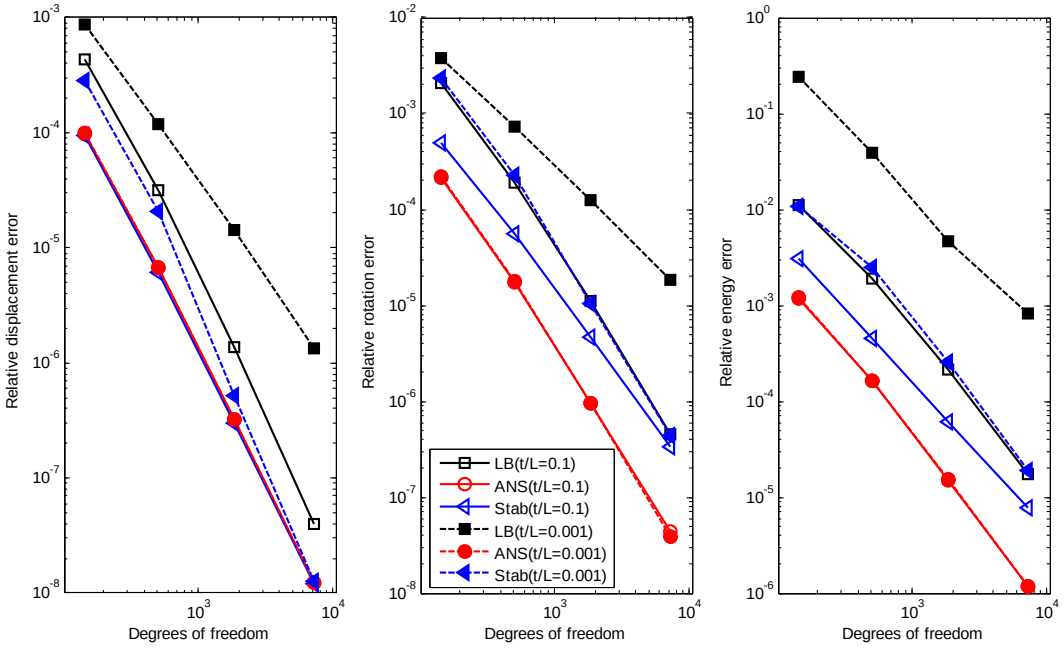

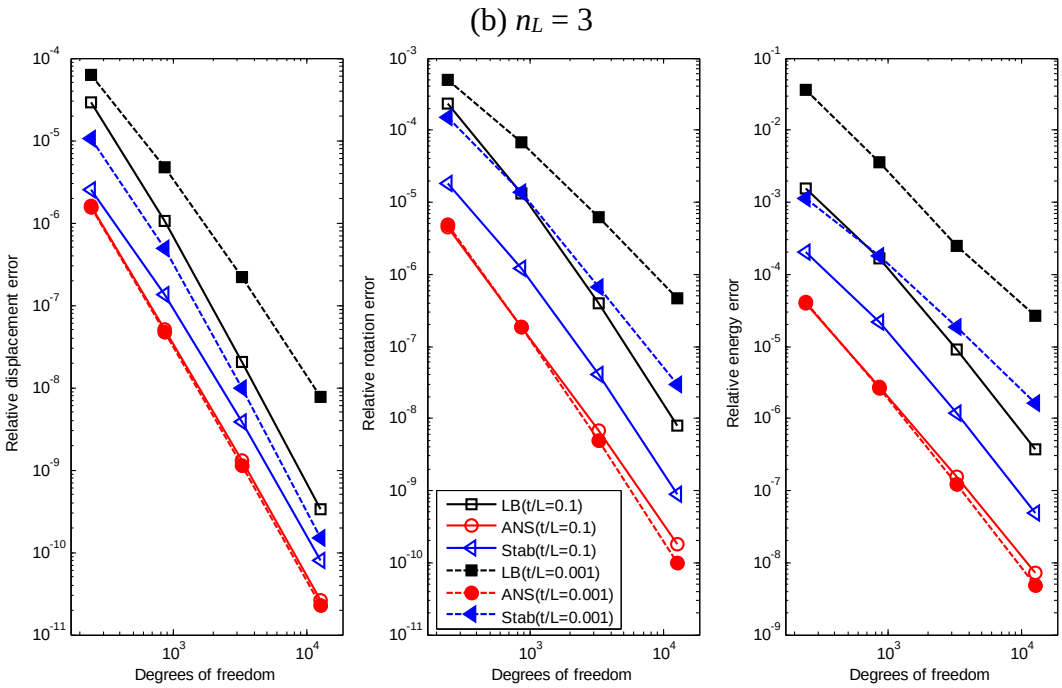

Figure 10. Errors for the square plate problem in Figure 9.

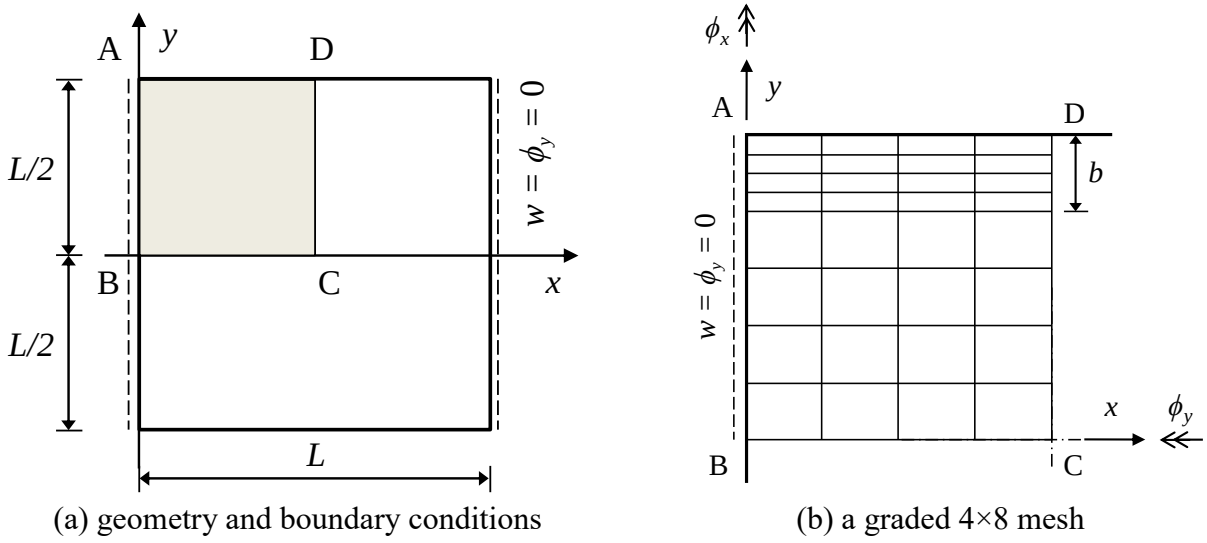

Figure 11. Square plate with boundary layer effect, L = 1, and the 4×8 graded mesh.

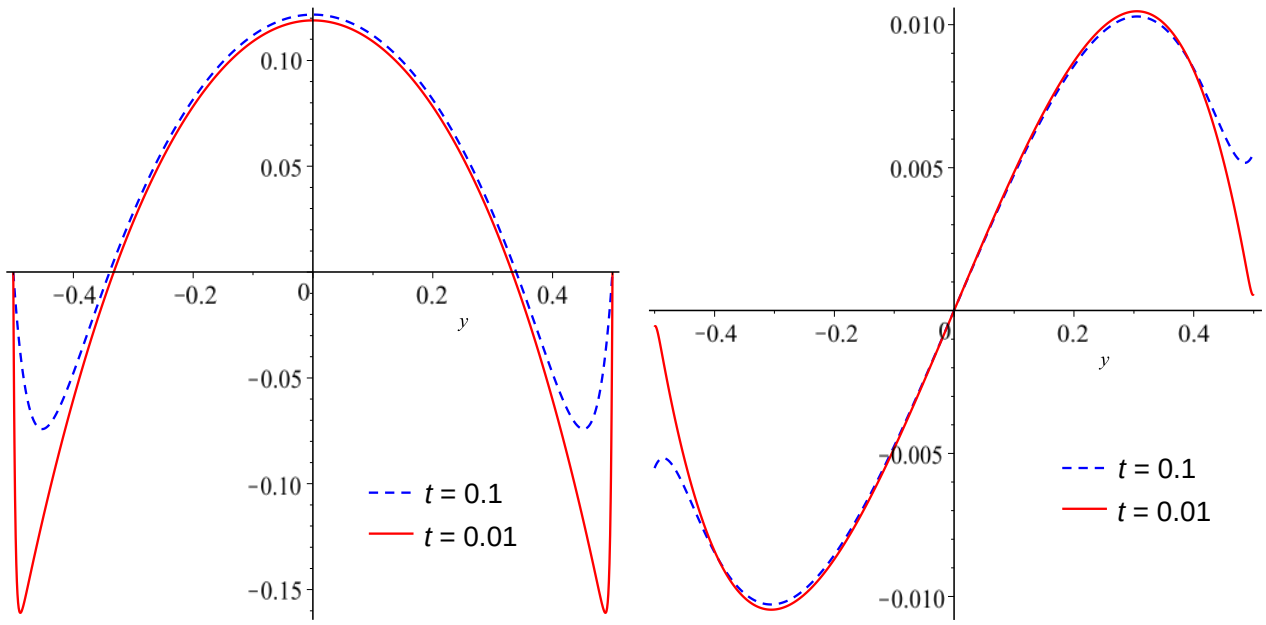

(a) shear force Q_x/q_0 (b) twisting moment Mxy/q_0

Figure 12. The analytical shear force Q_x and twisting moment M_{xy} along $x = 0$ when the edges at $y = \pm L/2$ of the square plate in Figure 11 are clamped.

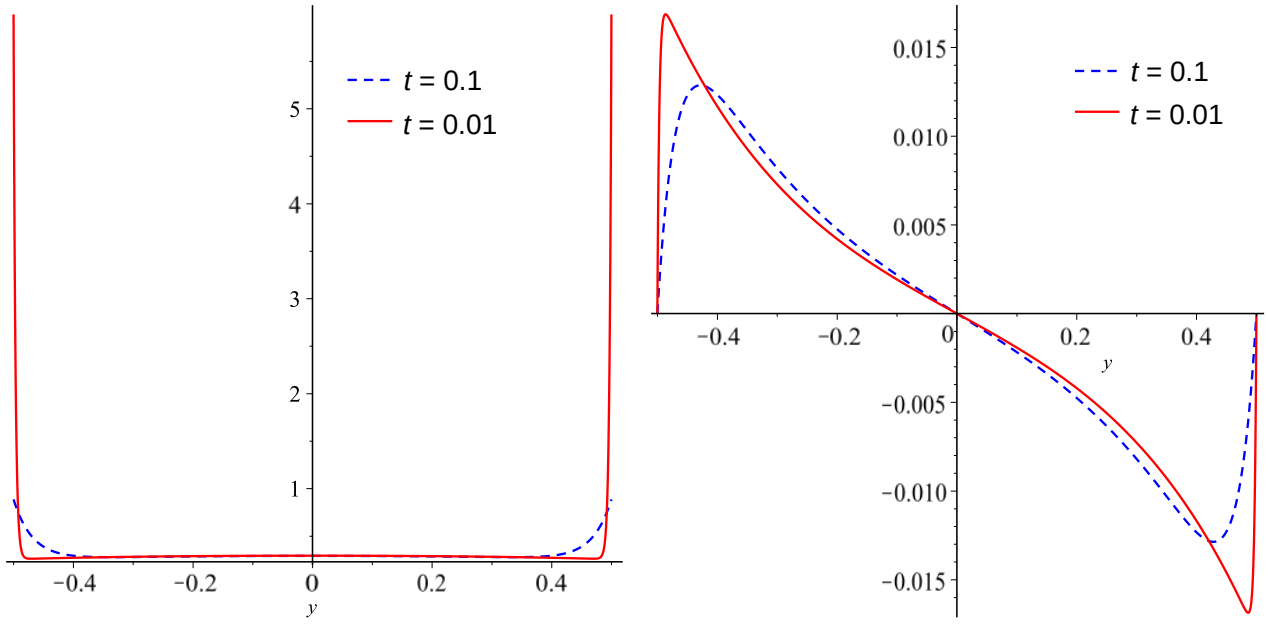

(a) shear force Q_x/q_0 (b) twisting moment Mxy/q_0

Figure 13. The analytical shear force Q_x and twisting moment M_{xy} along $x = 0$ when the edges at $y = \pm L/2$ of the square plate in Figure 11 are free.

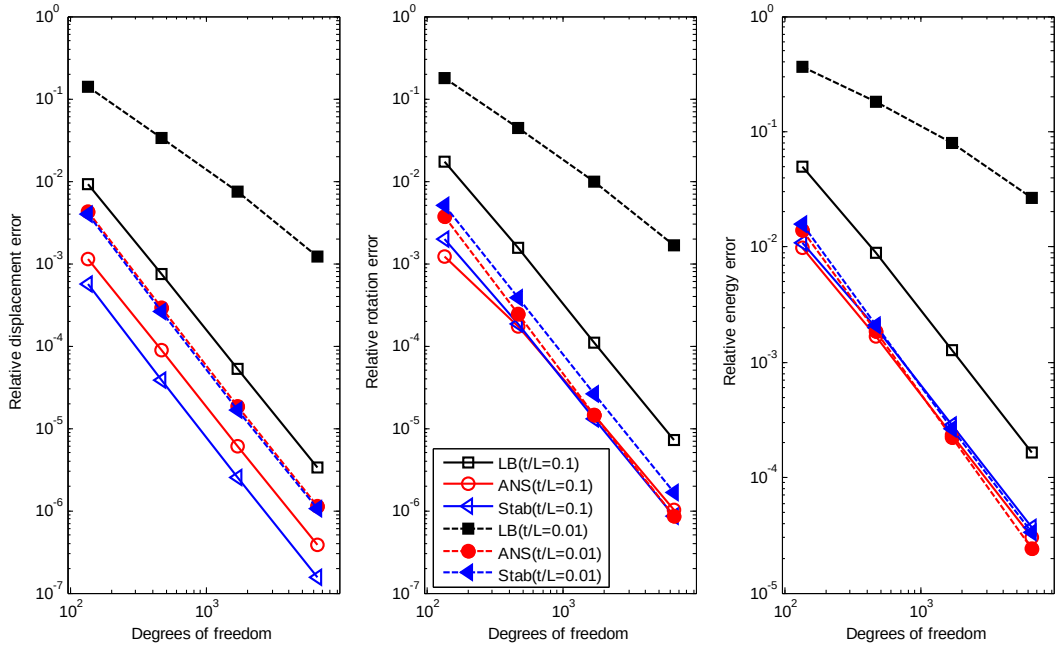
Relative displacement error
Relative rotation error
Relative energy error
Degrees of freedom
LB(t/L=0.1)
ANS(t/L=0.1)
Stab(t/L=0.1)
LB(t/L=0.01)
ANS(t/L=0.01)
Stab(t/L=0.01)

(a) $n_L = 2$

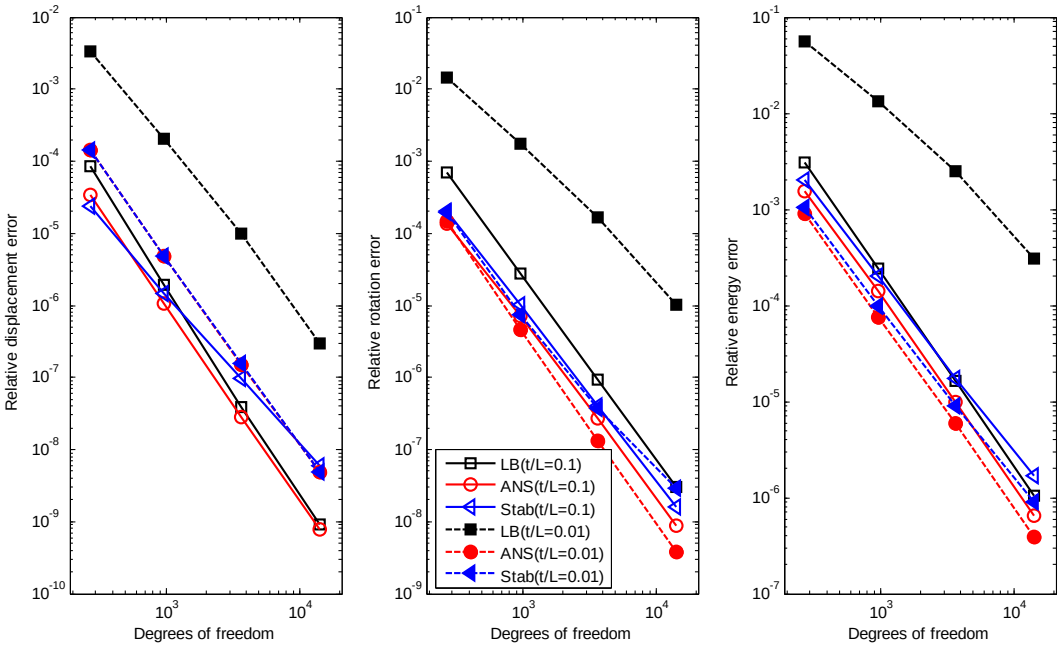
Relative displacement error
Relative rotation error
Relative energy error
Degrees of freedom
LB(t/L=0.1)
ANS(t/L=0.1)
Stab(t/L=0.1)
LB(t/L=0.01)
ANS(t/L=0.01)
Stab(t/L=0.01)

(b) $n_L = 3$

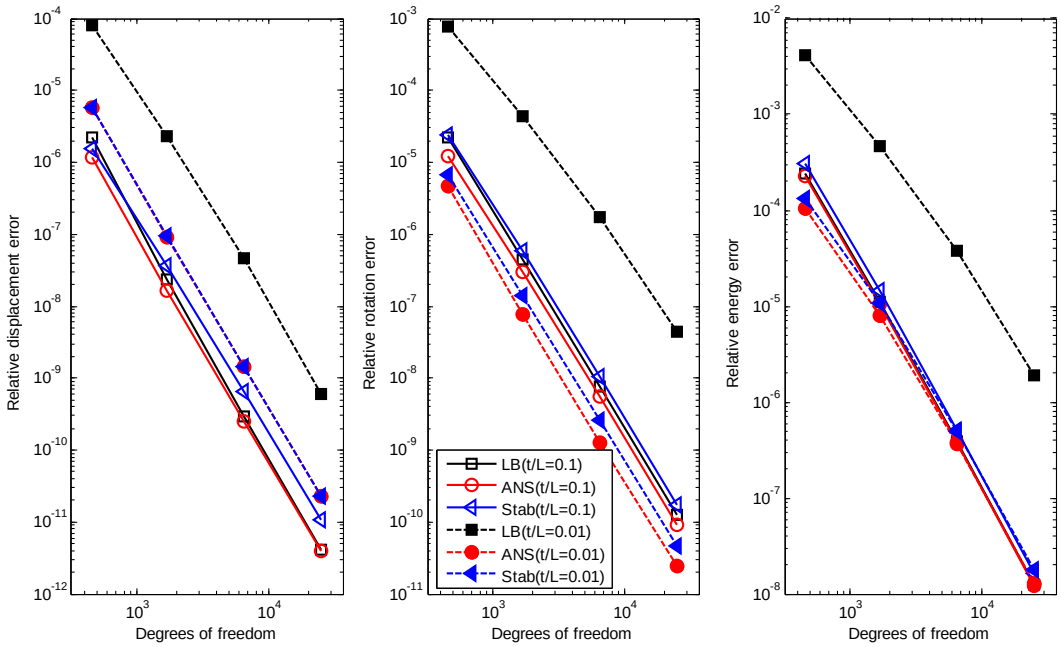

(c) $n_L = 4$

Figure 14. Errors for the square plate problem with boundary layer effect and clamped edges at $y = \pm L/2$, see Figure 11.

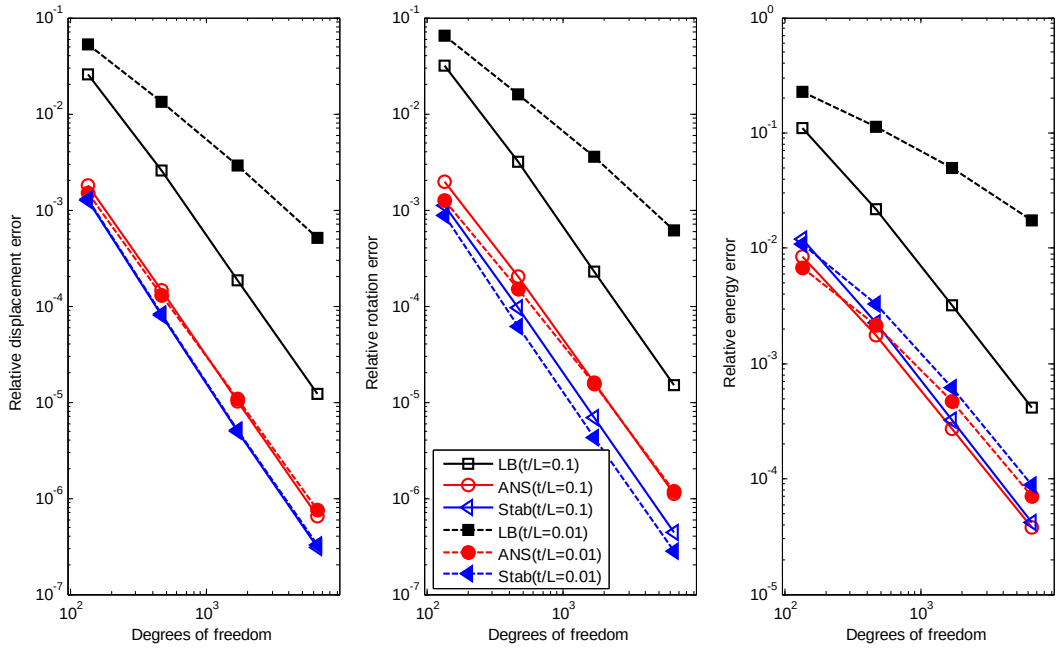

(a) $n_L = 2$

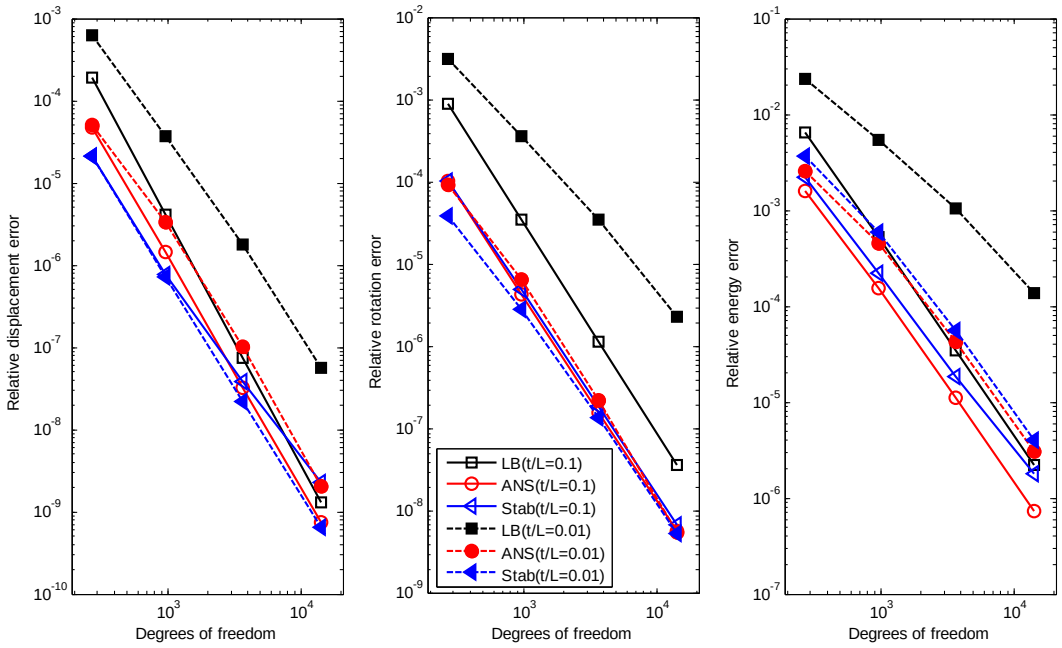

(b) $n_L = 3$

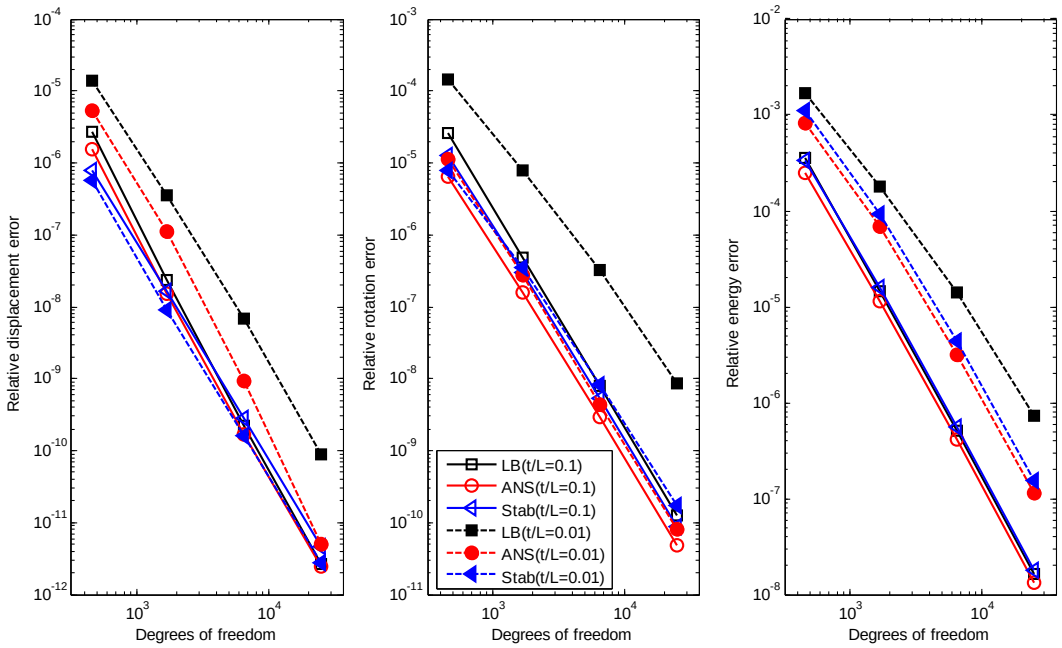

(c) $n_L = 4$

Figure 15. Errors for the square plate problem with boundary layer effect and free edges at $y = \pm L/2$, see Figure 11.

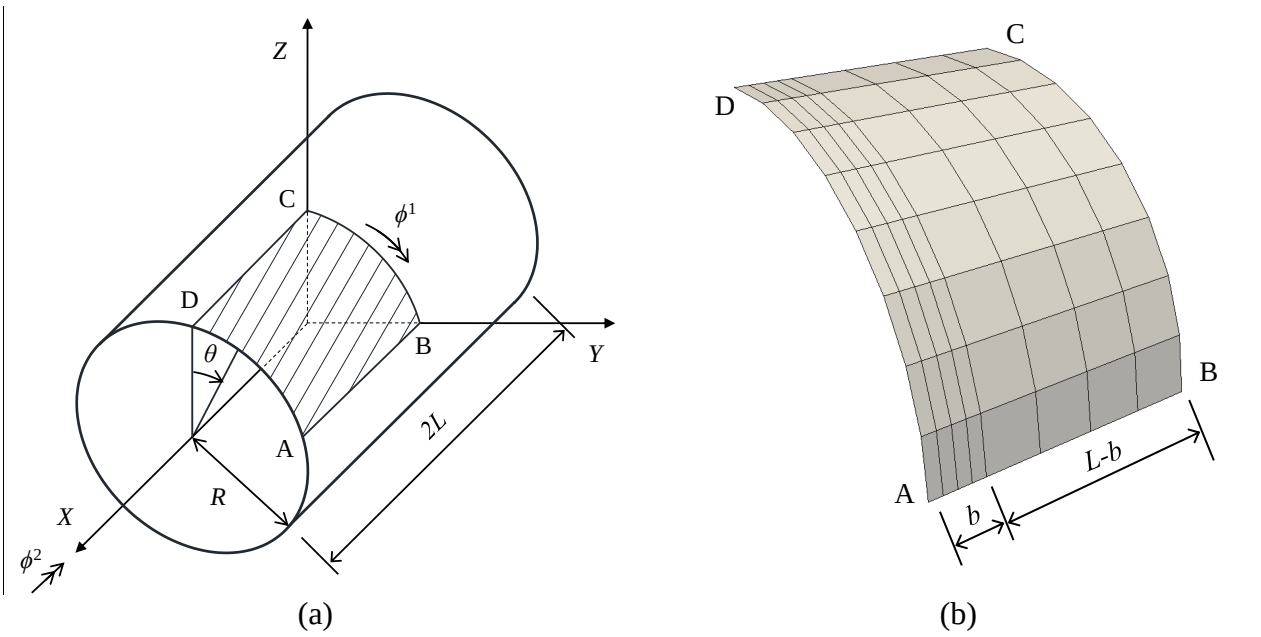

Figure 16. The cylindrical shell problem and the 8×8 graded mesh. R = L = 1.

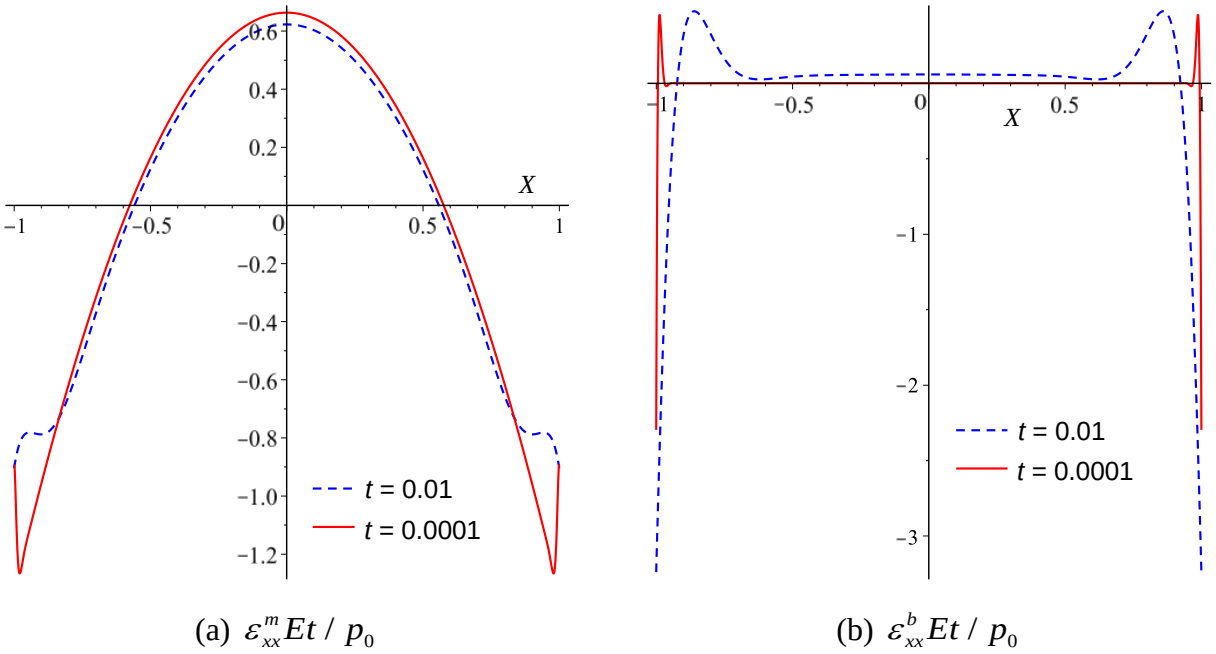

Figure 17. The analytical axial membrane and bending strains along θ = 0 when the two ends of the cylindrical shell in Figure 16 are clamped.

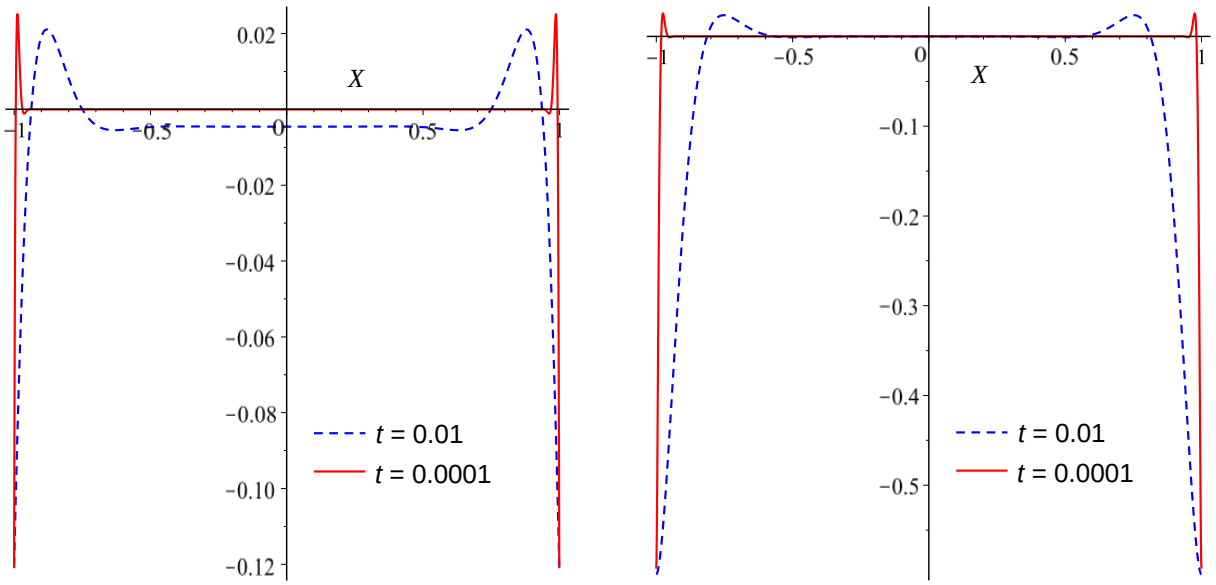

(a) $\varepsilon_{xx}^{m} Et^2 / p_0$ (b) $\varepsilon_{xx}^{b} Et^2 / p_0$

Figure 18. The analytical axial membrane and bending strains along $\theta = 0$ when the two ends of the cylindrical shell in Figure 16 are free.

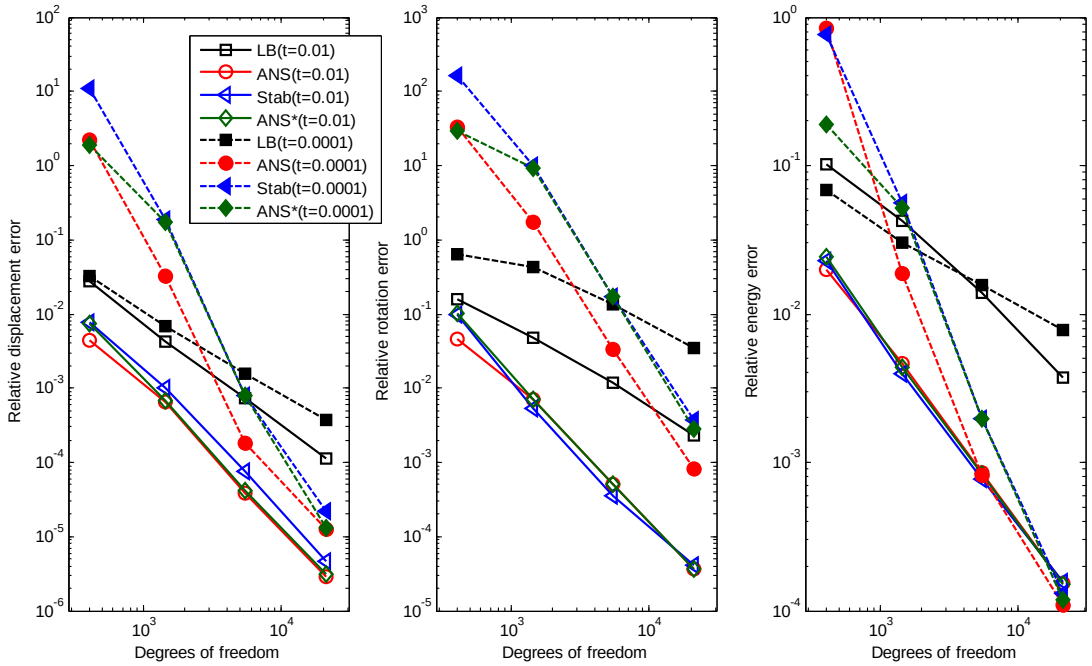

(a) $n_L = 2$

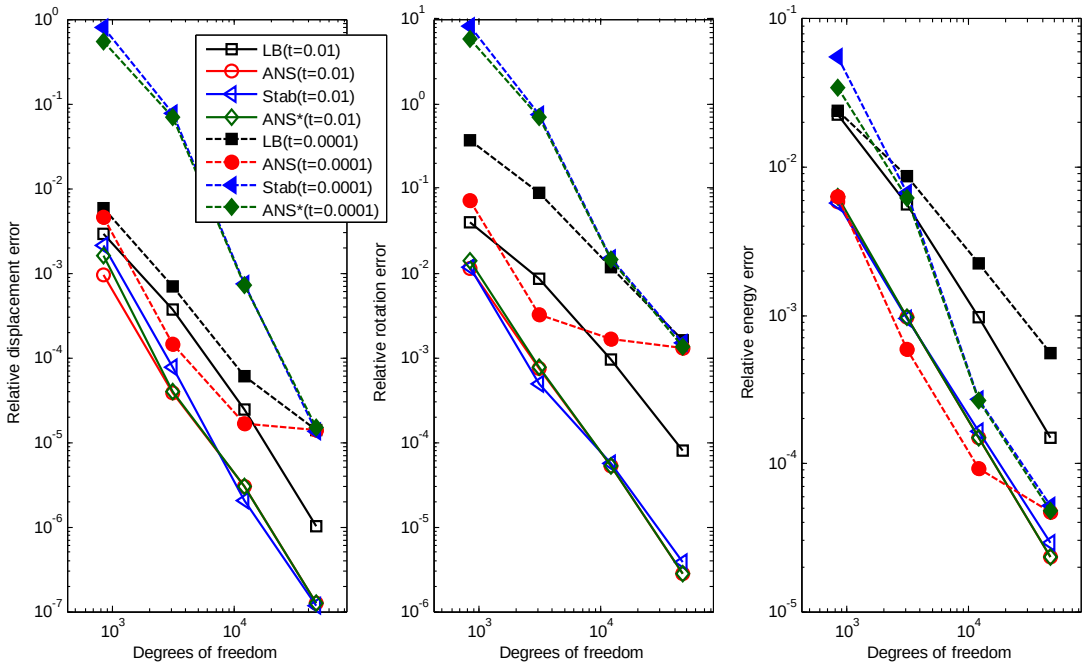

(b) $n_L = 3$

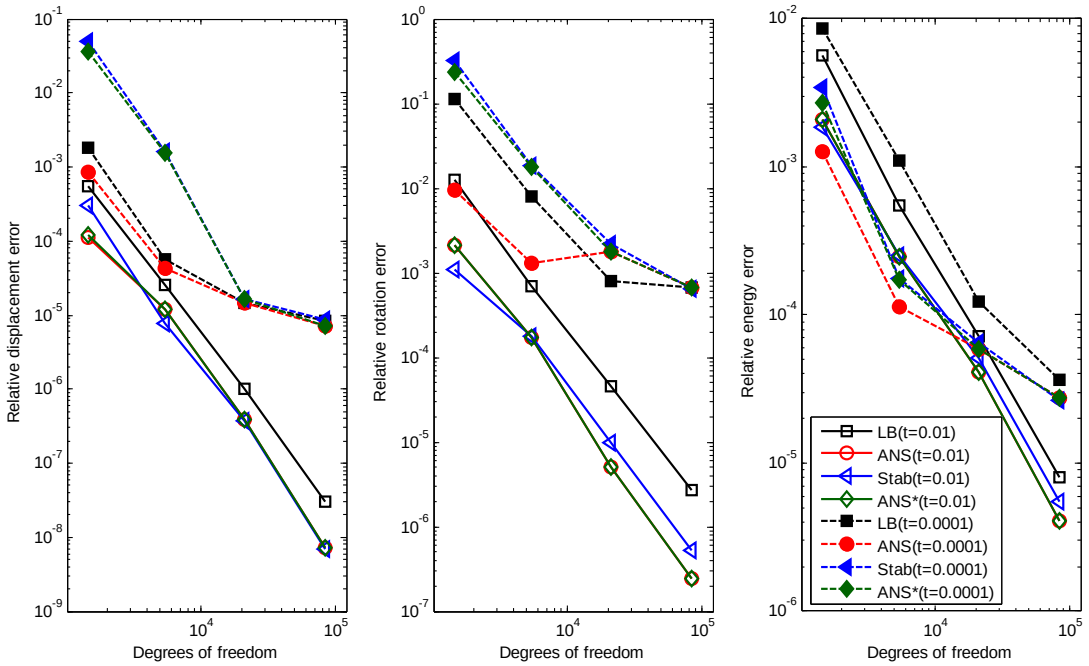

(c) $n_L = 4$

Figure 19. Errors for the cylindrical shell problem in Figure 16 with clamped ends.

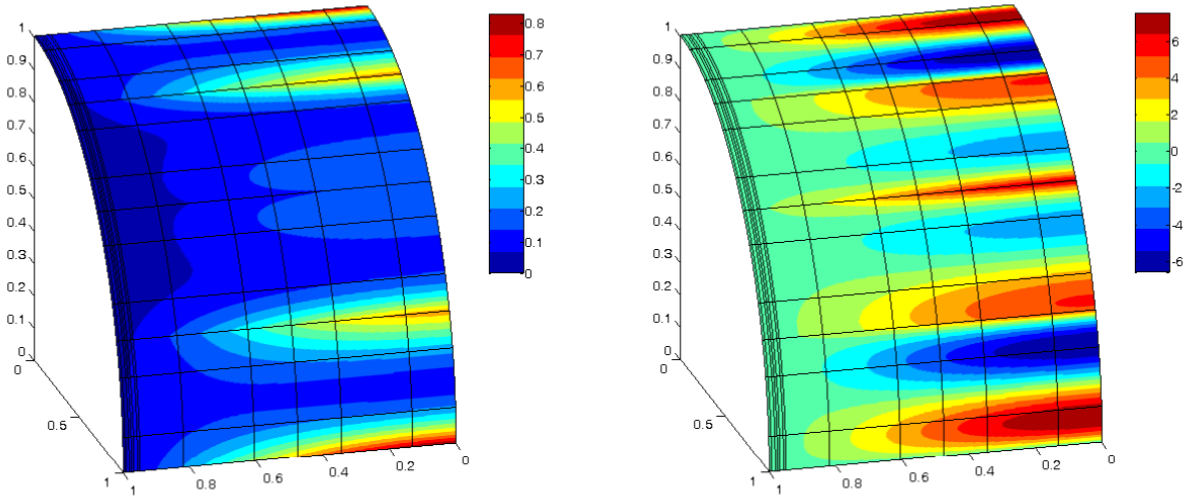

(a) displacement vector magnitude (b) rotation about the *X*-axis

Figure 20. Contour of the displacement vector magnitude and rotation about the *X*-axis when the cylindrical shell problem in Figure 16 with clamped ends is modelled by 4×4 graded mesh and cubic ANS* element. Nodal lines which are not necessary the element boundaries are also shown.

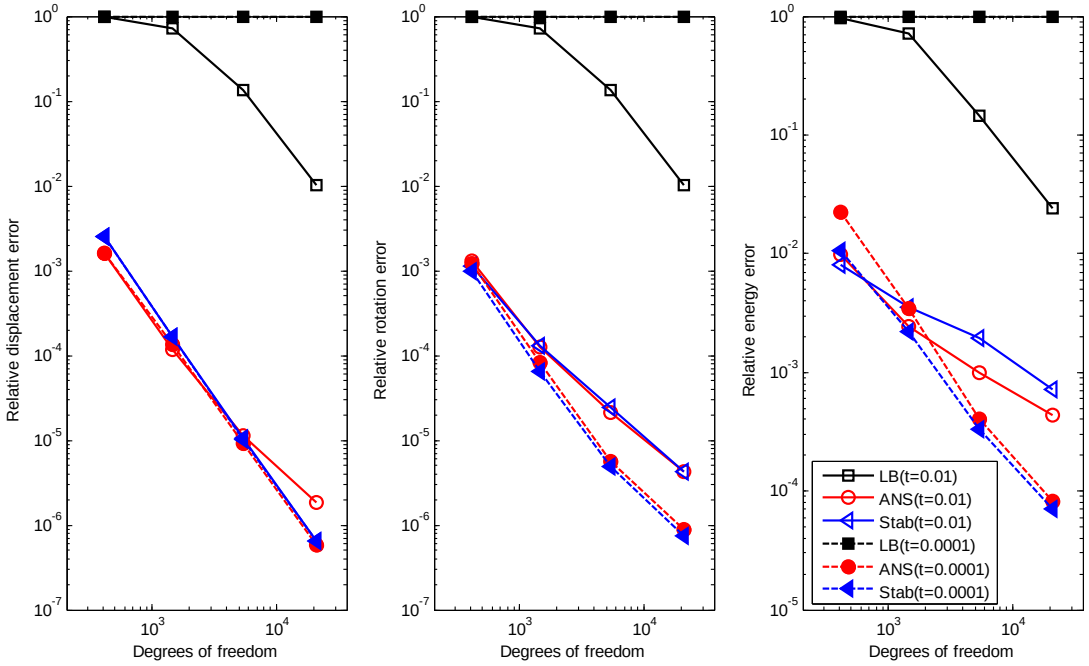

(a) $n_L = 2$

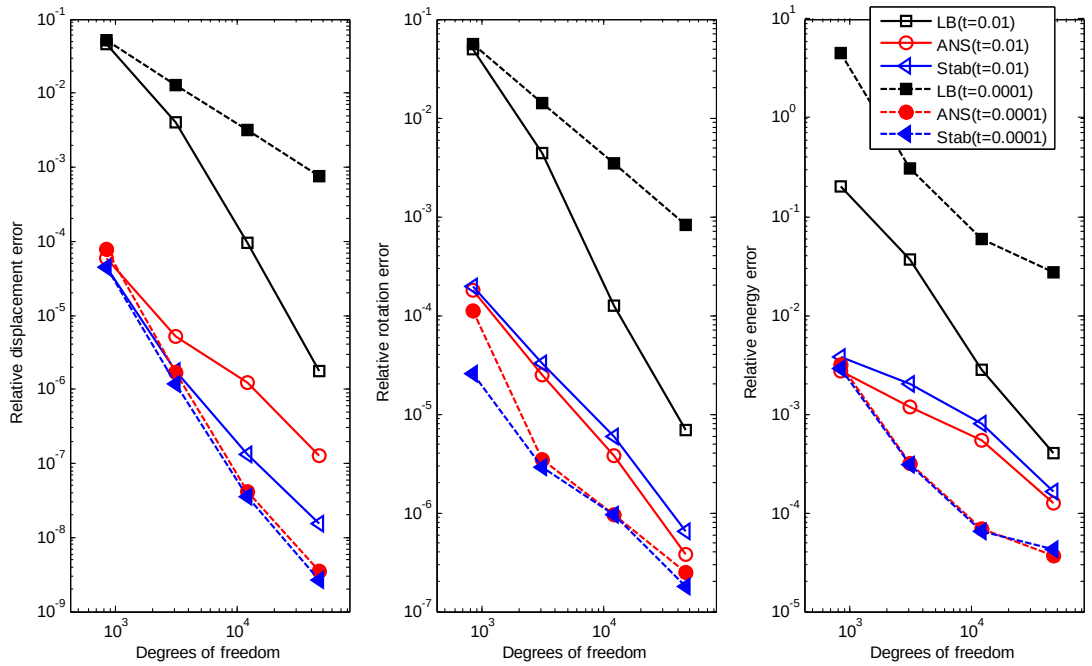

(c) $n_L = 3$

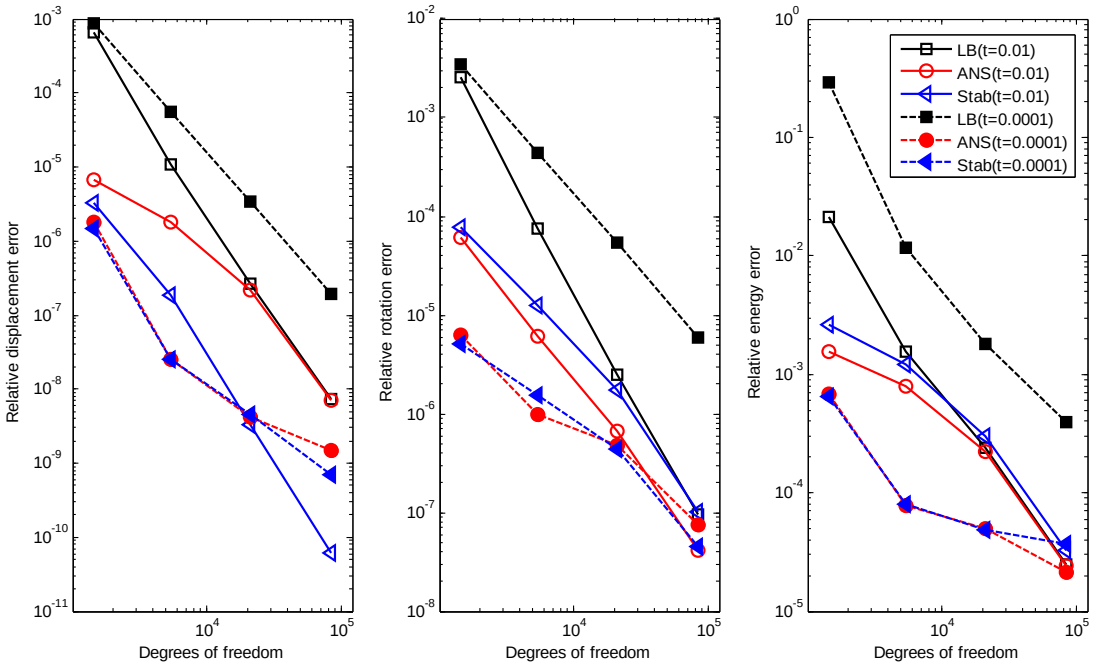

(c) $n_L = 4$

Figure 21. Errors for the cylindrical shell problem in Figure 16 with free ends.

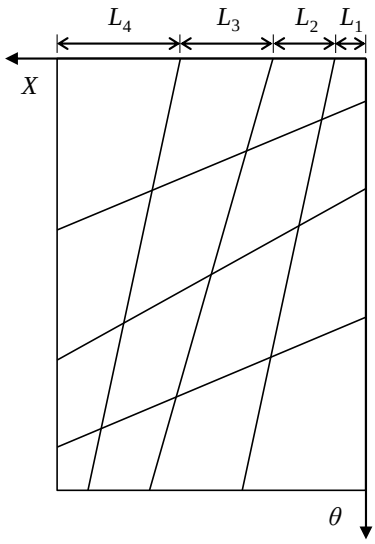

Figrue 22. Distorted meshes for cylindrical shell problem in Figure 16.

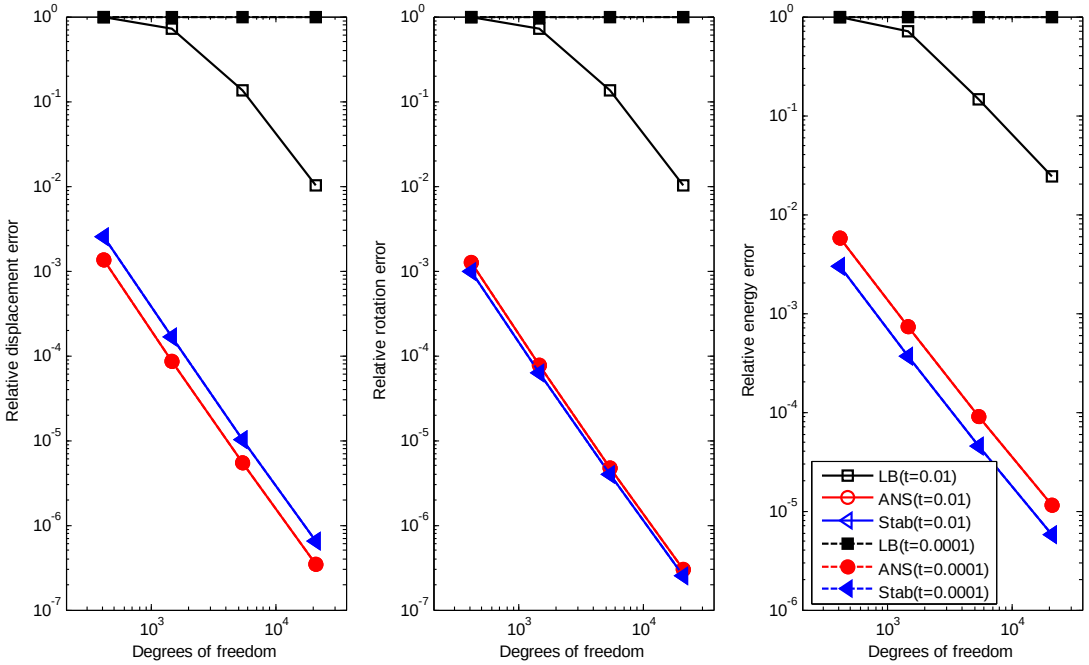

(a) $n_L = 2$

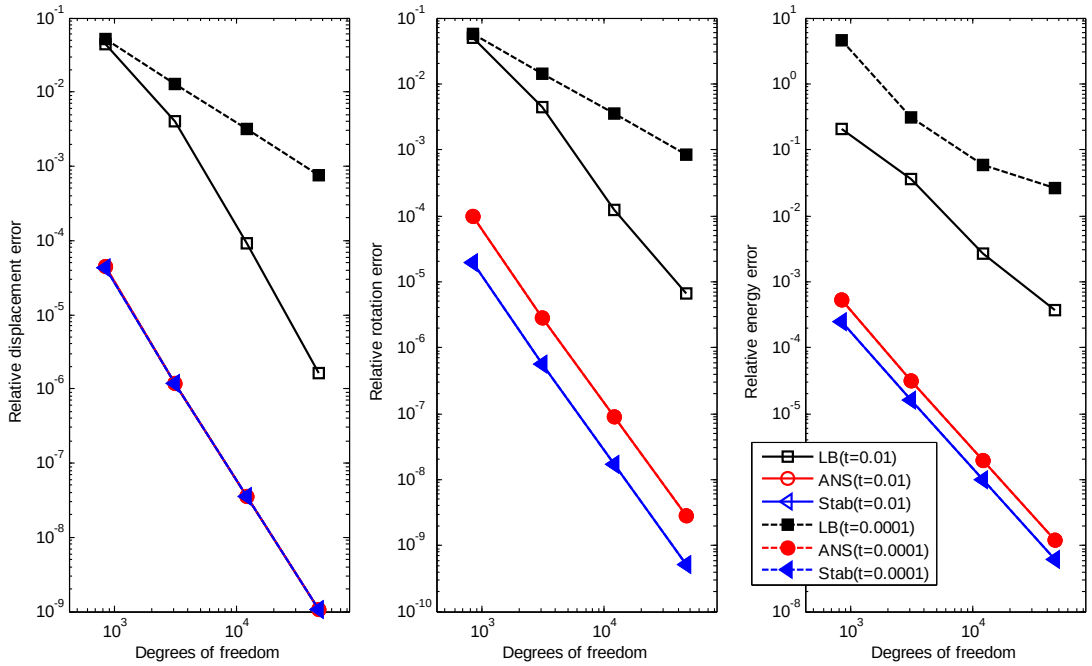

(b) $n_L = 3$

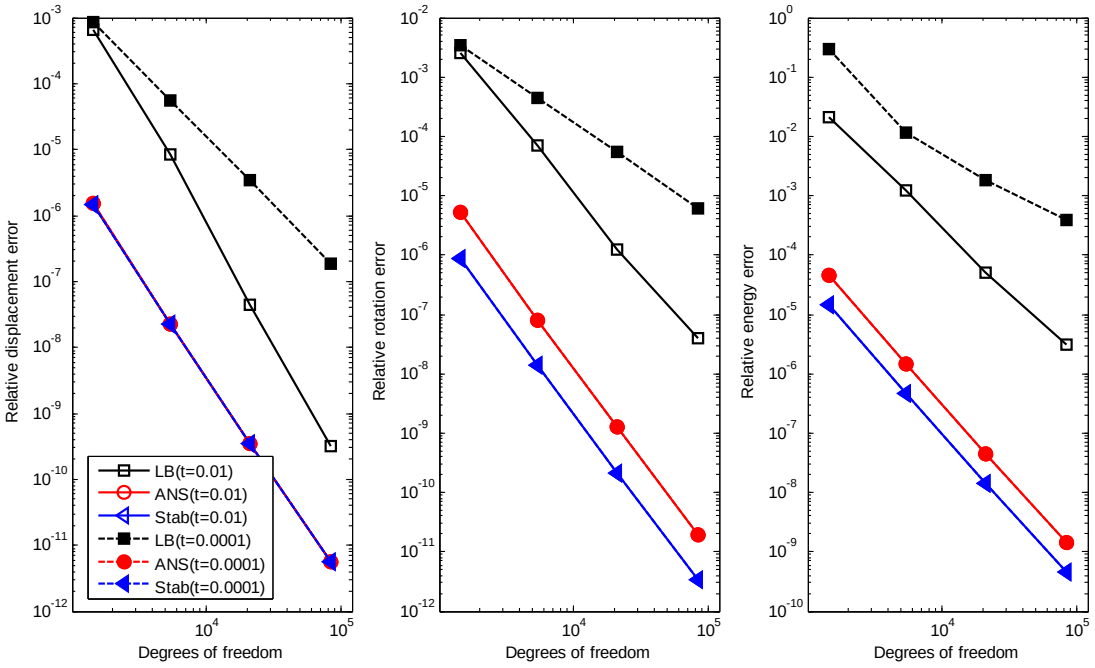

(a) $n_L = 4$

Figure 23. Errors for the cylindrical shell problem in Figure 16 with symmetric ends and modelled by uniform meshes.

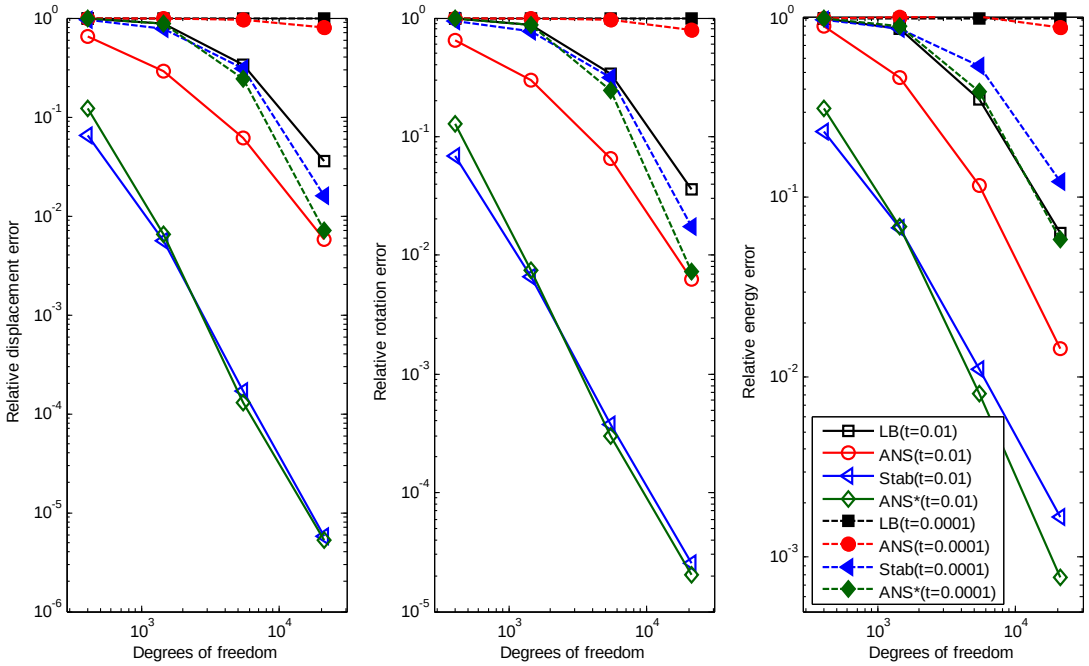
Relative displacement error
Relative rotation error
Relative energy error
Degrees of freedom
LB(t=0.01)
ANS(t=0.01)
Stab(t=0.01)
ANS*(t=0.01)
LB(t=0.0001)
ANS(t=0.0001)
Stab(t=0.0001)
ANS*(t=0.0001)

(a) $n_L = 2$

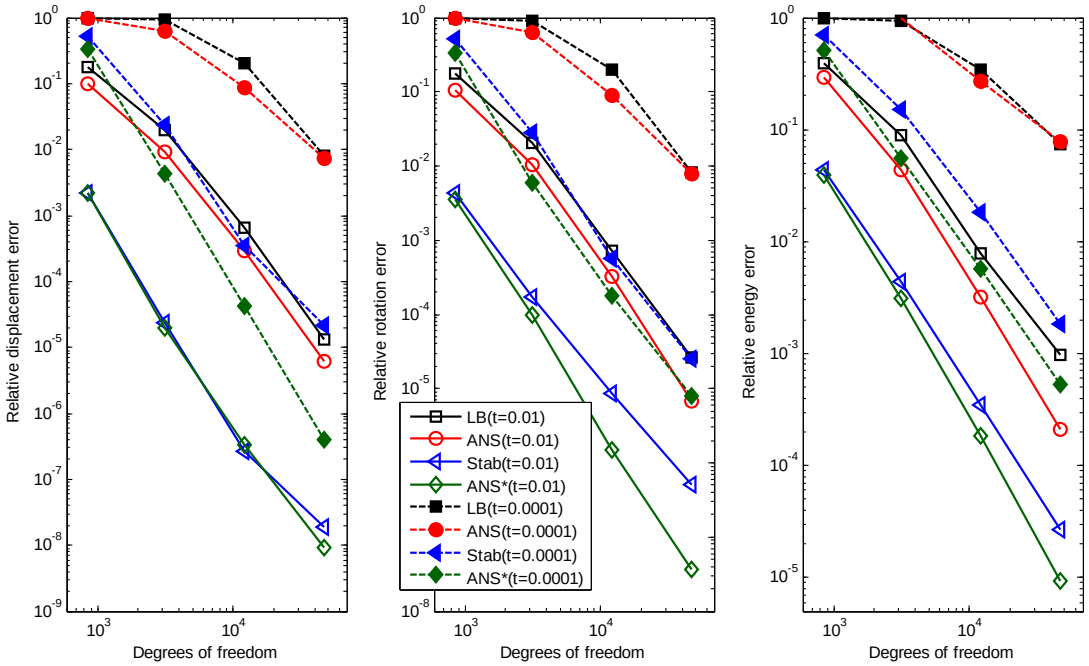
Relative displacement error
Relative rotation error
Relative energy error
Degrees of freedom
LB(t=0.01)
ANS(t=0.01)
Stab(t=0.01)
ANS*(t=0.01)
LB(t=0.0001)
ANS(t=0.0001)
Stab(t=0.0001)
ANS*(t=0.0001)

(b) $n_L = 3$

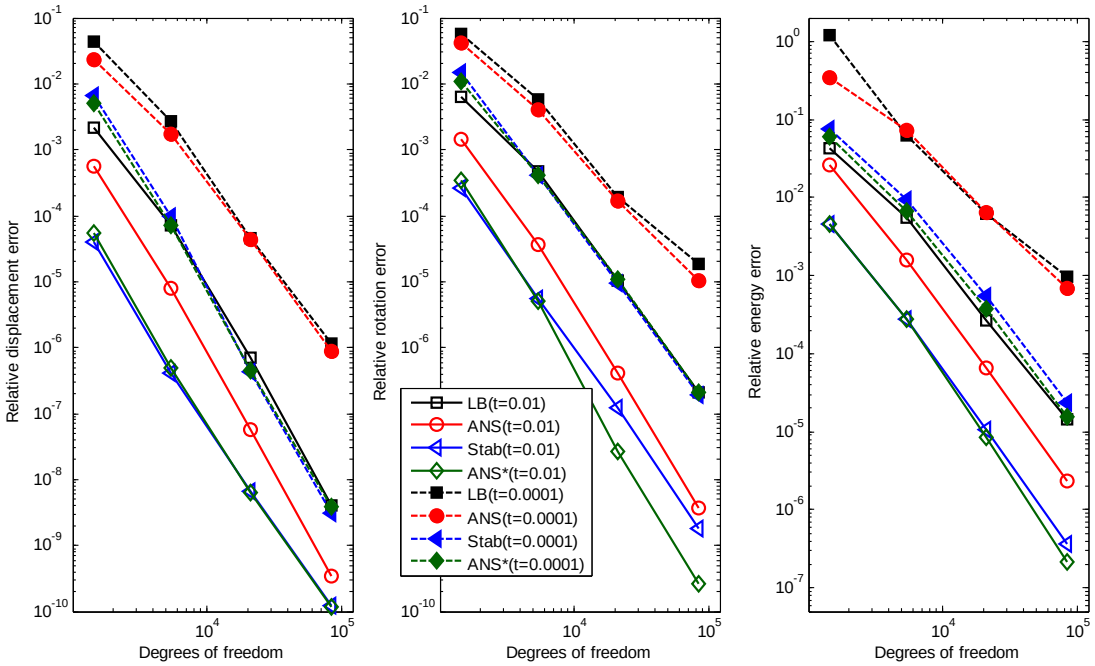

(c) $n_L = 4$

Figure 24. Errors for the cylindrical shell problem in Figure 16 with symmetric ends and modelled by distorted meshes illustrated in Figure 22.

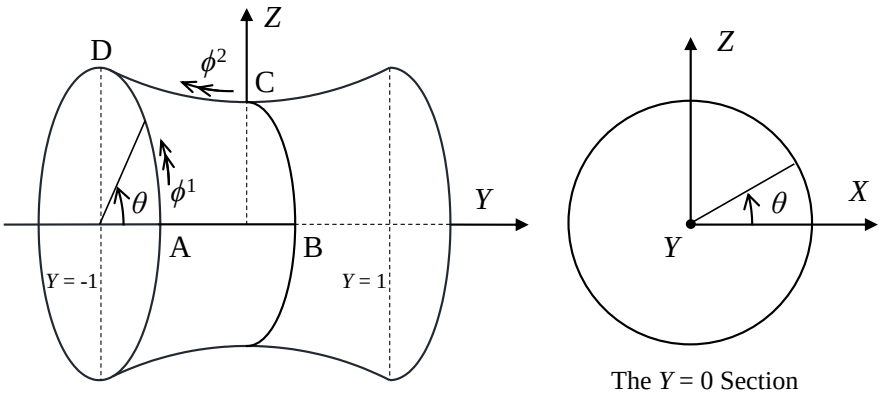

(a)

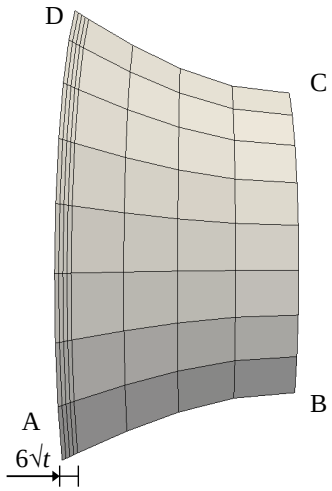

(b)

Figure 25. (a) The hyperbolic shell geometry and (b) the 8×8 graded mesh.

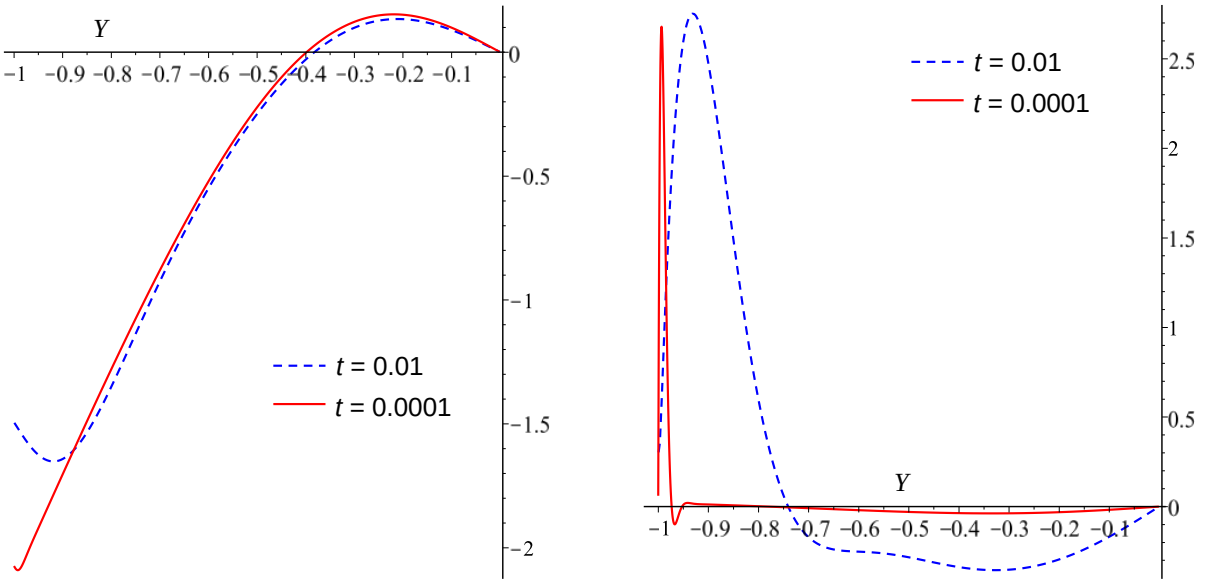

(a) $\gamma_{xy}^{m} Et / p_0$ (b) $\gamma_{xy}^{b} E\sqrt{t} / p_0$

Figure 26. The reference inplane shear strains along $\theta = \pi/4$ when the two ends of the hyperbolic shell in Figure 25 are clamped. The results are obtained by 64 sixth order 1D elements.

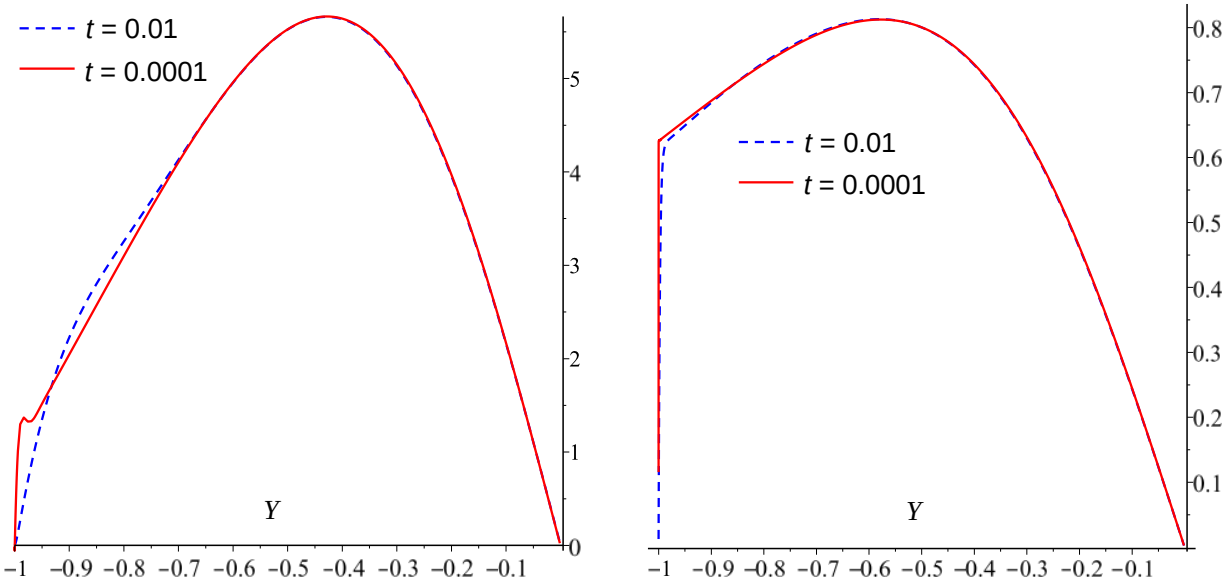

(a) $\gamma_{xy}^{m} Et / p_0$ (b) $\gamma_{xy}^{b} Et^2 / p_0$

Figure 27. The reference inplane shear strains along $\theta = \pi/4$ when the two ends of the hyperbolic shell in Figure 25 are free. The results are obtained by 64 sixth order 1D elements.

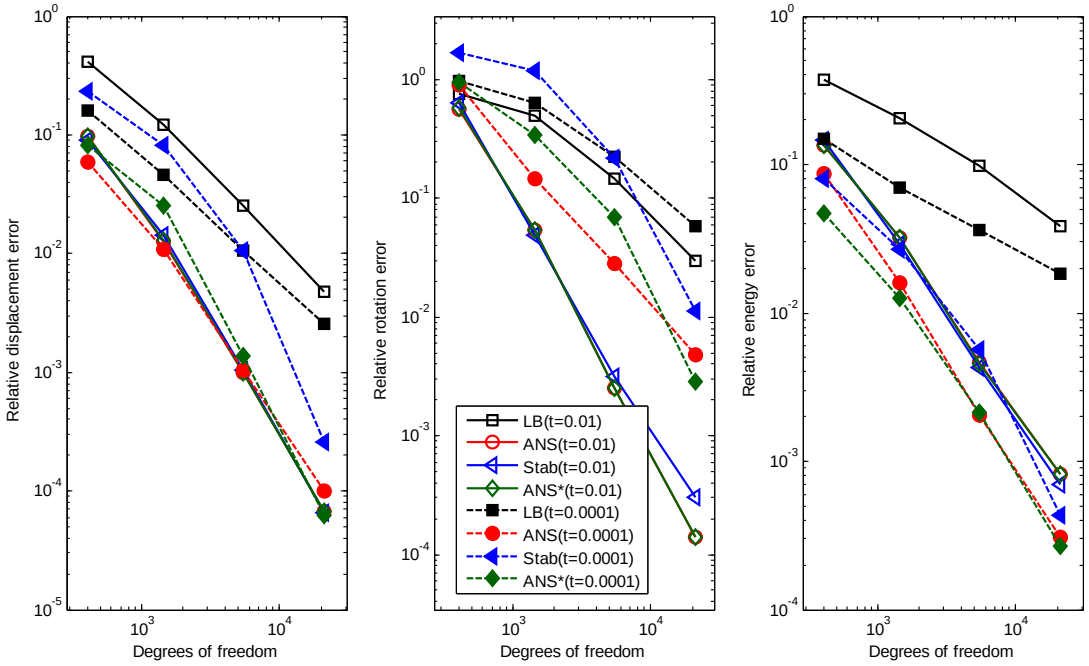
Relative displacement error
Relative rotation error
Relative energy error
Degrees of freedom
LB(t=0.01)
ANS(t=0.01)
Stab(t=0.01)
ANS*(t=0.01)
LB(t=0.0001)
ANS(t=0.0001)
Stab(t=0.0001)
ANS*(t=0.0001)

(a) $n_L = 2$

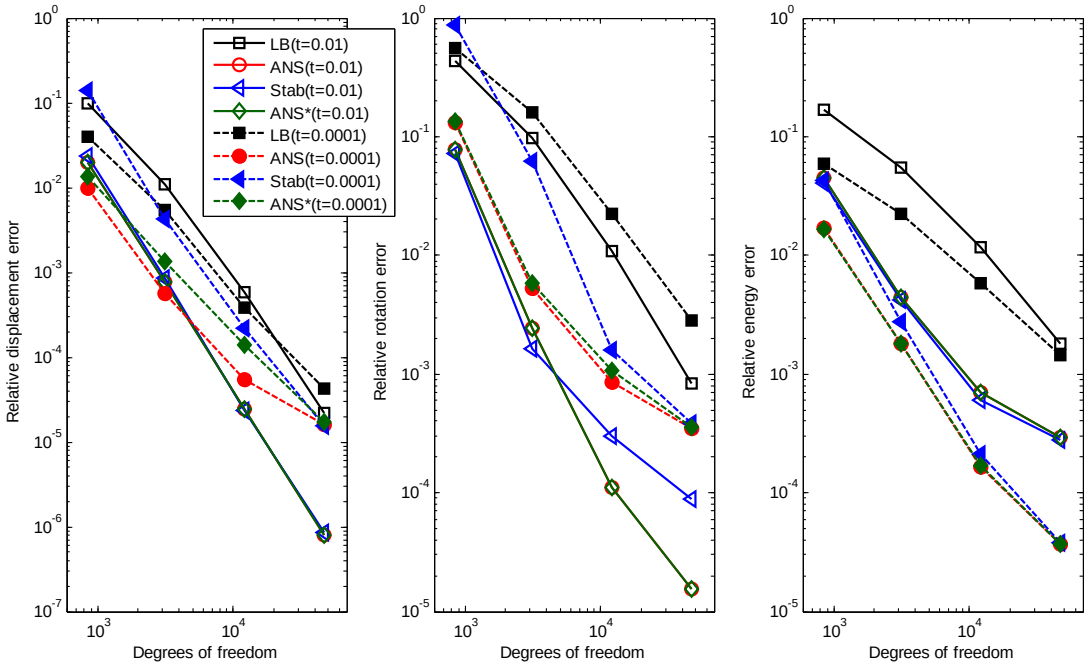
Relative displacement error
Relative rotation error
Relative energy error
Degrees of freedom
LB(t=0.01)
ANS(t=0.01)
Stab(t=0.01)
ANS*(t=0.01)
LB(t=0.0001)
ANS(t=0.0001)
Stab(t=0.0001)
ANS*(t=0.0001)

(b) $n_L = 3$

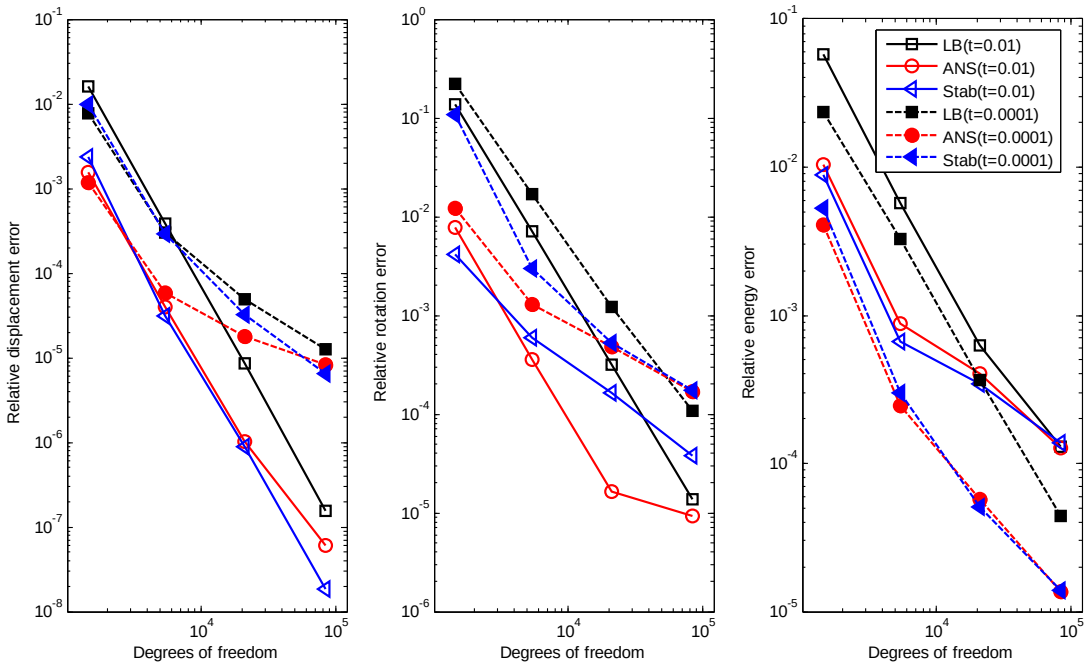

(c) $n_L = 4$

Figure 28. Errors for the hyperbolic shell problem in Figure 25 with both end clamped.

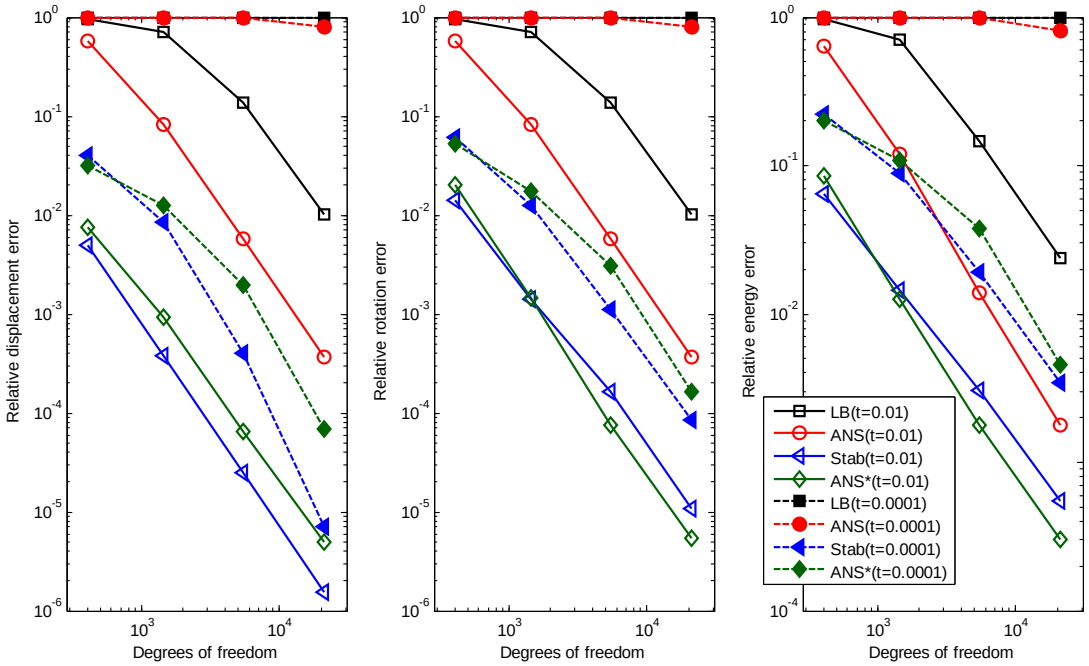

(a) $n_L = 2$

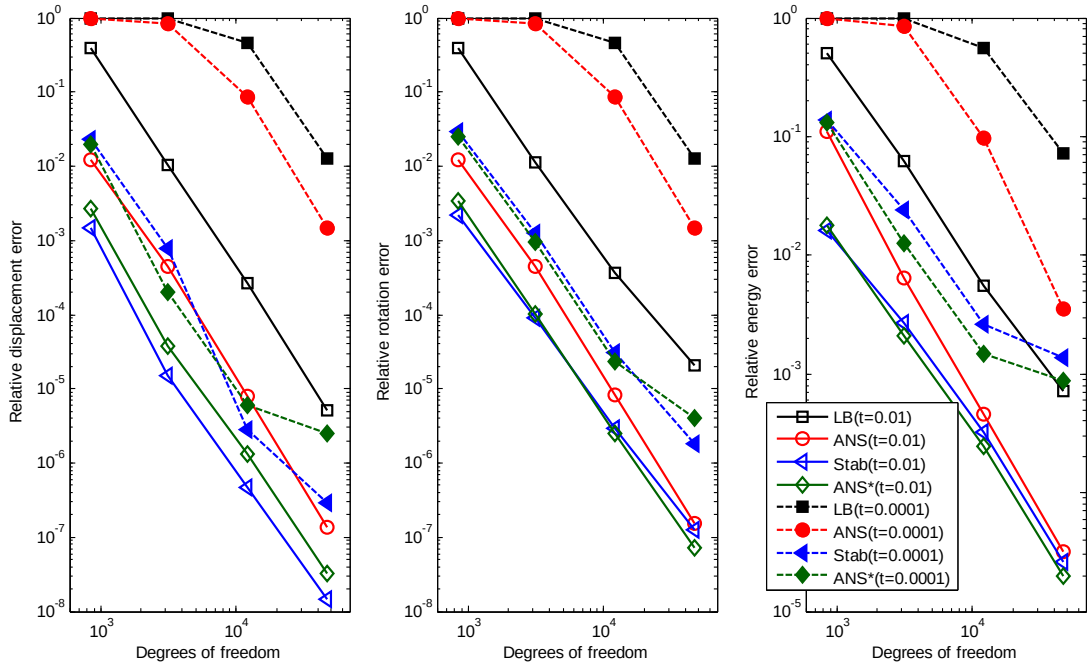

(b) $n_L = 3$

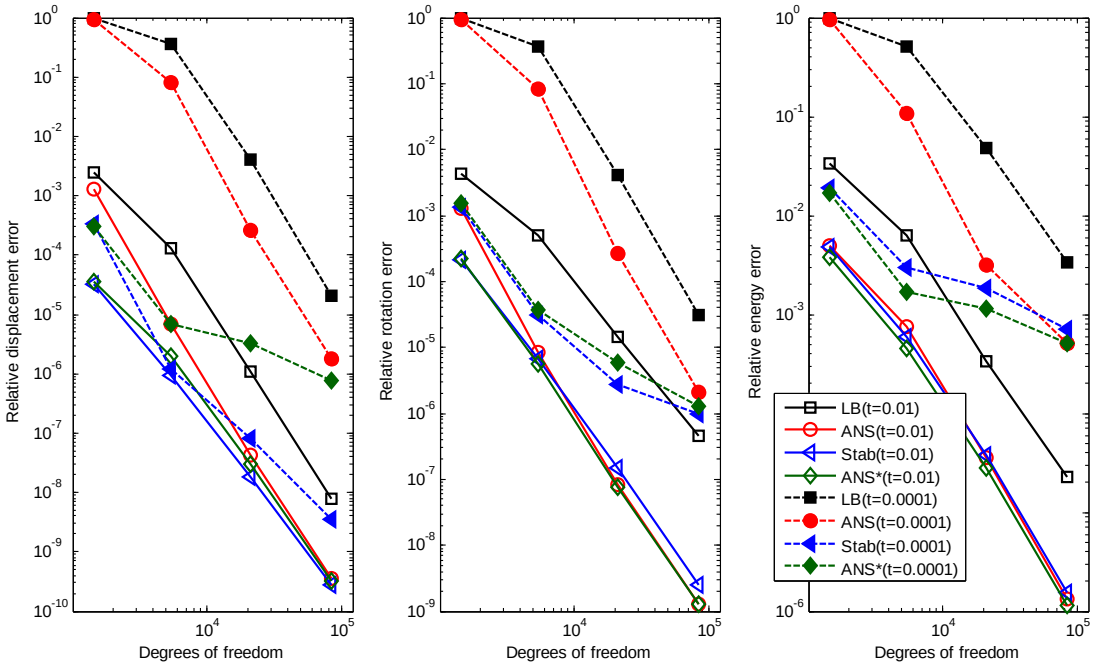

(c) $n_L = 4$

Figure 29. Errors for the hyperbolic shell problem in Figure 25 with both ends free.

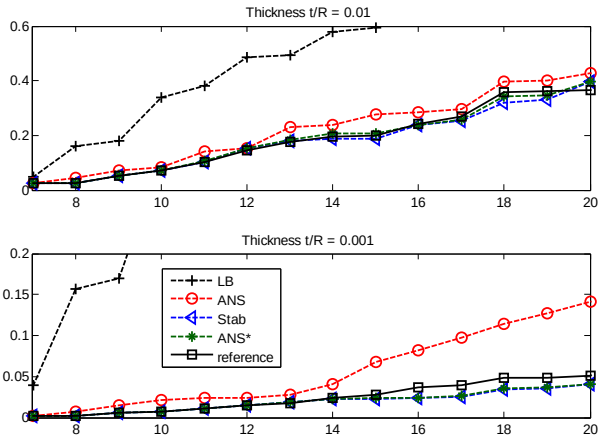

(a) n_L = 2, 4×4 mesh

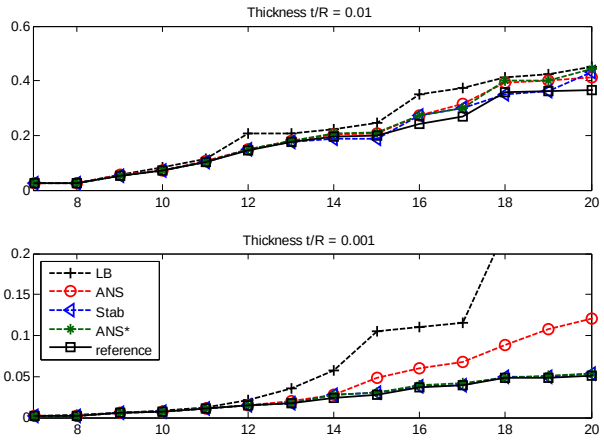

(b) n_L = 4, 2×2 mesh

Figure 30. The non-zero frequency parameters $\omega R\sqrt{\rho / E}$ in increasing order for a free cylindrical shell panel with the same dimensions as ABCD in Figure 16(a). Uniform 4×4 and 2×2 meshes are employed for the quadratic and quartic elements.

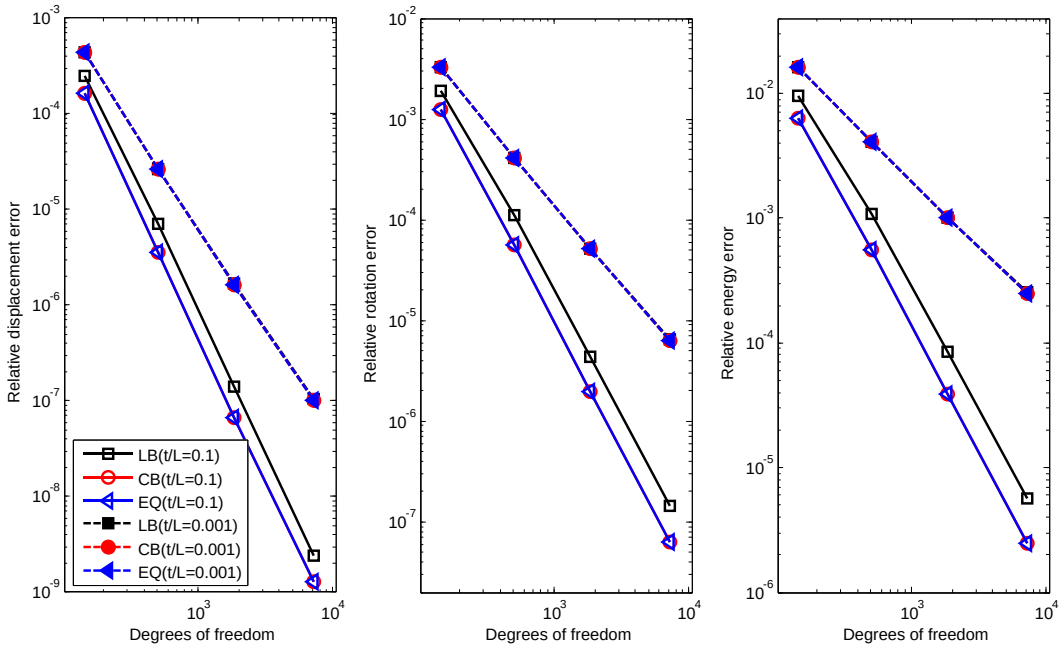

(a) Regular mesh

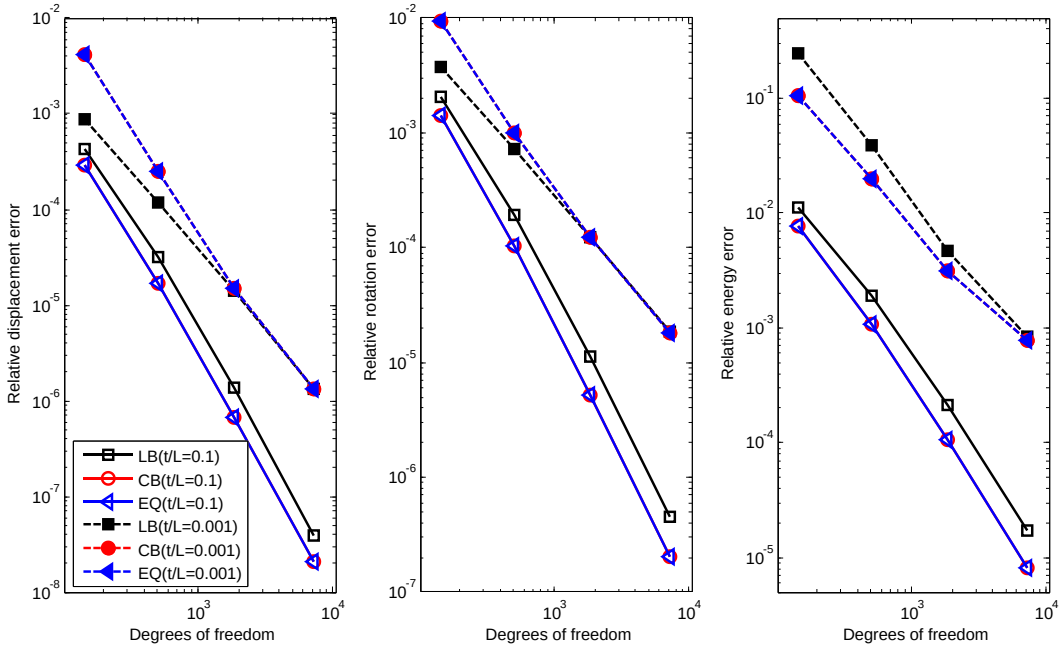

(b) Distorted mesh

Figure 31. Errors of the third order Lagrange elements defined by Lobatto, equi-spaced “EQ” and Chebyshev “CB” nodes in the hard-simply supported square plate problem in Figure 7. (a) Regular mesh and (b) the distorted mesh in Figure 9 are employed.

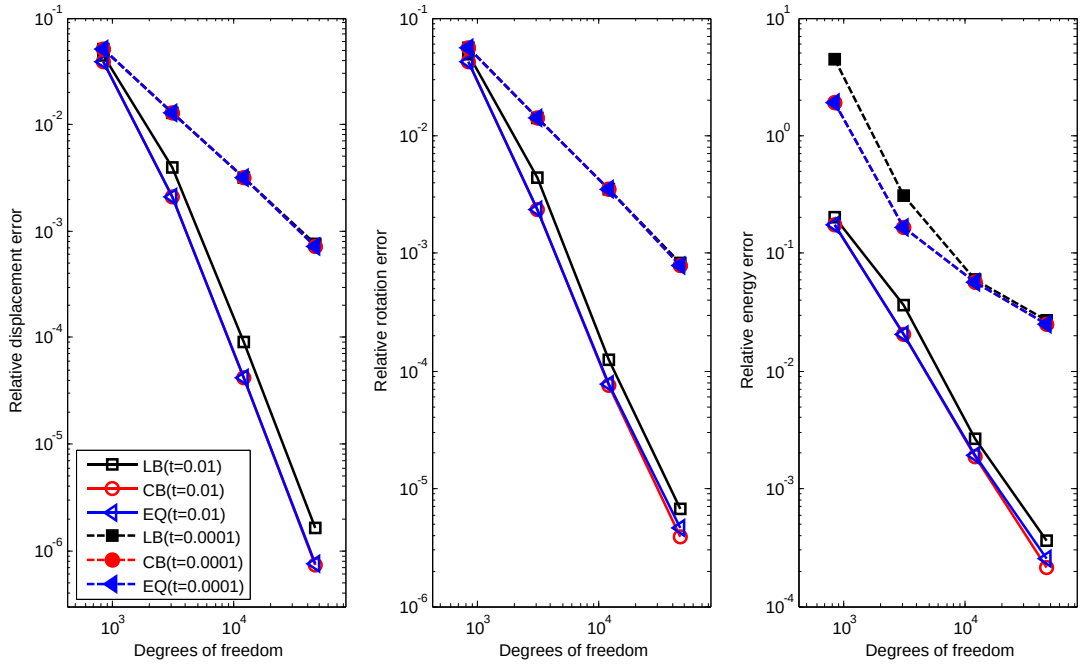

(a) Regular mesh

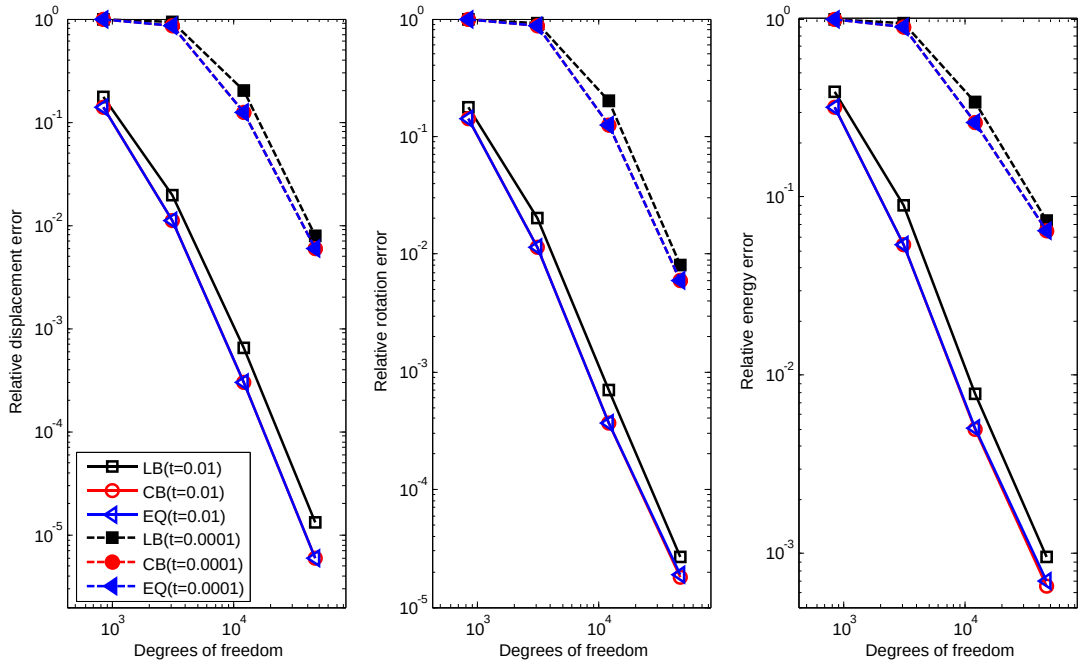

(b) Distorted mesh

Figure 32. Errors of the third order Lagrange elements defined by Lobatto, equi-spaced “EQ” and Chebyshev “CB” nodes in the cylindrical shell problem in Figure 16 with symmetric ends. (a) Regular mesh and (b) the distorted mesh in Figure 22 are employed.